Perovskite-Silicon Tandem based Photoelectrochemical Systems for Efficient Solar Hydrogen Generation

Astha Sharma

A thesis submitted for the degree of

Doctor of Philosophy of

The Australian National University

School of Engineering (SOEN)
College of Engineering and Computer Science
The Australian National University

25th April 2021

Declaration

This thesis reports the research I conducted during my PhD, at the School of Engineering, College of Engineering and Computer Science, The Australian National University, Canberra ACT, Australia. I certify that this thesis does not incorporate any material previously submitted for a degree or diploma in any university, and that, to the best of my knowledge, it does not contain any material previously published or written by another person except where due reference is made in the text. The work in this thesis is my own, except for the contributions made by others as described in the acknowledgment or referenced in an appropriate manner.

Astha Sharma

For their unconditional love, patience, and support,

I dedicate this to Khushi Sharma and Siddharth Khole.

Acknowledgements

I would like to begin by acknowledging the traditional custodians of the land upon which I conducted my research and I pay my respects to their elders past and present. I extend that respect to the Aboriginals and Torres Strait Islander people.

I would like to take this opportunity to thank my supervisor, *Dr. Fiona J Beck*, who has been a guardian angel for me during this research. She has been actively involved at every step of the way. Her insights and guidance were instrumental which have contributed to shaping my vision. She has kept me on my toes, challenged me, encouraged me, inspired me and most of all shaped me as a researcher. For all this, I am eternally grateful. My Supervisory Panel for it was impossible to do this without their valuable guidance and insights. I am thankful to *Dr. Heping Shen* for her invaluable guidance and support throughout this research. I am extremely grateful to *Dr. Siva Karuturi*, for his guidance has been instrumental in defining the path of my research. I would like to express my utmost sincere gratitude to *Dr. Kylie Catchpole*, for her immense knowledge and abundant life experiences have been a source of guidance and inspiration for me during this research journey and personal life.

I am thankful for the tuition fee waiver and PhD Scholarship support from the *School of Engineering, ANU* and the financial support from the *Australian Renewable Energy Agency* towards conducting this research.

I would like to take this chance to thank all the members of the *Solar Photovoltaics group* at the *School of Engineering, ANU*. It is their ever-helpful attitude and a constant support that has made my PhD a great learning experience. I would particularly like to mention and thank

Chris Samundsett for teaching me silicon cell fabrication. It is a very lengthy process, and I am grateful for your time and patience. *Sachin Surve*, for his help with designing the Si masks. *Dr. Pheng Phang, Dr. Teng Kho, Dr. Di Yan, Dr. Rabin Basnet, Stephane Armand, Dr. Wengsheng Liang and Dr. Parvathala Narangari* for helping me with all my doubts around silicon. I greatly appreciate all the help and support from *Dr. Yuan (Helena) Wang, University of New South Wales (UNSW)* and *Dr. The Doung* with whom I have worked closely with during my PhD. I would like to thank *Dr. Peng Liu, Tsinghua University* for their collaboration and providing NiFe catalyst used in chapter 4. I would also like to thank all my colleagues in *Research School of Physics and Engineering, ANU* especially to *Joshua Butson* and *Asim Riaz* for their help with GC measurements.

I would like to extend special mentions and gratitude to *Nina De Cartiat, Maureen Braurers, James Cotsell* and *Bruce Condon* for all the technical support. I have approached them for all kinds of new experiment setups, orders and countless technical issues and they have always provided a solution to all my queries. *Kaushal Vora* and *Olivier Lee Cheong Lem* at the *Australian Nanofabrication Facility, ANU* for the training and technical support for sputtering and e-beam deposition experiments.

I take this opportunity to thank all my friends, who have been my family here for the last four years. *Dr. Mahesh Venkataraman* and *Preetha Iyer,* aka *Thakurs* for treating me like your family. Thank you for all the love, laughter and of course the amazing food. *Dr. Ankur Sharma,* for being the brother I never had. Thank you for the constant support and care and of course our funny banters which were a great source of entertainment for me. *Dr. Anukriti Mathur and Chirag Ajwani for* being the most amazing house mates. Anukriti Mathur, we have lived our PhD journeys together. Thank you for being my PhD twin and all the encouragement and support throughout.

I take this moment to thank my parents *Sandhya and Nitin Sharma* for all their efforts, sacrifices, love and most importantly their contributions in making me capable to pursue my dreams. I have no words that could explain my sincere most gratitude for their sacrifices and love that they have showered me with. *Mohana Khole,* for her support and words of encouragement, especially during the times of covid. She had been a big support in helping me adjust with the work from home environment and focusing on my work despite all the odds. To my sister *Khushi Sharma,* for all her support throughout these years. As the definition of her name says, she is absolutely a source of happiness. Finally, I would like to thank my partner *Siddharth Khole* for being there through this adventurous journey. For making me believe that nothing is impossible if you are determined enough. Thank you for immense love, support and encouragement that kept me going. I would not have been able to do this without you.

“ Yes, my friends, I believe that water will someday be employed as fuel, that hydrogen and oxygen, which constitute it, used singly or together, will furnish an inexhaustible source of heat and light….

I believe, then, that when the deposits of coal are exhausted, we shall heat and warm ourselves with water. Water will be the coal of the future.”

Jules Verne, The Mysterious Island, 1874

Abstract

Direct solar hydrogen generation (DSTH) is a promising method for renewable hydrogen generation, where solar energy drives the generation of hydrogen and oxygen by molecular dissociation of water on a catalytic or semiconductor surface. Despite an enormous amount of work over the last few decades, DSTH has not yet been implemented on large scale due to low efficiency and high costs. Techno-economic analysis of different solar hydrogen generation systems has identified the solar-to-hydrogen conversion (STH) efficiency as an important parameter for cost reduction. The US Department of Energy has set a target of 20% STH efficiency by 2020, and an ultimate goal of 25% using low-cost materials to ensure the economic viability of direct solar hydrogen generation for large scale hydrogen production.

This thesis investigates perovskite-silicon tandem photovoltaic (PV) and earth abundant catalysts-based systems for low-cost, high efficiency direct solar hydrogen generation. The thesis starts by developing a photoelectrochemical system based on perovskite PV and Si photocathodes in a tandem configuration. We demonstrate a high-performance Si photocathode, incorporating state-of-the-art charge selective passivation and earth abundant catalysts, with an applied bias to photon efficiency (ABPE) of over 10%. Earth abundant catalysts are fabricated by sputter deposition for direct integration with the silicon photocathode. Using a physical deposition method allows catalyst fabrication to be integrated easily with current PV manufacturing and allows the possibility of scaling up the system. Charge selective passivation layers improve the Si photocathode performance by roughly 70% compared to Si photocathode without any passivation, highlighting the importance of the efficiency loss due to recombination at the Si/catalyst interface. An overall water splitting efficiency of 17% is achieved for the photoelectrochemical system when combined with a

previously reported Earth abundant OER catalyst and a wide bandgap perovskite solar cell in tandem.

Next, we identify performance limitations and conceptualise practical device designs to improve the STH efficiency towards 20%, by developing a new theoretical framework to quantify and compare different loss mechanisms in PV based solar hydrogen generation systems and evaluate the potential of different loss mitigation techniques to improve the solar to hydrogen generation efficiency. Our analysis shows that the two largest losses in an ideal system are energy lost as heat in the photovoltaic component, and current and voltage mismatch between the PV and electrochemical (EC) components due to sub-optimal system configuration. Two different loss mitigation techniques are considered: decoupling the PV and EC system by introducing a power management unit, and thermal integration to improve the water splitting reaction kinetics by utilizing the heat losses from the PV component to increase the electrolyte temperature. Employing loss mitigation techniques targeting the two major efficiency losses results in predicted STH efficiencies above 20% for realistic perovskite-silicon tandem-based systems, without the need for further improvement of the photovoltaic devices or catalyst. These results identify where best to target interventions to mitigate losses and ensure maximum improvement in the performance.

Next, we develop a system with perovskite-Si tandem PV and Ni based earth abundant catalysts with a record STH efficiency of 20%. The NiMo electrodes with a high density of NiMo active sites are fabricated in a flower-stem morphology and exhibit an exceptional HER performance. In addition, an improved perovskite top cell with a record open circuit voltage is achieved using n-dodecylammonium bromide.

Further analysis is performed to assess the potential for improvement in the STH efficiency. Decoupling the PV and EC component of the system to allow optical configuration, would improve the STH efficiency of the current system to 23% without any further improvement in the components or materials. With Si solar cell performance already close to theoretical limits, improving the perovskite solar cell offers the best opportunities of increasing the overall tandem efficiency. Realistic enhancements in the performance of perovskite solar cell alone could improve the STH efficiency to 25%.

A technoeconomic analysis is performed to assess the cost competitiveness of the developed system. The levelized cost of hydrogen (LCOH) of the DSTH system is calculated as $4.1/Kg. Combining this with projected cost reductions in the PV module and membrane costs could further reduce the LCOH to $2.3/Kg, presenting a remarkable opportunity to realise cheap renewable hydrogen.

The results of this thesis show that perovskite-silicon tandem based photoelectrochemical systems have the potential to make large scale direct solar hydrogen generation a reality by demonstrating STH efficiencies of 20% using all low-cost systems. Our work demonstrates that 25% STH efficiency is achievable with further improvement in the perovskite solar cell performance. In addition, we have developed a modelling approach capable of, identifying the major limitations of DSTH systems under realistic operating conditions. In doing so we have demonstrated the potential of different loss mitigation techniques to improve the STH efficiency by improving system components and integration and introducing thermal integration. This work will encourage dedicated research with a clear awareness of which components to focus on, and how to improve system design, enabling progress towards achieving the aim of low-cost, large scale solar hydrogen generation.

Publications

This thesis is based on following publications:

1. **Astha Sharma**, The Doung, Peng Liu, Doudou Zhang, Di Yan, Christian Samundsett, Heping Shen, Siva Karuturi, Kylie Catchpole and Fiona J. Beck. "Silicon photocathodes with carrier selective passivated contacts, and earth abundant catalyst for high performance, low-cost, direct solar hydrogen generation." *Under preparation* (Chapter 4)

2. **Astha Sharma**, and Fiona J. Beck. "Quantifying and Comparing Fundamental Loss Mechanisms to Enable Solar-to-Hydrogen Conversion Efficiencies above 20% Using Perovskite–Silicon Tandem Absorbers." *Advanced Energy and Sustainability Research*: 2000039. (Chapter 5)

3. Yuan Wang*, **Astha Sharma***, The Duong, Hamidreza Arandiyan, Tingwen Zhao, Doudou Zhang, Zhen Su, Magnus Garbrecht, Fiona J. Beck, Siva Karuturi, Chuan Zhao and Kylie Catchpole. "Direct Solar Hydrogen Generation at 20% Efficiency Using Low-Cost Materials. " *under review in advanced energy materials* (Chapter 6)

Other publications by the author:

1. Karuturi, Siva Krishna, Heping Shen, **Astha Sharma**, Fiona J. Beck, Purushothaman Varadhan, The Duong, Parvathala Reddy Narangari, Doudou Zhang, Yimao Wan, Jr-Hau He, Hark Hoe Tan, Chennupati Jagadish, and Kylie Catchpole. "Over 17% Efficiency Stand-Alone Solar Water Splitting Enabled by Perovskite-Silicon Tandem Absorbers." *Advanced Energy Materials 10, no. 28 (2020): 2000772.*

2. Joshua D. Butson, **Astha Sharma**, Hongjun Chen, Yuan Wang, Yonghwan Lee, Purushothaman Varadhan, Mihalis N. Tsamps, Chuan Zhao, Antonio Tricoli, Hark Hoe Tan, Chennupati Jagadish and Siva Karuturi. " Surface-Structured Ni-Based Cocatalyst Foils Unravelling a Pathway for High-Efficiency and Ultra-Stable Solar Water Splitting Cells." *Under review*

3. Doudou Zhang, Haobo Li, **Astha Sharma**, Wensheng Liang, Yuan Wang, Hongjun Chen, Kaushal Vora, Di Yan, Zhen Su, Antonio Tricoli, Chuan Zhao, Fiona Beck, Karsten Reuter, Kylie Catchpole, and Siva Karuturi. "Direct Synthesis of Earth-Abundant Nitrogen Vacancy-Enhanced Ni3N/Ni Catalysts for Alkaline Hydrogen Evolution with High Activity and Stability". *Under review*

4. Bikesh Gupta, Md. Anower Hossain, **Astha Sharma**, Doudou Zhang, Hark Hoe Tan, Chennupati Jagadish, Kylie Catchpole, Bram Hoex, and Siva Krishna Karuturi. "Recent Advances in Materials Design using Atomic Layer Deposition for Energy Applications". *Under preparation*

5. **Astha Sharma**, E. Senthil Prasad, and Harsh Chaturvedi. "Photon induced separation of bio-nano hybrid complex based on carbon nanotubes and optically active bacteriorhodopsin." *Optical Materials Express 6.4 (2016): 986-992.*

Oral Conference Presentations

1. Astha Sharma " Optimizing Thermal and Electrical Integration of PV for Solar Hydrogen Generation." *International Conference on Materials for Advanced Technologies (ICMAT), Singapore 2019*

2. Astha Sharma "Silicon Photocathodes for Efficient Solar Hydrogen Generation." *International Conference on Materials for Advanced Technologies (ICMAT), Singapore 2019*

3. Astha Sharma "Limiting efficiencies for Solar Hydrogen Generation: Can we use the losses?" *Asia Pacific Solar Research Conference, Canberra 2019*

4. Astha Sharma. " Quantifying and Comparing Fundamental Loss Mechanisms in Direct Solar Hydrogen Generation Systems." *Virtual MRS Spring Meeting and Exhibit, 2021*

Table of Content

Chapter 1

Introduction

1.1. Motivation

To limit global warming below 2 ℃, green-house gas (GHG) emissions must be reduced by around 25% below 2010 levels by 2030, and reach net zero by 2070 [1]. Energy related emissions account for two-thirds of the global GHG emissions, highlighting the urgent need to transition from fossil fuels to renewable energy sources. With the current trajectory, CO_2 emission are projected to increase to 35 $Gtonns/year$ by 2050 [2]. The Intergovernmental Panel on Climate Change (IPCC) has indicated that current global policies can stabilise the CO_2 emission but will not help with reducing it, resulting in the need for a profound transformation from fossil-fuels to a renewable, low-carbon energy system [1]. According to the International Renewable Energy Agency (IRENA), renewables and energy efficiency can reduce the energy related CO_2 emission by up to 94% by 2050. Renewable energy and electrification are expected to contribute 41% and 13% to reducing the emissions, respectively. Further, the energy efficiency will contribute to 40% in CO_2 reduction. To achieve this, renewable energy's share in global energy consumption needs to increase from 18% today to 65% by 2050 [2].

Presently one-third of the CO_2 emission comes from energy intensive industry sectors, such as iron, steel, cement, aluminium production and freight transport, which heavily depend on

fossil fuels without any economically viable alternative [3]. Total decarbonisation of these sectors is difficult by means of electrification alone, emphasizing on the need of alternate renewable fuels for rapid decarbonisation of energy use in transportation and industrial processes.

1.2. Hydrogen as a promising fuel candidate

The high specific energy density of hydrogen allows its use as a feedstock in industry as well as fuel, which makes it a suitable candidate for a carbon-free energy vector [4, 5]. Hydrogen is an energy carrier like electricity and can be produced and stored in different ways depending upon the end use. its flexibility in terms of production and storage has made it attractive for use in a wide variety of applications.

1.2.1. Current hydrogen production and applications

Around 70 Mt of merchant hydrogen is currently produced every year, primarily for use in industries such as refineries, ammonia, bulk chemicals, etc. Due to this, industry has well established hydrogen production and handling techniques [6].

The current primary source of hydrogen production is steam methane reforming (SMR). Around 76% of the required hydrogen demand is met from production through natural gas and 23% using coal. This translates to consumption of around 205 billion cubic metres of natural gas and 107 metric tons of coal, 6% and 2% of global use, respectively. Each kilogram of hydrogen produced from SMR results in ~10 kgs of CO_2 [6].

GHG emission intensity of existing fossil fuel technologies can be reduced by coupling them with carbon capture and storage technologies (CCS). Large quantities of CO_2 can be avoided from being released in the atmosphere, by capturing it from stationary emitters, compressing it, and injecting it underground at the depth of 1 km or more to be store in suitable rock formations. A 60% efficient carbon capture system will still result in 4 kg of CO_2 per kg of hydrogen, meaning that 70 Mt of hydrogen produced using SMR with CCS would still result in 280 Mt of CO_2 emitted to the environment every year. These factors motivate the development of renewable hydrogen generation techniques.

1.2.2. Future hydrogen applications

Recent years have seen increasing interest in hydrogen as an alternate energy source for applications like transportation, energy storage etc. Fuel cell electric vehicles powered by hydrogen are an attractive low carbon alternative to petrol/diesel powered vehicles. They can be a preferable option for medium to heavy duty transport such as the freight sector where battery powered vehicles are currently limited due to shorter range and longer refuelling times [7]. Based on the current scale of production and use, it can still be termed as an application in the development stage with a promising future.

Automobile companies and others have developed fuel cell cars and buses that are already available commercially and concept designs for the future. Germany launched Cordia-iLint, the world's first fuel cell passenger train for commercial purposes in 2018 and is currently expanding it at other places [8, 9]. Recently, airbus revealed three zero-emission commercial aircraft designs relying on hydrogen fuel, which it hopes to enter in commercial operation by

2035 [10]. Increasing interest of industries and recent advancements shows promising future towards developing hydrogen fuel cells-based vehicles.

Hydrogen also has the potential to be used as a substitute to natural gas for domestic power and heating requirements. Already established gas pipelines can be modified for the purpose. Another key advantage of the direct power to hydrogen conversion is the ease of storing hydrogen on a large scale, which enables the system to manage the large variations in energy demands as well as allowing for inter-seasonal storage to meet seasonal demand peaks. But low roundtrip efficiency of ~47 % limits is use [11].

Critically, hydrogen could also provide us with a way to export renewable energy around the world – from countries that have a lot of it – like Australia, to countries that do not have enough. Hydrogen can be stored and exported at a relatively low cost compared to renewable electricity export using high voltage lines. The large number of applications of hydrogen also provides flexibility in terms of its use in the importing country [12].

However, hydrogen can only be used as an alternative fuel to drive decarbonisation if it is made from renewable energy.

1.3. Renewable hydrogen generation

Electrolysis is an electrochemical process that splits water into hydrogen and oxygen, and as such is potentially a CO_2 emission free process if produced using renewable electricity options such as wind and/or solar. **Figure 1.1** shows a schematic of renewable hydrogen generation

using renewable electricity and electrolysers, as well as possible end uses. One of the benefits of hydrogen is, like renewable energy, it can be produced and used on-site in decentralised systems or in a centralised electrolyser system powered by renewable electricity from grid, and then compressed and transported.

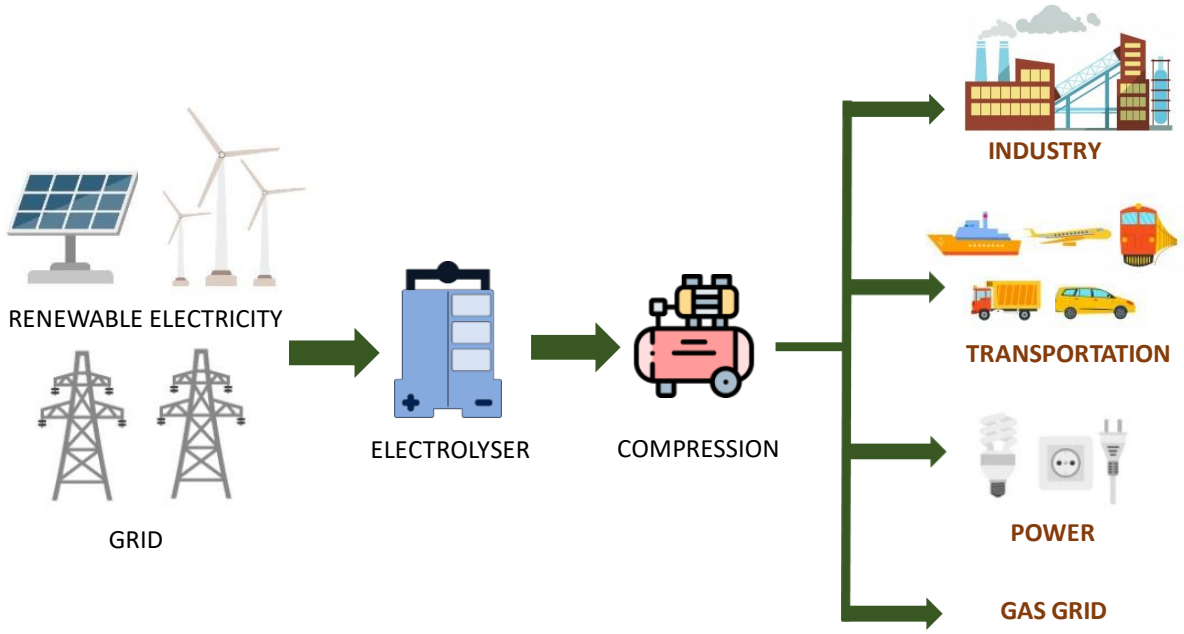

Figure 1.1: Schematic of renewable hydrogen generation using renewable electricity and electrolyser and end use (individual small images- freepik.com)

Presently, less than 0.1% of hydrogen is produced by water electrolysis and is mostly used in applications that require high purity hydrogen, due to its higher cost compared to SMR.

The levelized cost of hydrogen (LCOH) gives the net present cost of hydrogen for a plant over its lifetime. It is an important measure which allows us to assess the scalability and compared different hydrogen production technologies. It is the ratio of the sum of the discounted capital

and maintenance costs over the amount of total hydrogen produced over a lifetime and is given by

$$LCOH = \text{Capital cost} + \frac{\sum_{t=0}^{n} \frac{O\&M}{(1+r)^t}}{\sum_{t=0}^{n} \frac{H_2\ production}{(1+r)^t}} \quad (1.1)$$

Where, n is the plant lifetime, O&M is the operation and maintenance cost, r is the discount rate and t is the year.

According to the IRENA report, assuming a realistic electrolyser capital expense of USD 840/kW, the present LCOH for renewable hydrogen is $4.6/Kg ($ is in USD), using the average cost of wind power with a capacity factor of 46%, and $6.9/kg using the average cost of solar PV power with a capacity factor of 26%. This is much higher than the LCOH for SMR with CCS, ~1.5-$2/Kg [13]. In order for renewable hydrogen generation to be competitive to current fossil fuel-based technologies, further cost reduction is required. Reduction in cost not only requires low-cost renewable electricity for longer durations, but also reduction in electrolyser costs up to 200 USD/kW. The US Department of Energy (DOE), has set LCOH target of 2.3 and $2/kg for distributed and centralised electrolysis system [14]. The Australian government has also set a 'stretch goal' of $2/Kg in the low emissions technology roadmap [15]. Current production costs are much higher than that.

1.4. Direct solar hydrogen generation

Direct solar hydrogen generation (DSHG) is a promising method for renewable hydrogen generation, where solar energy drives the generation of hydrogen and oxygen by molecular

dissociation of water on a catalytic/semiconductor surface [16]. This eliminates the need for separate power generation and electrolyser systems, as well as complex power infrastructure and additional balance of system (BoS), reducing the capital cost and potentially lowering the LCOH. Technoeconomic analysis of different solar hydrogen generation systems has identified solar to hydrogen (STH) efficiency as an important parameter for cost reduction [17]. The US DOE has also set a target STH efficiency of 20% by 2020 to attain economic viability of large-scale solar hydrogen production [18].

Solar hydrogen generation systems involve one or more semiconductor components that are either directly integrated with the catalysts or via wires. These systems generate hydrogen by following three major steps, as shown in **figure 1.2**.

1. The reaction is first initiated by photon absorption in the semiconductor, which generates numerous electron-hole pairs and generates a photovoltage sufficient to drive the water splitting reaction .
2. Those charge carriers then migrate from semiconductor to the surface of the catalysts active sites.
3. Finally, the photo-generated electrons reduce water to form hydrogen, and the holes oxidize water molecules to give oxygen, where the charge transfer occurs through the electrolyte.

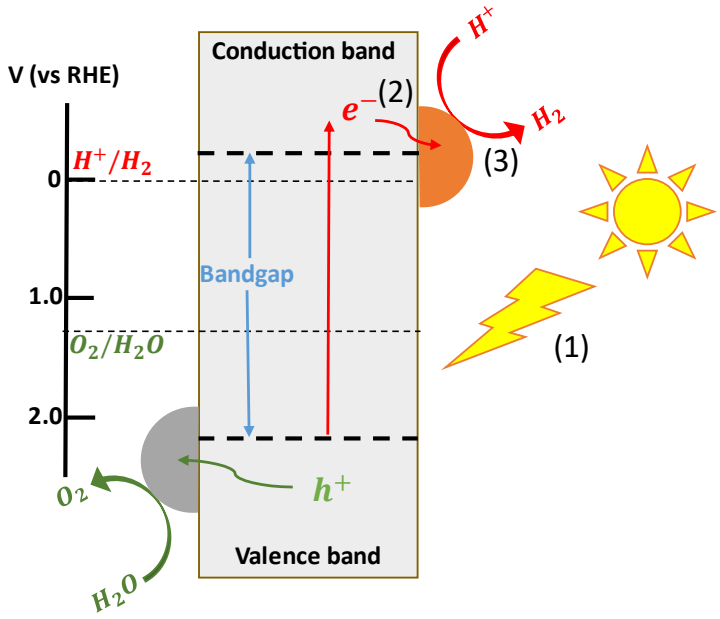

Figure 1.2: Solar water splitting process schematic

The minimum therodynamic potential requirement to drive the water splitting reaction is 1.23V under normal pressure and temperature, but overpotential losses in the photovoltaic (PV) and catalyst system increase the potential requirements to 1.6-2 V [16, 19, 20].

1.4.1. System design/pathways for direct solar hydrogen generation

Different techniques can be applied for DSHG via water splitting and can be broadly classified into two categories: Photochemical system (PC) and, photoelectrochemical system (PEC) as shown in **figure 1.3**.

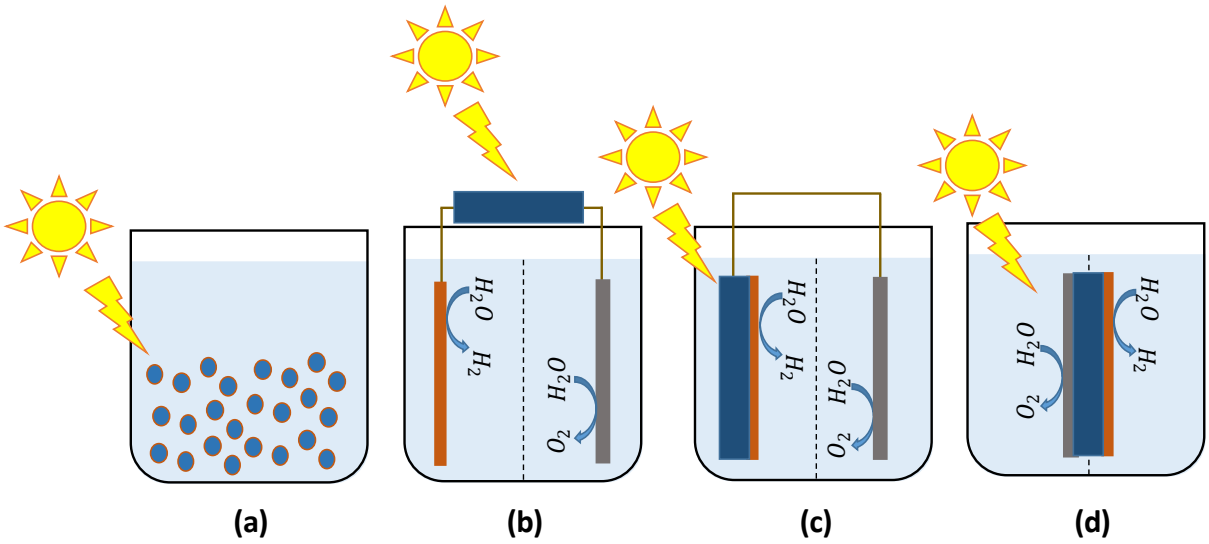

Figure 1.3: Different solar hydrogen generation systems (a) a photochemical system (PC), (b-d) different configurations of photoelectrochemical systems (PEC). The semiconductor is represented in blue, while the hydrogen evolution reaction (HER) and oxygen evolution reaction (OER) catalysts are represented by orange and grey, respectively.

The PC approach uses semiconductor-based photocatalytic particles embedded in the electrolytic solution for direct solar hydrogen generation (figure 1.3 (a)). Though a simple system, it suffers from the following drawbacks, limiting its use for large scale solar water splitting.

Firstly, additional high-cost equipment is required to immediately separate the hydrogen and oxygen gas to avoid any back reactions. This increases the capital cost of the system, thus affecting the LCOH. It is important to make sure that there is minimum contamination and obtained gases have high purity.

Secondly, hydrogen production from this approach suffers from very low STH efficiency compared to other methods, typically an order of magnitude lower (<1%). Semiconductor particles of bandgap more than 2 eV are required to achieve unassisted solar water splitting, reducing the theoretically limiting STH efficiency to below 20% (figure 1.4 (a)). Further unavoidable losses in the photocatalytic component and overpotential losses associated with the reaction reduce the practically achievable efficiency to below 10%.

The disadvantages above severely limit the potential of PC system for low-cost and large-scale hydrogen generation. PEC systems are another possible approach for solar hydrogen generation with the potential to offer high efficiency. A simple PEC system consists of one or more semiconductors in a photovoltaic and/or a photoelectrode configuration integrated directly with a catalyst or connected via wires to the electrodes. Figure 1.3 (b) shows a PV-EC configuration where a photovoltaic cell is placed outside the electrolyte and connected to the electrodes supporting the catalysts via wires. Figure 1.3 (c) shows another configuration where the HER catalyst is directly integrated with a semiconductor photoelectrode and connected to a counter electrode via wires. A monolithic PEC system or artificial leaf system has both the HER and OER catalysts directly integrated with the semiconductor, resulting in a single device for overall water splitting as shown in figure 1.3 (d). Different configurations of PEC approach are discussed in detail in Chapter 2 section 2.4.

Unlike standard PV-electrolysis which employs electrolysers powered by photovoltaic panels connected together with external power management, a PEC system combines the solar energy conversion and electrochemical water splitting directly in a single system [21, 22]. The PEC approach eliminates the need for separate power generation and electrolyser systems, as well

as complex power infrastructure and additional BoS, reducing the capital costs. High STH efficiency also results in cost reduction [18], making PEC a promising approach for low-cost large scale solar hydrogen generation.

1.4.2. Photoelectrochemical hydrogen generation system

For the ideal water splitting reaction without any losses, a voltage of 1.23 V is required to split water into hydrogen and oxygen. However, unavoidable overpotential losses associated with the reaction itself increase the potential requirements to 1.6-2 V.

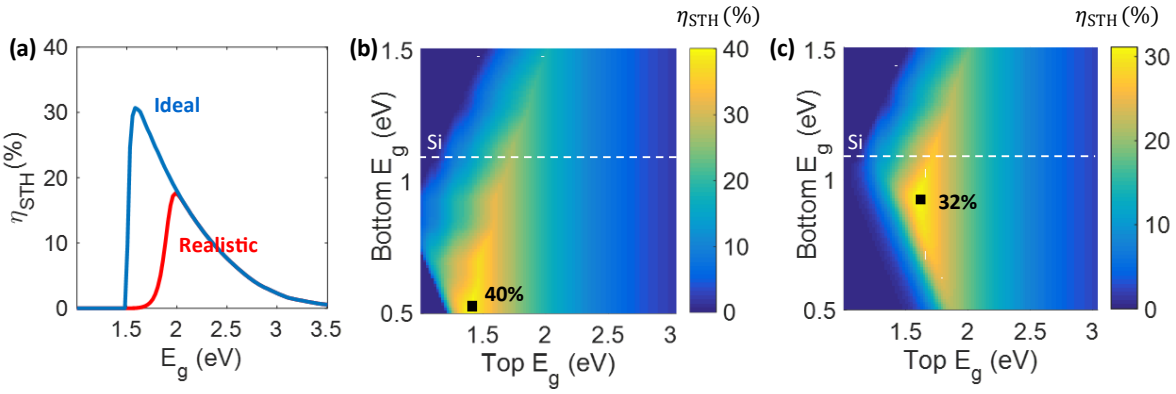

Figure 1.4: Calculated (a) STH efficiency for a single PV cell and catalyst system without (blue) and with (red) the catalytic overpotential losses as a function of semiconductor bandgap (E_g). STH efficiency (η_{STH}) for tandem PV cells in two-terminal configuration without (b) and with (c) the catalytic overpotential losses as a function of top (Top E_g) and bottom (Bottom E_g) semiconductor bandgap. In both the cases ideal PV system without any losses is considered. STH efficiency is calculated using standard solar spectrum (AM1.5G). (Details of the calculations are given in Chapter 2)

In PEC systems, the potential to drive the water splitting reaction is provided by the solar cells/photoelectrodes. The maximum open circuit potential of the solar cell depends upon the semiconductor bandgap. The ideal STH efficiency of a PEC system can be calculated following the detailed balance approach and will be discussed in Chapter 2.

Figure 1.4 (a) shows comparison of STH efficiency for a single PV cell and catalyst system without (blue) and with (red) taking into account the catalytic overpotential losses as a function of semiconductor bandgap. The standard solar spectrum (AM1.5G) is used as the input spectrum, and realistic catalytic overpotential losses are considered, typical of high-performance platinum and iridium-ruthenium catalysts, similar to previously reported work [23]. The thermodynamic limiting STH efficiency for a solar hydrogen generation system using a single semiconductor absorber with optimum bandgap of more than 1.50 eV is close to 30% (blue line). However, when considering overpotential losses in the catalytic system, a bandgap of more than 2 eV is required to achieve unassisted solar water splitting, considerably reducing the maximum STH efficiency to ~17% (red line). Considering further unavoidable losses in the PV components in realistic systems reduces the practically achievable efficiency of systems based on single PV components to 10-15% [19, 23, 24]. As discussed above, a single bandgap semiconductor with bandgap more than 2 eV are required to provide sufficient potential for water splitting reaction. Such high bandgap restricts the amount of solar spectrum that can be absorbed by the semiconductor, limiting the maximum STH efficiency.

Various wide bandgap semiconductors like TiO_2 (3.2 eV), WO_3 (2.6 eV), Fe_2O_3 (2.2 eV) have been extensively studied for unassisted solar hydrogen generation, but their performance is

limited due to restricted absorption (high bandgap), low conductivity, short diffusion length and high overpotentials [25-28].

Low bandgap PV components can also be connected in series to provide sufficient overpotential for unassisted water splitting reaction. Various devices with series connected photovoltaic cells/photoelectrode were reported with efficiency higher than 10%. For example, Luo et al. reported an STH efficiency of 12.3% using bifunctional NiFe catalysts and two series-connected perovskite solar cells[29]; while 13.1% STH efficiency was achieved using GaAs photoelectrodes.[30] Schuttauf et al. reported 14.2% STH efficiency using three series-connected bifacial Si heterojunction cells paired with Ni-based catalysts [31]. Series connected systems offer the opportunity to use efficient low bandgap semiconductors to provide sufficient potential for water splitting reaction. But connecting semiconductors in series reduces the operating current density in proportion to number of series connected cells, limiting the maximum STH efficiency of series connected systems [32].

1.4.3. Photoelectrochemical hydrogen generation systems using tandem solar cells

One way to improve the efficiency is to integrate two semiconductor absorbers with complementary bandgaps in a tandem configuration, to provide sufficient potential to drive the electrochemical water splitting reaction. Tandem configurations using a high bandgap top cell and a low bandgap bottom cell allows more utilisation of the solar spectrum compared to a single bandgap semiconductor [15, 25]. Considering the example of the PV system, the thermodynamic efficiency improves to 40% for two terminal (2-T) tandem cell for an optimum

bandgap combination, compared to around 30% for a single bandgap semiconductor PV [21, 33].

Figure 1.4 (b,c) shows limiting STH efficiencies, without (b) and with (c) catalytic overpotential losses, for a 2-T tandem based system as a function of top and bottom cell bandgap. The same catalytic overpotential losses are considered as in figure 1.4 (a) [23]. The maximum STH efficiency for a 2-T tandem PV based system is 40%, for a top and bottom bandgap combination of 1.4 and 0.5 eV, highlighted by black square in figure 1.4 (b). However, such low bandgap bottom cells suffer from poor material quality and hence low performance. Restricting the choice of bottom bandgap to the range 0.9-1.4 eV, reduces the possible bandgap combinations that achieve STH efficiencies above 30% to a narrow region and requires top bandgaps in the range 1-2.5 eV.

Once again, catalytic overpotential losses increase the voltage requirement to drive the water splitting reaction, reducing the realistically achievable efficiencies to 32% (figure 1.4 (c)). However, it is still possible to achieve the 25% STH target set by US-DOE for DSHG to be cost competitive for large scale hydrogen generation.

There have been many experimental demonstrations based on tandem based systems aiming to achieve low cost, high efficiency direct solar hydrogen generation. Various oxide-based semiconductors such as Fe_2O_3 (2.2 eV) [34, 35], $BiVO_4$ (2.4-2.5 eV) [36, 37], have been explored as photoelectrodes for tandem PEC configuration, coupled with another low bandgap photoelectrodes. Non-ideal bandgap combinations have limited the STH efficiency of these systems. In order to improve the STH efficiency, tandem configurations with photoelectrode

and a PV cell combination have also been explored. A $BiVO_4$ photoanode was combined with perovskite PV cell achieving an STH efficiency of 4.3% [38]. Similarly, Park et. al. developed a PV/PEC tandem device with $WO_3/BiVO_4$ heterojunction photoanodes combined with a dye-sensitised solar cell, realizing an STH efficiency of up to 7.1% [39] [40]. These materials are cheap and easy to fabricate, and a potentially low-cost option for solar hydrogen generation. However, the bandgap combinations available, and losses in the PV and catalytic components limit the STH efficiency of such systems to less than 10% (figure 1.4 (b, c)).

Tandem PV cells based on high cost III-V semiconductors have long been explored to achieve high efficiency solar water splitting. Their favourable bandgap combinations and high PV efficiencies makes them promising candidates to achieve high STH efficiency. Khaselev and Turner reported a III-V tandem PV components-based PEC system for the first time in 1998, achieving 12.4% STH efficiency with a GaInP top cell and GaAs bottom cell [41]. Improvements in material growth techniques resulted in STH efficiencies of 16.2% for GaInP/GaInAs tandem structures. Further improvement in the material quality and surface passivation resulted in record STH efficiencies of 19.3% under 1 sun illumination for a monolithic PEC system [42].

Directly coupled III-V tandem PV-electrolyser systems under concentrated irradiation have also been used for solar hydrogen generation. Peharz et.al. reported a STH efficiency of 12.8%, under 500 suns for a GaInP/GaInAs tandem based PV system [43]. A record STH efficiency over 30% was achieved with a GaInP/GaAs/GaInNAsSb cell and 2 series connected electrolysers under 42 suns [44].

Regardless of the impressive STH efficiencies reported in literature, the use of expensive semiconductors and/or noble-metal catalysts will likely reduce their economic viability for large scale solar hydrogen generation [17, 45].

As discussed above, oxide-based semiconductors are cheap and easy to fabricate but suffer from STH efficiencies below 10%, whereas III-V based systems that have demonstrated experimental STH efficiencies of more than 19% under 1 sun are too expensive for large scale implementation. Large scale solar hydrogen generation requires low-cost alternatives that can simultaneously provide higher efficiencies.

1.5. Perovskite-silicon tandems-based photoelectrochemical system for low-cost, high-efficiency direct solar hydrogen generation

Silicon (Si) solar cells dominate the PV market, with close to 95% of total PV installations are currently based on Si technologies [46]. With record Si solar cell efficiencies already close to theoretically achievable efficiency limits [47], the PV community is looking into Si-based tandems as a viable option for increasing the efficiency above 30% [48, 49].

Properties like bandgap tunability, high absorption coefficient and low sub-bandgap absorption coefficient make perovskite solar cells based on organic-inorganic halides a favourable top cell for Si based tandem solar cells [49-52]. Moreover, the abundant availability of constituent elements and low-cost solution-based processing, suggests that production cost could be low at large scale [53-55]. The first report of perovskite solar cells was published in 2009, with the

power conversion efficiency (PCE) of 3.8% [56]. This efficiency rose rapidly over the years, with the current record PCE of 25.5 % [57].

With the potential to use perovskite as top cells in combination with Si in tandem configurations, efforts have also been devoted to developing semi-transparent high bandgap perovskite cells. In 2014, Bailie et. al. reported a semitransparent perovskite solar cell and mechanically stacked perovskite-silicon tandem solar cell with 17% PCE [58]. Subsequently they reported the first monolithic perovskite/Si tandem solar cell with PCE of 13.7% [59]. Increasing research interest in perovskite-silicon tandems has led to rapid improvements in the efficiency, with a current record PCE of 29.52% PCE [60] for monolithic tandems and 27.7 and 30.5% for mechanically stacked tandems using interdigitated back contact (IBC) and bifacial type of Si bottom cells respectively [61, 62].

The International Technology Roadmap for Photovoltaics predicts that perovskite-Si tandem solar cells will be in mass production as early as 2021, paving the way for low cost, high efficiency tandem cells in the near future [63]. The high efficiency and commercial dominance of Si-based tandems can be leveraged for large scale implementation of commercial PV-based solar hydrogen generation.

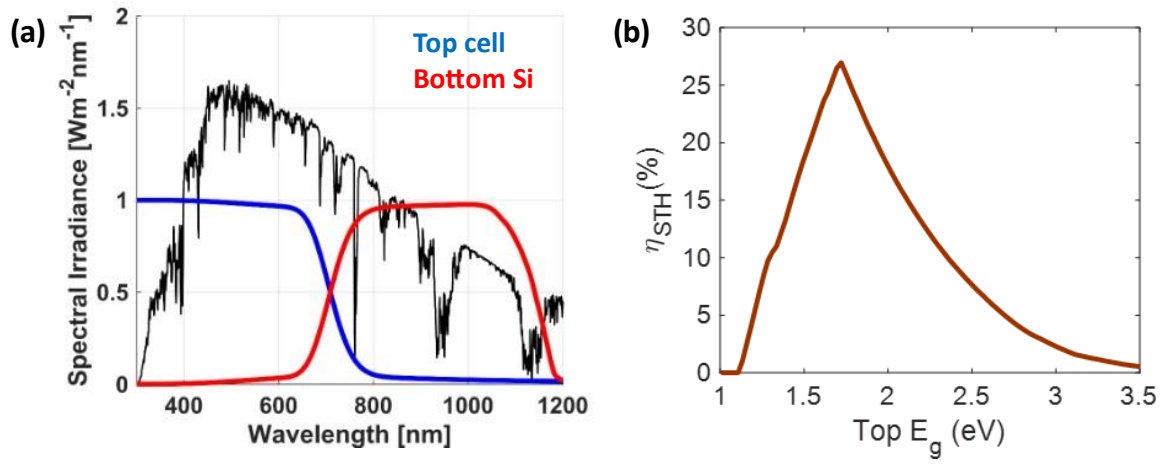

Figure 1.5: (a) Absorption spectrum of tandem PV cell with bottom Si cell (b) Thermodynamic STH efficiency (η_{STH}) of solar hydrogen generation system with two-terminal tandem configuration with bottom Si cell, as a function of top cell bandgap. Ideal STH efficiency is calculated using standard (AM1.5G) solar spectrum, and catalytic system with no overpotential losses. (Details of calculations are discussed in Chapter 2)

Figure 1.5 (b) shows the thermodynamic STH efficiency (η_{STH}) of tandem PV based systems with bottom Si cell, as a function of top PV bandgap. Thermodynamic STH efficiency greater than 25% is possible for top PV cell with bandgap in the range of 1.6-1.8 eV. Perovskite-Si tandem PV cell offers promising opportunity to achieve high STH efficiency and low-cost large scale hydrogen production. Recent efficiency improvements in perovskite-Si tandem PV cells and increasing research towards further improvement in efficiency and stability can be directly leveraged for large scale solar hydrogen generation. In particular, thermodynamic limiting efficiency of more than 25%, opens up realistic possibilities to achieve DOE targets for PEC solar hydrogen generation using low-cost systems [18].

Recent advances in the development of low-cost, DSHG systems using the perovskite-Si tandem PV have shown promising STH efficiencies approaching 18% on the lab-scale [64-67]. However, despite good progress, further advances are required to achieve STH efficiencies above 20% with low-cost materials.

1.6. Earth abundant catalysts for photoelectrochemical hydrogen generation

The best-known water splitting electrocatalysts for OER and HER are the noble metal-based catalysts, such as Ir/Ru for OER and Pt for HER [68]. However, scarcity and high cost of the noble metals contributes to increasing the overall hydrogen production costs from the solar water splitting [69]. Replacing these materials with earth abundant catalysts is one of many ways to reduce the production costs and make the system more feasible for industrial scale implementation. The development of low-cost, earth-abundant metal-based electrocatalysts with similar performances to the noble metals is critical to increasing the overall STH efficiency, thereby reducing the LCOH.

The first-row transition metals, such as Ni, Fe, Co, have shown promising OER and HER performance [70-78]. Alloying 3-d transition metals has been known to further improve their electrocatalytic activity, superior to the individual activities of pure metals. Nickel alloyed with other metals has received extensive attention due to their excellent OER/HER activities and stability under harsh alkaline conditions [71-73, 75, 76]. Although earth abundant catalysts have shown promise, their performance and operational stability need to be further improved in order to match with PV cells and construct robust, high efficiency DSHG systems.

1.7. Thesis outline

This thesis aims to develop perovskite-Si tandem PV/photocathode devices and earth abundant catalysts for low cost, high efficiency unassisted solar hydrogen generation systems. We focus on developing both the photovoltaic and catalytic components, as well as optimum configuration strategies, for overall improvement in the STH performance. Apart from experimentally investigating these systems, this thesis also advances understanding of the fundamental limitations in these systems and proposes methods to overcome them to improve the STH efficiency.

In Chapter 2, we will work towards establishing an understanding of various physical processes occurring in solar hydrogen generation system. We further describe theoretical models to analyse ideal and realistic solar hydrogen generation systems.

In Chapter 3, we discuss the design strategies for Si photocathode. We introduce the experimental methods and fabrication techniques, used in Chapter 4 and 6 to experimentally demonstrate high efficiency perovskite-Si tandem and earth abundant catalysts based solar hydrogen generation systems.

In Chapter 4, we develop a high efficiency Si photocathode with charge selective passivation layer integrated with earth abundant catalysts for hydrogen evolution reaction. Sputter based earth abundant catalysts are developed for direct integration with the silicon photocathode. Using a physical deposition method allows catalyst fabrication to be integrated easily with PV fabrication and allows the possibility of scaling up the manufacture of the system. An overall

water splitting efficiency of 17% is achieved for a PEC system when combined with earth abundant OER catalyst and perovskite solar cell in PV-PEC configuration.

In Chapter 5, we introduce a new theoretical approach to quantify the losses in PV-based solar hydrogen generation systems and assess the potential of loss mitigation techniques to improve the STH efficiency. We develop a temperature-dependent system model to evaluate the relative potential of two techniques to mitigate these losses: decoupling the PV system; and thermal integration. We show that optimal system configuration strategies provide more than three times the STH efficiency increase of thermal integration at high operating temperatures. Combining both techniques results in predicted STH efficiencies approaching 20% for low-cost perovskite-Si tandem-based systems with earth abundant catalysts at realistic working temperatures.

In Chapter 6, we demonstrate a low-cost material system consisting of perovskite/Si tandem semiconductors and Ni-based earth-abundant catalysts for direct solar hydrogen generation. We achieve a record 20% STH efficiency for a PEC system in PV-EC configuration. In addition, we have assessed the potential for further improvement in STH efficiency. We analyse the improvements in STH efficiency by employing loss mitigation technique of decoupling proposed in Chapter 5. Further improvements in the perovskite cell are considered as a function of different loss parameters and resultant improvement in PCE and STH efficiency is studied. A technoeconomic analysis is performed to calculate the current and future levelized cost of hydrogen and assess the cost competitiveness of direct solar hydrogen generation for large scale hydrogen generation.

In Chapter 7, we summarise the main findings and analysis from the thesis and discuss the future research pathways towards realising the goal of large-scale solar hydrogen generation.

Chapter 2

The Theory of Solar Hydrogen Generation

2.1. Introduction

In this Chapter, we will work towards establishing an understanding of various physical processes occurring in solar water splitting systems. A PEC system for direct solar hydrogen generation can be divided into two main parts defined by their role in the hydrogen generation process: the PV components responsible for the conversion of light to electrical energy; and the electrochemical (EC) components which mediate the conversion of electrical energy to chemical energy. We start by discussing the theory of the water splitting reaction in section 2.2. In section 2.3 we discuss solar hydrogen generation systems models, various approaches mentioned in the literature and their limitations. We then describe a solar hydrogen generation model to calculate limiting and realistic efficiencies. Section 2.4 covers different configurations and their impact on system performance.

2.2. Theory of the water splitting reaction

Water splitting is a chemical reaction where hydrogen and oxygen is produced by molecular dissociation of water on a catalytic/semiconductor surface [16]. The overall water splitting reaction in an alkaline electrolyte can be written as

$$4H_2O + 4e^- \rightleftharpoons 2H_2 + 4OH^- \qquad E^0_{red} = -0.828\,V \tag{2.1}$$

$$4OH^- + 4h^+ \rightleftharpoons 2H_2O + O_2 \qquad E_{Ox}^0 = -0.401\,V \tag{2.2}$$

E_{red}^0 and E_{Ox}^0 are the reduction and oxidation potentials respectively. For an acidic environment, the appropriate reactions can be obtained by subtracting or adding the dissociation reaction of water into protons and hydroxyl ions:

$$4H^+ + 4e^- \rightleftharpoons 2H_2 \qquad E_{red}^0 = +0.000\,V \tag{2.3}$$

$$2H_2O + 4h^+ \rightleftharpoons 4H^+ + O_2 \qquad E_{Ox}^0 = -1.23\,V \tag{2.4}$$

As discussed in Chapter 1, section 1.4, in the absence of any overpotential losses, the water splitting reaction requires a minimum thermodynamic potential of 1.23 V for the reaction to proceed at room temperature. But in realistic operating conditions, the electrochemical reaction has some additional losses. Additional potential is required to overcome the activation energy barrier and drive the reaction at a desired rate, and results in irreversible activation overpotential losses in the system. Ohmic overpotential losses can also occur due to resistance to the flow of charge in the electrode and electrolyte solution. These overpotential losses increase the potential requirements to 1.6-2 V [16, 19, 20].

An electrochemical system for water splitting consists of series connected hydrogen evolution reaction (HER) and oxygen evolution reaction (OER) electrocatalysts, seperated by an ion-conducting electrolyte and a power source. For a standalone water-splitting system, the voltage required to overcome the reaction potential and additional losses is given by [79]:

$$V_{IN}(J,T) \geq E_{STH}(T) + V_{OER}(J,T) + V_{HER}(J,T) + V_e\,(J,T) \tag{2.5}$$

where E_{STH} is the electrochemical reaction potential which defines the minimum potential required to drive the water-splitting reaction (at a specific temperature, T, and pressure condition); $V_{OER}(J,T)$ and $V_{HER}(J,T)$ are the temperature-dependent activation overpotential losses during the OER and HER respectively; and $V_e(J,T)$ is the resistive voltage loss due to charge transport through the electrolyte.

The minimum electrochemical reaction potential $E_{STH,}$ is calculated using the Nernst equation. The Nernst equation provides a relationship between the potential of an electrochemical reaction and the standard reaction potential, and can be used to calculate the potential of an electrochemical reaction under non-standard conditions:

$$E_{STH} = E_0 + \frac{RT}{nF} ln[\frac{P_{H_2}(P_{O_2})^{0.5}}{P_{H_2O}}] \tag{2.6}$$

where R is the gas constant, T is the operating temperature, n is number of charges involved in the reaction and F is Faraday's coefficient, P_{H_2}, P_{O_2} and P_{H_2O} are partial pressures of hydrogen, oxygen, and water, respectively. The reaction potential under standard conditions, (temperature and pressure) E_0, is determined by the change in the Gibbs free energy, ΔG, as[80]

$$E_0 = -\frac{\Delta G}{nF} \tag{2.7}$$

Both the Gibbs free energy and reaction potential in the electrochemical system are sensitive to the operating temperature. The change in Gibbs free energy of the reaction is due to the change in enthalpy, ΔH^0_{rxn}, and entropy, ΔS^0_{rxn}, of the reaction with temperature [80, 81]

$$\Delta G^0_{rxn} = \Delta H^0_{rxn} - T * \Delta S^0_{rxn} = \Delta H^0(T_0) + \int_{T_0}^{T} \Delta C_P(T)dT - T\int_{T_0}^{T} \Delta C_P \frac{dT}{T} \quad (2.8)$$

where $\Delta H^0(T_0)$ is the enthalpy change at reference temperature, T_0 (298 K), and C_p is the heat capacity at constant pressure. The values above can be calculated by established methods using semi empirical polynomial equations [16]:

$$\int_{T_0}^{T} \Delta C_P(T)dT = \Delta At + \Delta B\frac{t^2}{2} + \Delta C\frac{t^3}{3} + \Delta D\frac{t^4}{4} - \frac{\Delta E}{t} + \Delta F - \Delta H(T_0) \quad (2.9)$$

$$\int_{T_0}^{T} C_P \frac{dT}{T} = \Delta A\, ln\, t + \Delta Bt + \Delta C\frac{t^2}{2} + \Delta D\frac{t^3}{3} - \frac{\Delta E}{2t^2} + \Delta F \quad (2.10)$$

where $t = T/1000$, T is the operating temperature in kelvin.

Any additional overpotential required to overcome the activation energy barrier for the reaction to proceed is calculated by the temperature dependent Butler-Volmer equation. Butler-Volmer equations gives the relation between current density at an electrode and the activation overpotential. It is given mathematically as [80, 82-84]

$$V_{act} = V_{HER} + V_{OER} = \frac{2RT}{nF}\left[sinh^{-1}\left(\frac{J}{2J_{0,anode}}\right) + sinh^{-1}\left(\frac{J}{2J_{0,cathode}}\right)\right] \quad (2.11)$$

where, $J_{0,}anode$, and, $J_{0,}cathode$, are the exchange current density at the anode and cathode, respectively. The exchange current densities for the anode, $J_{0,}anode$, and, cathode, $J_{0,}cathode$, is the rate of oxidation and reduction respectively, and are calculated as

$$J_{0,}anode = \gamma_a \left(\frac{P_{H_2}}{P_0}\right)\left(\frac{P_{H_2O}}{P_0}\right) exp\ (-\frac{E_{act,a}}{RT}) \tag{2.12}$$

$$J_{0,}cathode = \gamma_c (\frac{P_{O_2}}{P_0})^{\frac{1}{4}} exp\ (-\frac{E_{act,c}}{RT}) \tag{2.13}$$

where P_0 is the reference pressure, γ_a and γ_c are the pre-exponential factors and $E_{act,a}$and $E_{act,c}$ are the activation energies of the anode and cathode respectively [80, 83]. A large exchange current density signifies fast reaction kinetics and electron transfer at the electrode and vice-versa [16]. The electrochemical system is modelled based on Nernst and Butler-Volmer equations which predict the behaviour of catalysts over a range of operating conditions. In the next section, we will describe the solar hydrogen generation system model based on detailed balance approach to calculate thermodynamic limiting STH efficiency and realistic efficiencies based on previous approaches.

2.3. Modelling photoelectrochemical system for direct solar hydrogen generation

Developing a theoretical model for solar water splitting, including all the critical photoelectrochemical processes, provides an opportunity to understand optimal material combinations, different design considerations, operating conditions, and allow for a quantitative understanding of the system performance.

In 1977, Ross and Hsaio calculated the efficiency limits of photoelectrochemical solar energy conversion based on Shockley and Quiesser's 'detailed balance limit' for the efficiency of p-n junction photovoltaic devices [33]. For a photoelectrochemical system operating under 1 sun at 20 ℃ they calculated thermodynamic efficiency limit of 29% for single absorber and 41% for a tandem system with two absorbers of optimised bandgaps [85]. Several authors have since developed similar frameworks to identify optimum bandgap combinations for tandem systems [19, 23, 85, 86]. In particular, Fountaine et. al. used analytical equations to develop a photoelectrochemical water splitting device model to calculate the limiting and realistic efficiencies for single and dual tandem absorbers [23]. Other works have demonstrated the importance of considering the effect of different electrical and optical configurations in tandem based systems [32, 87-89]. The operating parameters of the system has also been shown to be an important parameter [90, 91]. In general, these studies have tended to focus on a single aspect of the system design for example, choice of material, operating parameters, or device configuration.

Despite the importance of the studies discussed above, there is still a lack of understanding of the relative importance of different loss mechanisms for solar hydrogen generation systems. Loss mitigation techniques can be employed at different levels in the system to improve the STH efficiency, but generally add complexity and cost to the system. It is necessary to ensure that the most effective loss mitigation techniques are employed, however there have been no studies that systematically compare their potential to increase the performance. In Chapter 5 we perform a quantitative analysis of different losses in a PEC system for DSHG. We further assess the relative improvement in efficiency for different loss mitigation techniques. The literature on modelling the PEC systems will be reviewed critically in Chapter 5. In the next

section, we will use thermodynamic efficiency models to calculate the limiting efficiencies of PEC hydrogen generation systems.

2.3.1. Thermodynamic efficiency limits for direct solar hydrogen generation

We use the detailed balance approach to calculate the absolute limiting efficiencies of single and dual tandem junction PV based direct solar hydrogen generation devices [21, 23]. The total input solar irradiation incident on the PV component is calculated as

$$P_{in} = \int_0^\infty E \cdot \phi(E,T_S,\Omega_{solar})\, dE, \tag{2.14}$$

using Planck's equation to calculate the incoming photon flux from a black body as

$$\phi(E,T,\Omega) = \frac{2\Omega}{c^2h^3}\frac{E^2}{exp\left(\frac{E}{kT}\right)-1}. \tag{2.15}$$

The incoming photon flux is a function of photon energy, E, solid angle, Ω, and temperature, T. Here $c = 3 \times 10^8\ ms^{-1}$, is the speed of light, $h = 6.63 \times 10^{-34} Js$, is the Planck's constant and $k = 1.38 \times 10^{-23} JK^{-1}$, is the Boltzmann constant. To calculate the incident solar flux we take, $\Omega_{solar} = 6\ \times 10^{-5}$ as the angular diameter of Sun as viewed from the Earth and $T_s = 6000\ K$ is the temperature of Sun.

For STH efficiency calculations in Chapter 1, and realistic cases discussed in Chapter 5 and 6 AM1.5G solar spectrum is used as incoming solar irradiation and is given as

$$P_{in} = \int_0^{\infty} AM1.5G(E)dE \tag{2.16}$$

In an ideal PV component, all the incoming photons exceeding the semiconductor bandgap energy E_g are absorbed and contribute to the photocurrent as

$$J_L = q \int_{E_g}^{\infty} \phi(E,T_S,\Omega_{solar})dE, \tag{2.17}$$

where q is the elementary charge. The cell emits photons due to radiative recombination which results in the recombination current given as

$$J_{rad} = q \int_{E_g}^{\infty} \phi(E,T_{PV},\Omega_{emit})\, dE, \tag{2.18}$$

where $T_{PV} = 300\ K$ and $\Omega_{emit} = \pi$, are the temperature and the solid angle of emission of the PV component. The current density-dependent photovoltage of the ideal PV cell is then given by

$$V_{PV} = \frac{kT_{PV}}{q} ln\left(\frac{J_L - J}{J_{rad}} + 1\right). \tag{2.19}$$

The maximum power point (MPP) of the PV cell is defined as

$$MPP = \max_{0<J<J_L} V_{PV}(J)J, \tag{2.20}$$

which gives the PCE of the PV cell as

$$\eta_{PCE} = \frac{MPP}{P_{in}}. \tag{2.21}$$

Figure 2.1 shows the current density-voltage (J-V) curve of Si PV cell (red), semi-transparent top PV cell with bandgap 1.72 eV (blue) and Si as a bottom cell under top cell (dashed red) calculated using detailed balance approach discussed above.

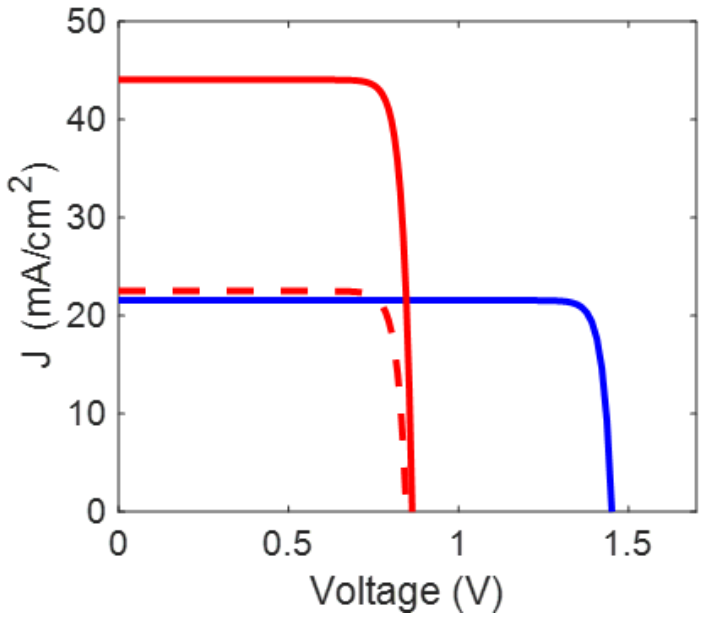

Figure 2.1: I-V curve of Si PV cell (red), top PV cell with bandgap 1.72 eV (blue) and Si as a bottom cell under top cell (dashed red).

To achieve unassisted water splitting the voltage supplied by the PV component should be enough to overcome reaction potential and additional losses as given in equation (2.5) and restated below,

$$V_{IN}(J,T) \geq E_{STH}(T) + V_{OER}(J,T) + V_{HER}(J,T) + V_e(J,T)$$

The STH efficiency, is defined by the fixed thermodynamic potential requirements of the water-splitting reaction (1.23 V) and is then given as

$$\eta_{STH} = \frac{J_{op}\, E_{STH}\, \eta_f}{P_{in}} \tag{2.22}$$

where, J_{op}, is the operating current, η_f is the faradic efficiency, assumed to be unity

The method above was employed to calculate the STH efficiencies as described in Chapter 1. Figure 1.4 details the limiting STH efficiency for a single and two terminal tandem PV and catalyst based solar to hydrogen generation system as a function of the semiconductor bandgaps. The results demonstrate that employing two semiconductors with complementary bandgaps in 2-T tandem configuration can improve the limiting STH efficiency to 40%.

2.3.2. Realistic direct solar hydrogen generation systems

The thermodynamic efficiency calculations are useful in understanding the absolute efficiency limits. However, these calculations give upper bound values of efficiencies and practical systems achieve much lower efficiencies due to inevitable system losses.

Given the dependence of STH on the voltage and overpotential losses, it is important to understand the difference between ideal and realistic efficiencies. As discussed in section 2.2, the electrochemical system suffers from overpotential losses which affect the voltage requirements for water splitting reaction. The PV components suffer from non-ideal diode characteristics which affect its photovoltage and photocurrent output.

Several authors have calculated realistic PV and STH efficiency by including the non-ideality factors associated with photovoltaic and catalytic components, which provides a better approximation of practically achievable device efficiencies.

Fountaine introduced five different loss parameters to calculate realistic efficiencies: semiconductor absorption fraction, semiconductor external radiative efficiency, series resistance, shunt resistance and catalytic exchange current density. These parameters directly affect light absorption, charge transport and catalysis [23]. This work provided a framework to analyse previously reported limiting efficiencies and parameters limiting the device performance. In Chapter 5 we expand on this work to take into account temperature dependence and different loss mitigation techniques.

2.4. Different configurations of photoelectrochemical system for direct solar hydrogen generation

A wide variety of configurations have been reported in literature for PEC systems. Jacobsson, in their work, established that all these different configurations are essentially equivalent as they follow same fundamental physical process regardless of the system configuration [88]. Although the physical design of different systems is considerably different based on how the semiconductor, catalyst and electrolyte are integrated, the solar to hydrogen conversion process in all the systems follow same underlying physics. The solar energy is converted to electrical energy by the photovoltaic effect and then the electrical energy is converted into chemical energy. Beck further developed a framework to rationally compare the performance of different configurations and optimise the system performance [21].

This thesis will discuss a range of different configurations for PEC systems, and it is instructive to include an overview here. In this section we will summarise the different configurations reported in literature and compare them based on the framework developed by Beck [21].

In a coupled PEC system, the two PV cells are connected in series with each other in 2-T configuration and with the EC components through wire or an interface, such that the same operating current (J_{op}) is flowing through all the components (Figure 2.2).

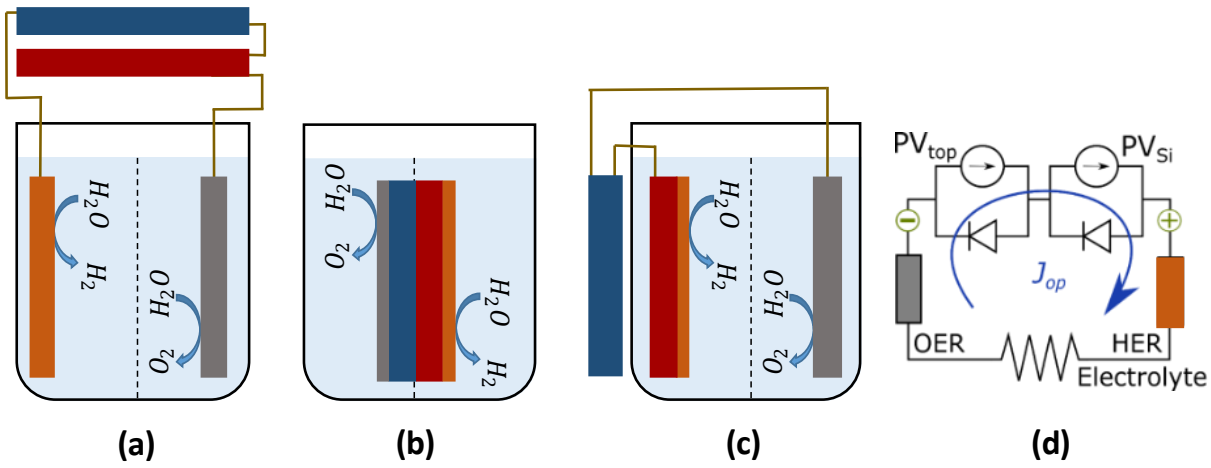

Figure 2.2: (a-c) Schematic and (d) equivalent circuit of coupled configuration. Top PV cell is represented by blue, bottom PV cell by red, HER by orange and OER by grey colour.

For a coupled PV-EC configuration the tandem PV cell is connected to the EC components via wires as shown in **figure 2.2** (a). A monolithic PEC configuration (also known as artificial leaf system) is also in the coupled configuration, where the catalyst is directly integrated on the PV cells, but still connected in series with same current flowing through all the components (figure 2.2(b)). In the intermediate PV-PEC configuration a photoelectrode is directly integrated to a

catalyst and additional PV cell is connected externally via wires (figure 2.2(c)). All the above three systems are essentially equivalent as they can be represented by the same equivalent circuit (figure 2.2 (d)).

It is possible to decouple the EC and PV components by connecting the tandem PV cell to a power management unit (PMU), which in turn is wired to the EC components, as shown in **figure 2.3** (a)) [21].

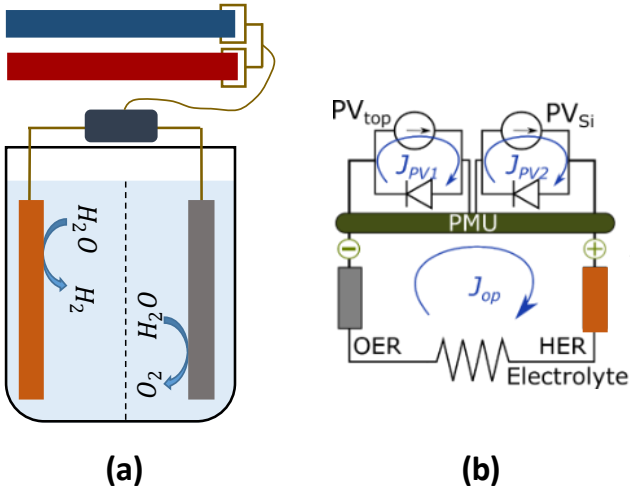

Figure 2.3: (a) Schematic and (b) equivalent circuit of decoupled configuration. Top PV cell is represented by blue, bottom PV cell by red, HER by orange and OER by grey colour.

The two PV components are connected independently to the PMU (known as a four-terminal (4-T) configuration). The PV cells can then be operated at their respective maximum power points (MPP) while the PMU optimises the current and voltage provided to the EC components. This can be represented by an equivalent circuit in figure 2.3(b). The resultant voltage for different system configurations can be summarized as

Coupled: $V_{IN}\left(J_{op}\right) = V_{PV,1}\left(J_{op}\right) + V_{PV,2}(J_{op})$

4-T PV decoupled system: $V_{IN}\left(J_{op}\right) = \frac{MPP_1 + MPP_2}{J_{op}}$

where MPP_1 and MPP_2 are maximum power operating points of the top and bottom PV cells. Optimising the system configuration can improve the STH efficiency. Decoupling the system eases the requirements for bandgap combinations to achieve high STH efficiency. Decoupled systems also have the potential to achieve higher STH efficiency compared to coupled systems for identical PV materials and catalysts[21]. But they require more complicated wiring and a power management unit, which will add to complexity and cost. We will discuss methods to increase STH efficiency in detail in Chapter 5.

2.5. Conclusion

To summarise, the PEC system can be divided into PV and EC components, based on their roles in the hydrogen generation process. The minimum thermodynamic potential required for water splitting reaction is 1.23 V but overpotential losses increase the potential requirements to 1.6-2 V. To achieve unassisted solar hydrogen generation, the PV component is required to provide enough potential to overcome minimum thermodynamic potential and additional overpotential losses.

We describe the model to calculate thermodynamic and realistic efficiency limits of direct solar hydrogen generation system. The thermodynamic efficiency calculations are useful in understanding the absolute efficiency limits, but these calculations give upper bound values of

efficiencies. Realistic efficiency calculations are important to understand the practically achievable limits and inevitable system losses. The electrocatalytic component is modelled using Nernst and Butler-Volmer equation. The ideal PV component is modelled using detailed balance approach, and realistic PV component is modelled by introducing various loss parameters to account for the non-idealities in the PV system.

We further discuss various PEC system configurations discussed in literature. Different configurations for solar hydrogen generation are reported in literature with PV and EC components either connected through wires or directly integrated through surface. These configurations are essentially similar with all the components connected in series and same current flowing through them. It is possible to decouple the EC and PV components by connecting the tandem PV cell to a power management unit (PMU), which in turn is wired to the EC components. This eases the current and voltage matching requirements between the PV and EC components.

The ideal and realistic solar hydrogen generation model and various solar hydrogen generation configuration form the basis of further detailed analysis in the upcoming Chapters in the thesis.

Chapter 3

Experimental Methods

3.1. Introduction

This Chapter will cover the key experimental fabrication and characterization techniques used in this thesis in the development and analysis of perovskite-Si tandem PV based solar hydrogen generation systems. Section 3.2 will give an overview of different c-Si solar cell designs and the development of Si photocathodes used in this thesis. It includes a brief overview of the limitations of Si photocathodes and different strategies explored in this thesis to overcome them. Section 3.3 will introduce the experimental process used to fabricate different components of the solar hydrogen generation system which includes Si solar cells (Chapter 4 and 6), Si photoelectrodes, sputter deposited earth abundant catalytic systems (Chapter 6), and perovskite-Si tandem configuration (Chapter 4 and 6). Section 3.4 will cover the solid state, electrochemical and photoelectrochemical characterisation techniques used for experimental analysis (Chapter 4 and 6).

3.2. Introduction to silicon photocathodes

In recent years, passivated emitter rear contact (PERC) cells have emerged as the most successful Si solar cells for commercial implementation, due to their high efficiency, good performance under variable temperature and light conditions, and relatively cheap fabrication costs. Si solar cell efficiencies of 26.7% have been reported on lab scale, very close to its

maximum achievable efficiency limit [92]. The efficiency of commercial Si based modules have improved to above 24% on lab-scale and 22% on industrial scale [93, 94]. According to International Technology Roadmap for PV-2020, around 60% of the global Si based PV technologies are of the PERC cell family, with diffused and passivated p-n junctions and passivated rear side [95]. **Figure 3.1** shows the schematics of some of the most common silicon cell structures: PERC, PERL, and PERT, which will be discussed below.

In 1976, Green and Godfrey developed metal insulator semiconductor (MIS) solar cells at University of New South Wales (UNSW) [96]. These cells had continuous passivation at the front via a thin oxide layer, allowing charge tunnelling between the metal contact and the Si cell. Blakers and Green reported 16% efficiency for an improved MIS design with light surface phosphorus diffusion (MINP) in 1981, further improving it to 18% by 1984 [97, 98].

Inspired by the low area metal contact at the surface, it was realised that reducing the metal-Si contact area at the rear would help in reducing the rear-surface recombination, thus improving the cell efficiency. In 1988, Blakers reported cells with a passivated emitter and rear cell (PERC) structure, shown schematically in figure 3.1(a), with PCE of 22-23 % [99, 100]. The optical and recombination losses at the rear of the PERC structure were reduced by using an Al reflector on top of a dielectric passivation layer. An array of small holes was used to make contact between the Si and rear Al metal, covering around 1% of the rear surface, while the rest was passivated with the dielectric layer.

To further improve on the PERC cell performance, a boron diffusion was performed at the rear Si surface underneath the Al reflective contact. The passivated emitter rear totally diffused

(PERT) structure, shown schematically in figure 3.1(b), had a boron diffusion on the entire rear surface, while the passivated emitter and rear locally diffused (PERL) structure, in figure 3.1(c), had local diffusions only at the point contacts.

The PERT and PERL cell structures provide excellent light trapping, better fill factor due to optimised design, reduced recombination due to better surface passivation and high minority carrier lifetimes, [101, 102] and resulted in improved efficiencies of 24-25% [101, 103-106].

Most of the initial solar cell research focussed on cells with p-type base wafers due to better tolerance to damage due to radiation, lower temperature requirements for phosphorus doping to form p-n junctions, and uniform resistivity along length. Research in the last few years have shown that n-type Si has certain advantages over p-type Si. N-Si has higher carrier lifetime compared to p-Si due to absence of boron oxygen defects, and are resistant to light induced degradation [107]. Cells with n-type substrates with reverse doping polarities (p^+nn^+) have also achieved efficiencies close to 26% [92, 108].

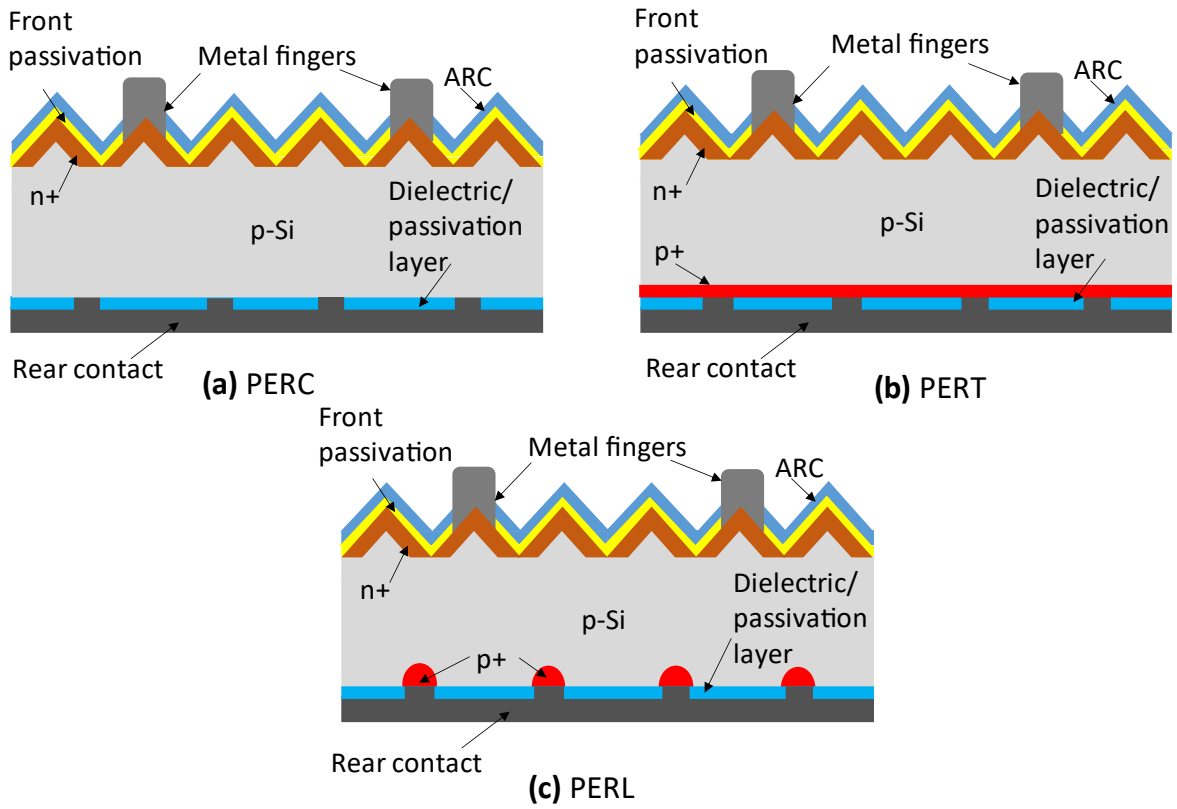

Figure 3.1: Schematic of (a)PERC (b)PERT and (c)PERL cell structures

Leveraging the existing success of Si cells, we develop high performance Si photocathodes by modifying standard PERT structures. Owing to superior performance, high quality and possibility of large-scale production, this structure is a preferable choice to design Si photocathodes. While the front is kept identical to the PERT/PERL structure, the rear surface was modified to develop photocathodes for hydrogen evolution reaction. This design decouples light absorption, occurring at the front, from the catalytic reaction, occurring at the rear, and reduces the photocurrent losses from parasitic light absorption [64, 109]. Owing to requirement of electrons for hydrogen evolution reaction at the catalytic site, a p^+nn^+ buried junction is

formed with n-Si base wafer, and catalyst at the n+ rear. A thin titanium interlayer is deposited at the n^+ rear surface to improve catalyst adhesion, followed by catalyst deposition.

Since Si photocathodes are unstable in alkaline solution and corrode quickly, the photocathode needs to be protected from the electrolyte solution. The front metal contacts are unstable in electrolyte and are protected by encapsulation using glass cover. The rear is protected by the Ti/catalyst coating. **Figure 3.2** shows the schematic of Si photocathode.

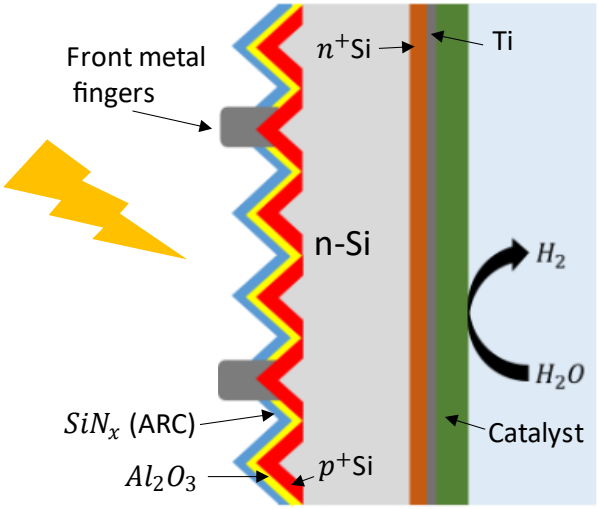

Figure 3.2: Schematic of Si photocathode

3.3. Silicon photocathode limitations and practical solutions

The performance of Si photocathodes is limited by slow reaction kinetics at its surface [110]. Employing a HER catalyst can substantially improve the performance [111]. Noble metal Pt is the best reported HER catalyst, but its low availability and high cost limits its use for large scale applications. While the previous reports of earth-abundant catalyst integrated Si

photocathodes have achieved efficiencies above 10%, they have relied on microstructures or wet-chemical methods-based catalyst synthesis [112-114] which are less compatible with the current industrial PV manufacturing [115]. Using wet chemical methods require Si encapsulation and metal layer deposition at the rear before electrodeposition to avoid corrosion during the electrodeposition process under harsh conditions.

Enabling low-cost DSHG based on Si photoelectrodes at large scale requires a transition towards earth abundant catalytic systems fabricated using processing techniques that can be easily integrated into the current PV industrial fabrication methods, while maintaining high STH efficiencies. Physical deposition techniques facilitate the deposition of thick and compact catalytic films, and also enable effective chemical protection of Si from the electrolyte [115, 116]. However, so far Si photocathodes integrated with physically deposited earth abundant catalysts have had limited performance, resulting in the photoelectrode efficiencies below 5% due to lack of optimisation of physically deposited catalysts [117-119].

In this thesis we develop high performance Ni based, bimetal catalysts using magnetron co-sputtering. Sputter deposition allows fast deposition of thick and compact high quality catalytic films [115] that can also provide chemical protection against corrosion of Si in electrolytic environment. It also provides precise control over the chemical composition, film thickness, morphology, provides good adhesion. Sputter deposition is a physical depositon method that is already used in the semiconductor industry allowing facile ntegration with the current Si PV manufacturing techniques [116]. Catalyst development and performance analysis is covered in detail in Chapter 4.

Recombination losses at the Si/catalyst interface is another key limitation for the Si photocathode performance. Capping the Si surface with a passivation layer can help improve the overall performance by reducing the charge recombination. Metal oxide semiconductors such as Al_2O_3 and TiO_2 have been widely explored for protection/passivation of Si photoelectrodes due to their stability in electrolytic solutions [120-122]. Although these layers provide better protection against corrosion, their passivation performance is still limited compared to similar layers employed in the solar cells. In this thesis we report for the first time Si photocathodes with industrially relevant poly-Si based charge selective passivating contacts. This provides electrical passivation against charge recombination at the Si/catalyst interface and electron selectivity for HER. Si photocathode and passivation layer fabrication and performance analysis is discussed in detail in Chapter 4.

The sections below give an overview of the Si photocathode and solar cell fabrication methods (3.3.1), catalyst deposition (3.3.2), photocathode encapsulation (3.3.3), perovskite-Si tandem configurations (3.3.4), and characterisation techniques (3.4) used in Chapter 4 and 6.

3.4. Device Fabrication

3.4.1. Silicon photocathode and solar cell fabrication

Silicon photocathodes and solar cells were fabricated following the procedure below for experiments performed in Chapters 4 and 6. **Figure 3.3** shows the flow chart of the major steps involved in Si solar cell and photocathode fabrication.

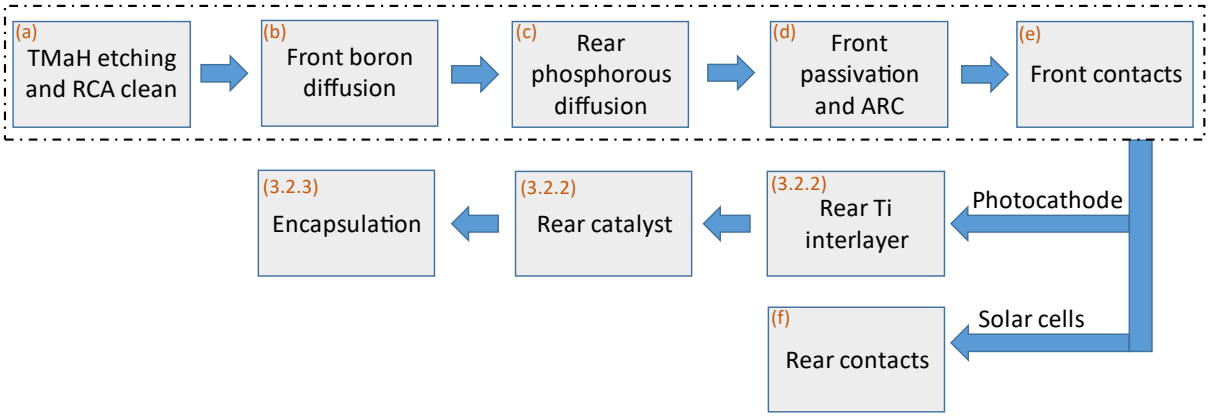

Figure 3.3: Flow chart of the major steps involved in Si solar cell and photocathode fabrication.

(a) Wafer etching and cleaning

N-Si wafers with 100 orientation and 0.5-1.5-ohm cm resistivity are used for solar cell and photocathode fabrication. The samples are etched in TMaH (tetramethylammonium hydroxide) solution at 80 ℃ for 10 minutes followed by standard RCA (radio corporation of America) cleaning prior to photocathode fabrication.

(b) Front diffusion and texturing

The formation of p^+n junction in the front consists of two different boron diffusions. The first is light and covers the front cell area to form p^+n junction. The second is heavy p^+ diffusion and is deposited beneath the contact fingers to reduce resistance.

A SiO_x/SiN_x mask is deposited on the front and rear of the wafer to define the cell area in the front for p^+ diffusion and protect the rear area. The thin SiO_x layer is deposited by ramping the

temperature of the furnace up to 666 ℃ followed by ramping down in the furnace under oxygen flow. The SiN_x layer is deposited using low pressure chemical vapour deposition (LPCVD) (CVD equipment corporation). Photolithography is performed to open cell area for front p^+ diffusion, using AZ 4620 photolith.

The p^+ region on the front (illumination) side is doped with boron, formed by by thermal diffusion of BBr_3 in an automated furnace (tempress systems, model 594). Boron doping is performed at 850 ℃ for 30 minutes followed by drive in under oxygen at 955 ℃ for 1 hour and oxidation for 20 minutes before cooling down in nitrogen upto 700 ℃. Masking layer is then removed by HF fuming.

The samples are RCA cleaned and a SiO_x/SiN_x mask is deposited following the same method as above, followed by photolithography to open selective area under the metal fingers. Random pyramid texturing in the active cell area in the front is formed, using TMaH and monotex solution at 75 ℃ for 13-15 minutes.

A heavily doped p^{++} region is formed under the front metal fingers. The wafers are RCA cleaned followed by masking using $SiO_x/SiN_x$and photolithography to open selective area. Boron doping is performed at 930 ℃ for 35 mins followed by oxidation for 40 mins before cooling down to 700 ℃ under nitrogen. This resulted in formation of p^+n junction in the front. The front SiO_x/SiN_x masking layer is removed by Hydrogen fluoride (HF) fuming.

(c) Rear diffusion

A phosphorus diffusion is performed to form the n^+n junction at the rear of the cell. Samples are first RCA cleaned followed by the deposition of a SiO_x/SiN_x mask to protect the front surface following the same method as above, followed by photolithography to open rear area. n^+ region is formed at the rear by thermal diffusion of $PoCl_3$ at 820 ℃ for 25 mins followed by oxidation at 900 ℃ for 40 mins before cooling down to 700 ℃ under nitrogen. This results in formation of n^+n junction at the rear.

(d) Front passivation and antireflection coating (ARC)

A SiN_x/Al_2O_3 dielectric stack is deposited on the front boron doped textured surface to provide antireflection and surface passivation. The Al_2O_3 layer is deposited by thermal atomic layer deposition (ALD) (Beneq, TFS200). Wafers are subjected to around 200 ALD cycles at 200 ℃, resulting in deposition of around 20 nm of conformal Al_2O_3 surface passivation layer. Around 70-80 nm of SiN_x anti-reflection layer is deposited using plasma enhanced chemical vapour deposition (PE-CVD) (Roth and Rau AK400) followed by forming gas anneal (FGA) at 425 ℃ for 25 minutes.

(e) Front metal contacts

The front metal grid and busbar are defined by photolithography on top of the previously defined p^{++} regions, followed by metal deposition. Chromium/palladium/silver are deposited for the metal grid and chromium/silver for busbars using standard thermal evaporation (Varian thermal evaporator).

(f) Rear metal/catalyst deposition

For Si solar cell samples, the rear is coated with silver, while for photocathodes, the catalyst is deposited at the rear following the method discussed in the next section. For Si solar cell samples, 900 nm silver is deposited for rear contact. Solar cells and photocathodes are then subjected to silver (Ag) plating to thicken front metal fingers to 12-15 um. The rear side of the photocathodes is protected by spin-coating AZ-4620 photolith layer to avoid any Ag electroplating.

3.4.2. Catalyst deposition

Fabrication details of catalysts and Ti interlayer used in Chapter 4 are discussed below

(a) Titanium layer

A Ti layer is used to improve catalyst adhesion on the Si photocathodes. The Ti layer is deposited using (Ti pellet 99.99%) by electron-beam evaporation (Temescal BJD-2000). The chamber is evacuated to 1e-5 Torr and metal layer is deposited at the rate of 1 As^{-1} at room temperature. The film thickness is confirmed using ellipsometry.

(b) Sputtered Nickel and Platinum

Pt and Ni catalysts are deposited using Pt (99.99%) and Ni (99.99%) targets respectively, by DC sputtering (AJA international). The process chamber is evacuated to 4 mTorr and flow of working gas argon is kept at 20 sccm during the deposition process. The substrate is rotated

continuously for uniform deposition and is maintained at room temperature through the process. The deposition power for Ni is 150 W, resulting in deposition rate of 9.8 $\mathrm{nm\,min^{-1}}$. and for Pt is 200 W, resulting in deposition rate of 10.1 $\mathrm{nm\,min^{-1}}$. The film thickness is confirmed using ellipsometry.

3.4.3. Silicon photocathode sample preparation

As mentioned above, the front contacts of the Si photocathode need to be protected from corrosion by coming in contact with electrolyte. Silicon photocathode encapsulation is performed following the procedure below for experiments described in Chapter 4.

External contact for performing photoelectrochemical measurements is formed by soldering silver wire on the front silver busbar. The front is then encapsulated using glass and epoxy (Hysol 9460). The front glass used for encapsulation is cut and cleaned thoroughly in soapy water, deionised (DI) water, acetone, isopropanol (IPA) and ethanol followed by drying through nitrogen gun. Epoxy is also used to define the rear catalytic area, ensuring it to be similar to front illumination area. Samples are then vented under fume-hood for 24 hours for epoxy to dry before any measurements.

3.4.4. Perovskite-Si tandem PV cells

Perovskite cell fabrication is discussed in Appendix section C. In Chapter 4, perovskite-Si tandem for unassisted direct solar hydrogen generation system is fabricated by placing wide bandgap semi-transparent perovskite PV as a top cell in 2-T configuration with bottom Si

photocathode in PV-PEC configuration. In Chapter 6, perovskite-Si tandem solar cell in 2-T configuration is used in PV-EC configuration. Details of configuration and performance are discussed in the relevant Chapters.

3.5. Characterisation techniques

The performance and properties of the as developed Si and perovskite solar cells, Si photocathode and catalyst system are analysed using a variety of solid-state and photoelectrochemical techniques. The performance of individual perovskite and Si cells, as well as tandem cells, are analysed using solid state current-voltage (J-V) and external quantum efficiency (EQE) measurements. Photocathode and catalyst are assessed using photoelectrochemical (PEC) and electrochemical (EC) measurements like linear sweep voltammetry (LSV), electrochemical impedance spectroscopy (EIS), chronopotentiometry (V-t) and chronoamperometry (J-t). The morphology of the Si photocathode and catalysts are investigated using scanning electron microscopy (SEM), transmission electron microscopy (TEM) and X-ray diffraction (XRD). The chemical composition of catalysts is analysed using X-ray photoelectron spectroscopy (XPS) and EDAX.

The section below discusses the key characterisation techniques mentioned above, covering their requirements, experimental setups, sample preparation, measurement process and specifications.

3.5.1. Solid state characterisation

(a) Current-voltage measurements

The performance of the individual perovskite and Si solar cells and perovskite-Si tandem cells is analysed by solid state current-voltage (I-V) measurements. Several important performance parameters such as open circuit voltage (V_{oc}), short-circuit current (J_{sc}), fill factor (FF) and power conversion efficiency (PCE) are determined by J-V curve.

The current–voltage characteristics are measured using a solar simulator (#WAVELABS SINUS-220) equipped with a potentiostat source (AutolabPGSTAT302N). The light intensity is calibrated at one sun ($100 mWcm^{-2}$, AM1.5G) using the certified FraunhoferCalLab reference cell. Unless stated otherwise, the scan rate is fixed at 50 mVs^{-1} with a voltage step of 10 mV and dwell time of 200 ms.

(b) External quantum efficiency (EQE) measurements

External quantum efficiency is the ratio of charge carriers collected by the solar cell to the total number incident photons of a given energy. EQE spectra is obtained using a homemade setup without light bias in DC mode, including a tungsten light source, a monochromator SP AB301-T, two Keithley 2425 source-meters, and a Si reference cell. The system is calibrated by the National Institute of Standards and technology (NIST)-certified reference Si and Ge photodiodes.

3.5.2. Electrochemical and photoelectrochemical characterisation

The performance of individual Si photocathodes is analysed by photocurrent measurements in a three electrode configuration under standard solar (AM 1.5G) illumination. The photocurrent response of the photocathode is proportional to the amount of hydrogen produced and can be used as a benchmark parameter to analyse the performance. For catalysts, similar current response measurements are performed without any light source.

Three electrode measurements are composed of a working electrode/photoelectrode (investigated electrode), a counter electrode (Pt plate) and a reference electrode (Ag/AgCl) to evaluate the electrochemical/photoelectrochemical HER activity of the developed materials in an alkaline solution (1 M potassium hydroxide (KOH)). **Figure 3.4** shows the schematic of the three- electrode measurement setup.

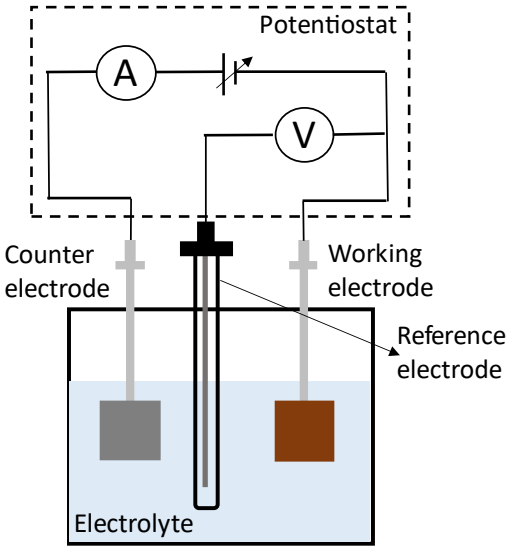

Figure 3.4: Schematic of three electrode measurement setup

The Ag/AgCl potential is converted to RHE (reversible hydrogen electrode) following Nernst equation stated below

$$V_{RHE} = V_{Ag/AgCl} + V_{0_{Ag/AgCl}} + 0.059\,V \times pH \tag{3.1}$$

where, $V_{Ag/AgCl}$ is the working potential measured using Ag/AgCl reference electrode, $V_{0_{Ag/AgCl}} = 0.197\,V$ is the standard potential of Ag/AgCl reference electrode at 25 ℃, and pH is the electrolyte solution pH. For optimizing catalytic performance, the overpotential value at 10 mAcm^{-2} current density is compared.

Applied bias to photon conversion efficiency (ABPE) is calculated in case of Si photocathode, using the following equation:

$$ABPE = \frac{V_{max}(V_{RHE}) \times J_{max}(mAcm^{-2})}{P_{in}(mWcm^{-2})} \tag{3.2}$$

where, V_{max} and J_{max} are the voltage and current density at maximum power point and P_{in} is the power density of incident irradiation (100 mWm^{-2}). Overall performance of the perovskite-Si tandem based system for direct solar hydrogen generation is analysed using a two electrode configuration. STH efficiency is calculated using equation (2.22), Chapter 2 and restated below:

$$\eta_{STH} = \frac{J_{op}\, E_{STH}\, \eta_f}{P_{in}}$$

where, J_{op}, is the operating current, η_f is the faradic efficiency, assumed to be unity

Electrochemical and PEC performance are studied using a solar simulator (#WAVELABS SINUS-220) equipped with a potentiostat source (AutolabPGSTAT302N). Photocathode measurements are performed in dark and under AM 1.5G illumination and in dark for catalysts. The light intensity is calibrated at one Sun (100 mWm^{-2}, AM1.5G) using the certified Fraunhofer CalLab reference cell. A platinum plate of size one by one cm is used as a counter electrode and silver/silver chloride (Ag/AgCl) is used as a reference electrode for all the three electrode measurements unless stated otherwise.

(a) Linear sweep voltammetry (LSV)

The linear sweep voltammetry (LSV) is the photocurrent/current response of either the two or three electrode configuration as discussed above.

(b) Chronoamperometry

Chronoamperometry measurements can demonstrate the stability of photocathode/catalyst or its performance over a period of time. The photocurrent/current measurements are performed at the fixed applied potential as a function of time. The resultant J-t plot is used to evaluate the stability of the photocathode/catalyst.

Chronoamperometry measurements for catalysts are performed at 10 $mAcm^{-2}$ in 1 M KOH in a three-electrode configuration with Carbon counter electrode. Chronoamperometry measurements of Si photocathodes are performed at 0 V vs RHE in 1 M KOH in three electrode configuration under 1 sun (AM1.5G) illumination.

(c) Chronopotentiometry

Chronopotentiometry measurements are similar to chronoamperometry measurements and are used to analyse the stability of catalyst or its performance over a period of time. The measurements are performed at a fixed current density and the overpotential required to maintain that current is measured over a period of time.

Chronopotentiometry measurements for catalysts are performed at 20 $\mathrm{mAcm^{-2}}$ in 1M KOH in three electrode configuration with carbon counter electrode and SCE reference electrode. Chronopotentiometry measurements for both HER and OER is also performed at 10 $\mathrm{mAcm^{-2}}$ in two electrode configuration.

3.5.3. Morphology and compositional analysis

(a) X-ray diffraction (XRD)

X-ray diffraction (XRD) provides information about crystal structure and chemical composition of the material. XRD analysis is performed using a PANalytical Empyrean II diffractometer with Cu Kα radiation. The samples for XRD analysis are prepared on $\mathrm{Si/SiO_x}$ substrates unless stated otherwise.

(b) Scanning electron microscopy (SEM)

The surface and cross-sectional morphology of the catalyst, photocathode and perovskite solar cell were analysed using scanning electron microscopy (SEM). The SEM images provide

information about the surface topography and composition of the sample. SEM analysis is performed using FEI Nova NanoSEM 450 FE systems. The samples for SEM analysis are prepared on Si substrate unless stated otherwise.

(c) Transmission electron microscopy (TEM) and Selected area electron diffraction (SAED)

The transmission electron microscopy (TEM) and selected area electron diffraction (SAED) analysis provides information about the morphology, crystal structure, chemical composition of the material. TEM and SAED analysis of the Si photocathode and catalysts was performed using JEOL JEM-F200 systems.

(d) X-ray photoelectron spectroscopy (XPS)

X-Ray photoelectron spectroscopy is used to identify the elemental composition analysis of material. The surface chemical properties and elemental composition of the catalysts are studied by XPS using a Thermo ESCALAB250i high-resolution X-ray photoelectron spectrometer.

(e) Ultraviolet-visible spectroscopy

The reflectance and transmittance are measured using a Lambda 1050 spectrophotometer (Perkin Elmer) equipped with an integrating sphere.

Chapter 4

Silicon Photocathodes with Carrier Selective Passivated Contacts, and Earth Abundant Catalyst for High-Performance, Low-Cost, Direct Solar Hydrogen Generation

4.1. Introduction

In this Chapter, we develop Si photocathodes with charge selective passivation and physically deposited earth abundant catalysts with an efficiency above 10%. A standalone PEC system in PV-PEC configuration is demonstrated by integrating the Si photocathode with a perovskite solar cell in 2-T tandem design, and a NiFe OER anode, achieving an exceptional STH efficiency of 17%. Section 4.2 introduces the background literature of Si photocathodes integrated with earth abundant catalysts, including the limitations of the current technology. Section 4.3 describes earth abundant HER catalysts in brief. We use magnetron co-sputtering to deposit conformal films of NiMo/Ni HER catalyst, with low HER overpotentials of 89 mV at 10 $mAcm^{-2}$ on planer substrates. Sputtering is a physical deposition technique and has the potential to integrate into current Si manufacturing processes for large scale production. The catalyst fabrication and electrochemical performance analysis is discussed in section 4.4. We further develop high-performance Si photocathodes, incorporating state-of-the-art charge selective passivation and earth abundant catalysts, with an ABPE of over 10%, covered in section 4.5. We separate the requirements of protection and passivation, by employing a Si dioxide and n doped polycrystalline Si (SiO_X/n^+ poly-Si) charge selective passivation layer,

combined with a continuous, thick metal catalyst layer on the rear of the photocathode to provide protection against corrosion in the electrolyte. The SiO_X/n^+ polycrystalline Si charge selective passivation layer improves the Si photocathode ABPE by 70% relative to the same photocathode without any passivation, highlighting the important effect of recombination at the Si/catalyst interface on the efficiency. Unassisted water splitting is demonstrated in section 4.6, by combining a semi-transparent, wide bandgap perovskite solar cell in a 2-T tandem design with the Si photocathode, and a NiFe OER anode. The perovskite PV cell used in this work was fabricated by Dr. The Duong, at The Australian National University, and the NiFe anode fabrication and characterisation was performed by Peng Liu, at Tsinghua University. The text in the Chapter is adapted from a paper which is under preparation and is co-authored by Astha Sharma, The Doung, Peng Liu, Doudou Zhang, Di Yan, Christian Samundsett, Heping Shen, Siva Karuturi, Kylie Catchpole and Fiona J. Beck.

4.2. Silicon photocathodes for hydrogen evolution

As discussed in Chapter 2, Si is an attractive candidate for constructing high efficiency photocathodes for solar water splitting because it has a suitable bandgap (~1.1 eV) to harvest solar energy, and a compatible conduction band edge to enable the hydrogen evolution reaction [111]. Unassisted solar hydrogen generation has already been achieved by integrating Si photocathodes with wide bandgap top cell resulting in efficiencies over 17% [64, 123-125] for PEC systems with noble metal catalysts. In addition, Si solar cells have reached more than 90% of their theoretical efficiency [126], and currently dominate the global solar energy market with close to 95% of the total PV installations based on Si technologies [95]. The impressive

advances in performance and manufacturing that have made this possible can be leveraged for solar water splitting.

Silicon photocathodes can be fabricated from standard Si solar cells by replacing the rear contact with metal catalysts. This design decouples light absorption, occurring at the front, from the catalytic reaction, occurring at the rear, and avoids the photocurrent losses from parasitic light absorption in the catalyst [64, 109]. High ABPE of more than 15% has been achieved for Si photocathodes integrated with noble metal catalysts [64, 127-129].

As discussed in Chapter 3 section 3.3, catalyst deposition techniques should be compatible with current industrial PV manufacturing processes to enable PEC systems to leverage existing fabrication infrastructure and reduce costs [130]. Although there have been many reports of high-performance earth abundant catalysts integrated with Si photocathodes, most of the approaches involve wet chemical methods, like electrodeposition, which are less favourable for large scale fabrication [112, 113]. So far, earth abundant catalysts fabricated using industrially relevant physical deposition methods have shown limited performance, with ABPE below 5 % due to lack of optimisation of physically deposited catalysts [117-119].

Charge recombination at the Si/catalyst interface is another key limitation for the Si photoelectrode. Thus, achieving high performance requires effective electronic passivation and chemical protection. Passivating the Si surface defects by using dielectric layers can improve the electrical performance. TiO_x has been widely studied as a carrier selective passivating contact chemical protection layer for Si photoelectrodes due to its high stability in electrolyte solution and low conduction band offset assisting the collection of electrons [128, 129, 131].

However, fabrication conditions are critical for the film quality and formation of charge trap states in TiO_x limits its surface passivation [121, 132]. Non-conducting passivating layers such as Al_2O_3 and SiO_x have also been investigated for passivation of Si photoelectrodes [120, 122, 133, 134]. However, the thickness of the passivating interlayers must be less than 2 nm to allow carrier transport via electron tunnelling, which is insufficient for adequate surface passivation [132]. In Si solar cells, this problem is solved by introducing localised contacts, and the non-contacted regions are passivated with state-of-art dielectric layers like SiN_x [135]. But high series resistance due to smaller contact area, complex fabrication steps, and limited catalyst coverage restricts its application in photoelectrodes [135, 136].

Carrier selective passivating contacts based on ultrathin SiO_x, and heavily doped polycrystalline Si (poly-Si) can overcome these issues in Si photoelectrodes which simultaneously providing good surface passivation and the carrier selectivity. The Si solar cells employing SiOx/poly-Si have achieved efficiencies more than 25% on an industrial scale and 26.1% on small scale [137-139]. Even though these types of passivating contacts are already used in high efficiency solar cells, there are no reports to demonstrate their use in photoelectrodes.

4.3. Nickel based earth abundant catalysts for hydrogen evolution reaction

Ni based alloys have received extensively explored as an alternative to noble metal catalysts due to their excellent OER/HER activities and stability under harsh alkaline conditions [71-73, 75, 76]. Various Ni based binary metal alloys such as NiMo [73, 140, 141], NiCo [142, 143], NiFe [144-146], NiW [144, 147, 148], NiCu [149, 150], NiZn [151] have been reported in

literature. Raj et. al. concluded the following activity trend of Ni-based binary metal alloys for Hydrogen evolution reaction in alkaline environment Ni-Mo > Ni-Zn > Ni-Co > Ni-W > Ni-Fe > Ni-Cr > Ni-plated steel [152]. This finding was corroborated by recent results of NiMo HER electrocatalysts with a remarkable HER activity with low overpotentials of 17 mV at 10 $mAcm^{-2}$[73]. Although Ni-based catalysts are a promising HER candidate, most of the high-performance systems reported in literature, involve chemical and solution-based processes like electrodeposition and hydrothermal methods [73, 140, 141] making them less compatible with current industrial PV manufacturing process [115, 116]. In the research described below, we develop an NiMo HER catalyst using dc-magnetron sputtering method. Sputtering is a physical technique used to prepare thin films, where film parameters can be engineered by closely controlling deposition parameters. Being a physical deposition method, it provides the flexibility to integrate it into current Si cell manufacturing processes [115, 116].

4.4. Sputter deposited hydrogen evolution reaction catalysts

4.4.1. Catalyst fabrication and optimisation

The deposition of the various HER catalysts studied here is carried out using dc-magnetron sputtering (AZA international). The process chamber is evacuated to 4 mTorr and the flow of working gas Ar is kept at 20 sccm during the deposition process. The substrate is rotated continuously for uniform deposition and is maintained at room temperature throughout the process. Pt, Ni and Mo catalysts are deposited using Pt (99.99%), Ni (99.99%) and Mo (99.99%) targets, respectively. Binary metal Ni-Mo films are prepared by co-sputtering Ni (99.99%) and Mo (99.99%) in a multisource dc-sputtering instrument. The deposition power

of Ni is kept constant at 150 W and the deposition power for Mo is varied to obtain Mo at ratio from 0% to 100% in Ni-Mo alloy.

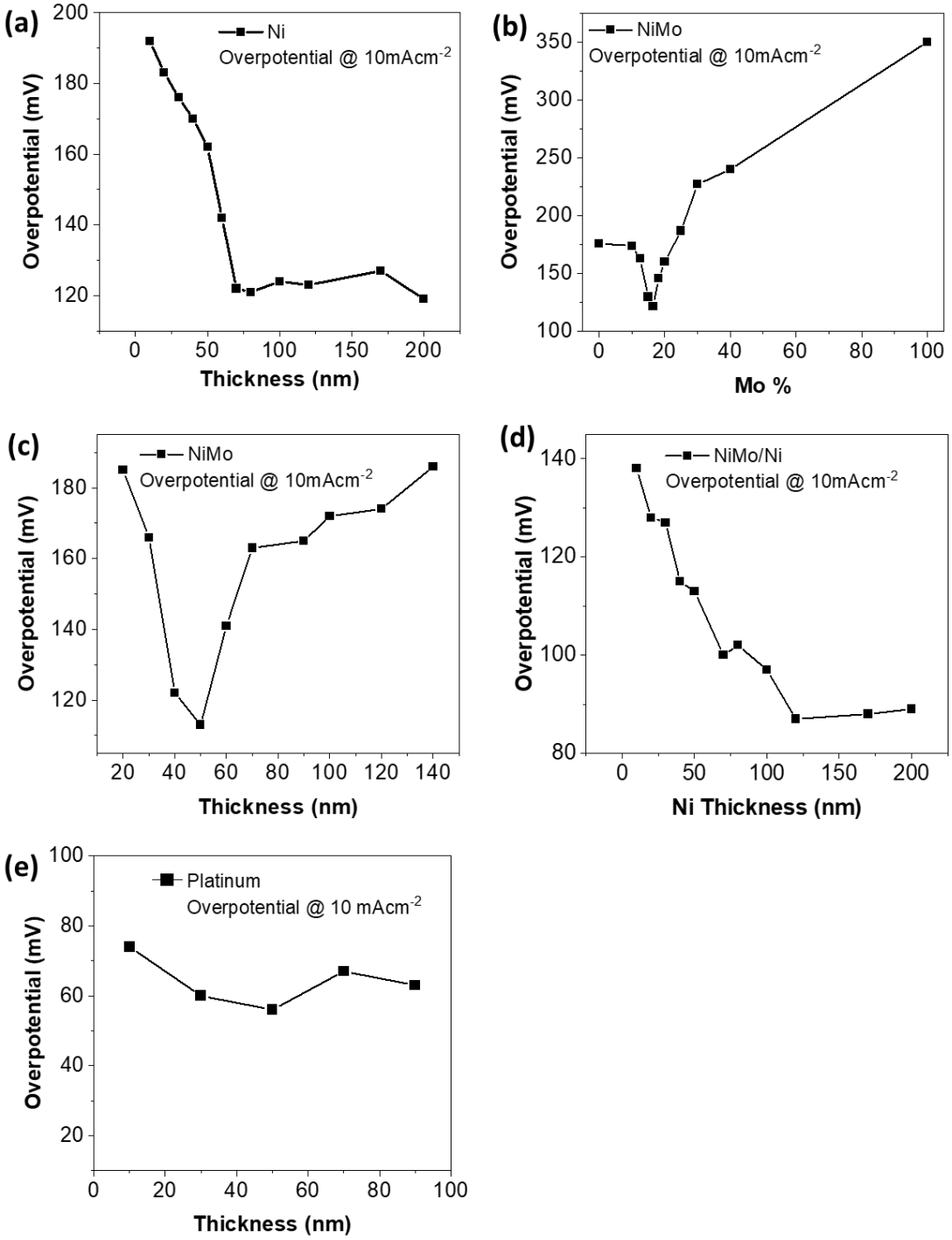

Figure 4.1: Overpotential at 10 $mAcm^{-2}$of sputter deposited (a) Ni catalyst with different thickness (b) NiMo with different ratios (fixed thickness) (c) NiMo with different thickness (fixed ratio) and (d) NiMo/Ni with different Ni interlayer thickness on FTO substrates. (e) Overpotential of sputter deposited Pt catalyst with different thickness on FTO substrate

Figure 4.1 shows the NiMo/Ni catalyst thickness and composition optimisation. The performance of the bimetal alloy is compared to the in the individual constituent metals, as well as Pt as a benchmark, and the thickness of Ni and Pt are also optimised. The thickness is determined using a surface profilometer and optimised by changing the the deposition time. The NiMo ratio is controlled by varying the sputter gun power. Three electrode linear sweep voltammetry measurements are carried out to determine the overpotential of catalysts at 10 $mAcm^{-2}$ for catalyst with different thickness, and ratios in the case of NiMo. A ratio of Ni(83.5%)Mo(16.5%) is found to be optimum with an overpotential of 113 mV at 10 $mAcm^{-2}$. Adding a Ni interlayer further improves the catalyst performance, reducing the overpotential to 89 mV at 10 $mAcm^{-2}$.

4.4.2. Morphology and composition analysis of sputter deposited NiMo hydrogen evolution reaction catalysts

Figure 4.2 (a) and (b) show the top and cross-sectional SEM images of the NiMo catalyst film on a Si substrate. The NiMo forms a conformal film with fine granular structures on the surface. Figure 4.2 (c) and (d) show the top and cross-sectional SEM images of the NiMo catalyst film with a Ni interlayer on Si substrate. Adding a Ni interlayer results in formation of a cauliflower-like structure, with noticeably bigger surface features compared to pure Ni or Mo

(supplementary section, figure S 4.1) or only NiMo (figure 4.2 (a)) film. The supplementary section is at the end of the Chapter. The cross-sectional SEM image of NiMo/Ni in figure 4.2 (d) further reveals that the NiMo/Ni catalyst films form non-conformal nanorod structures. The nanorod morphology of NiMo/Ni allows concentrated porosity in perpendicular direction to the substrate, supporting effective transport of reactants to the catalyst sites [144, 153]. The three-dimensional structure significantly enhances the surface area available for HER reaction and improves the catalytic performance.

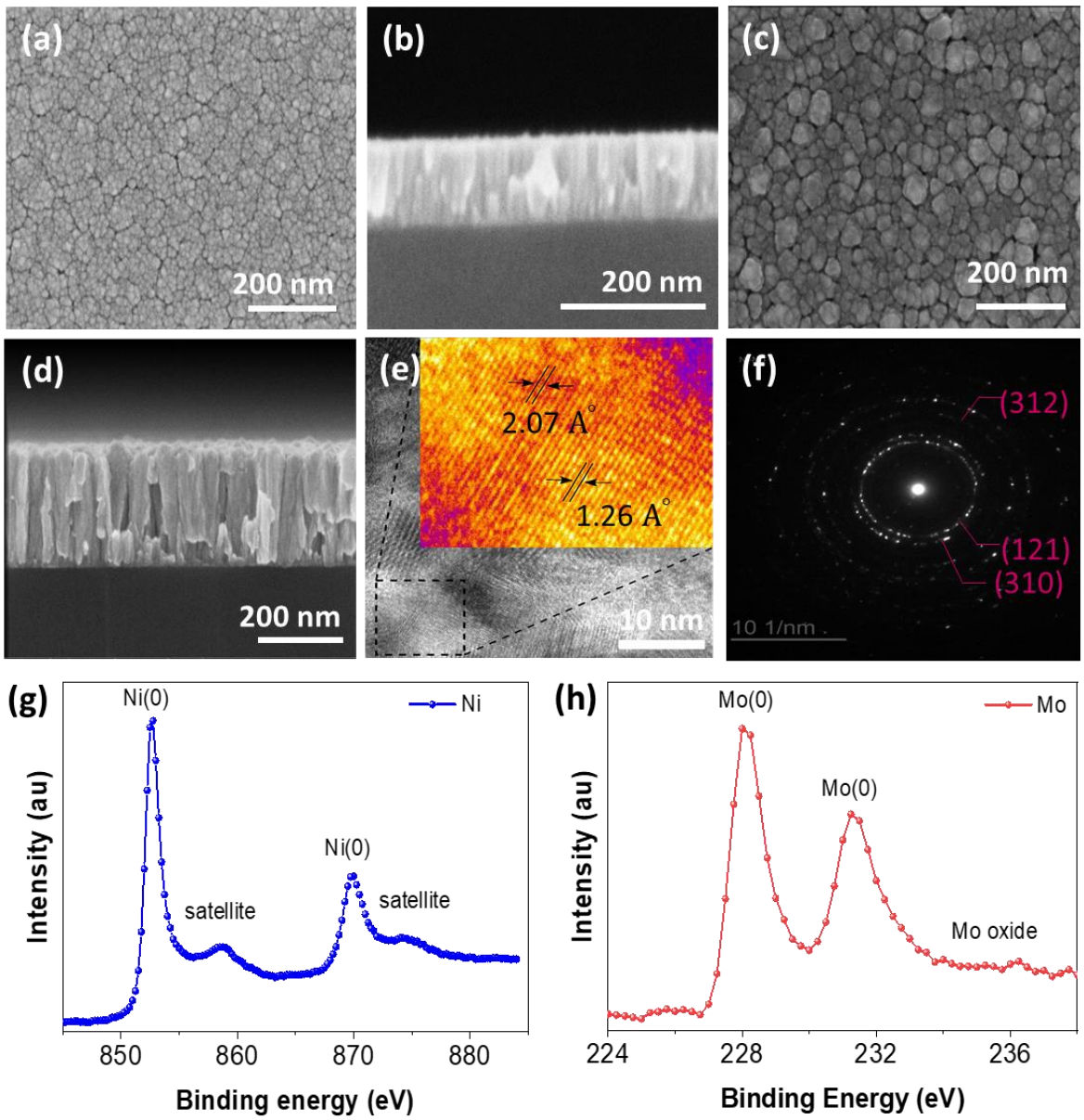

Figure 4.2: Surface and cross-sectional scanning electron microscopy (SEM) image of (a,b) NiMo and (c,d) NiMo/Ni, (e) high resolution transmission electron microscopy (HR-TEM) image of NiMo, (f) selective area diffraction (SAED) pattern of the NiMo/Ni, x-ray photoelectron spectra (XPS) of (g) Ni 2p and (h) Mo 3d on Si substrate.

Figure 4.2 (e) shows the HR-TEM image of NiMo film on a Si substrate. The coloured inset is the magnified image of the selected area with false colouring for better contrast. The inset image shows clear lattice fringes with interplanar spacing of 2.07 Å and 1.26 Å, corresponding to the (121) and (312) planes of $MoNi_4$. The crystal planes are oriented in random directions suggesting polycrystalline structure of the film. Figure 4.2 (f) shows the selective area diffraction (SAED) pattern of the NiMo/Ni film. The concentric-circular rings with broad halos and irregularly located diffraction dots further confirms the polycrystalline structure of the film. The diffraction rings are indexed to (310), (121), and (312) planes of $MoNi_4$, which is further confirmed by XRD patterns (figure S 4.2).

A surface chemical composition analysis of NiMo film is performed using XPS as shown in figure 4.2 (g) and (h). The Ni 2p XPS spectrum peaks in figure 4.2 (g) correspond to metallic Ni(0) (852.63 eV and 869.9 eV), and satellite peak (858.65 eV). Similarly, the Mo 2d XPS spectrum peaks in figure 4.2 (h) are attributed to metallic Mo(0) (228 eV and 231 eV) and MoOx (236 eV). Compositional analysis of XPS spectra reveals Ni:Mo ratio of 4:1 confirming presence of $MoNi_4$ alloy.

4.4.3. Electrochemical performance of sputter deposited NiMo HER catalysts

The electrochemical performance of the sputter deposited HER catalysts is measured in 1 M KOH electrolyte, in a three-electrode configuration. The LSV current-voltage curves for the NiMo alloy with and without the Ni layer are shown in **figure 4.3** (a) and are compared to plain Ni and Mo, as well as sputter deposited Pt metal as a benchmark.

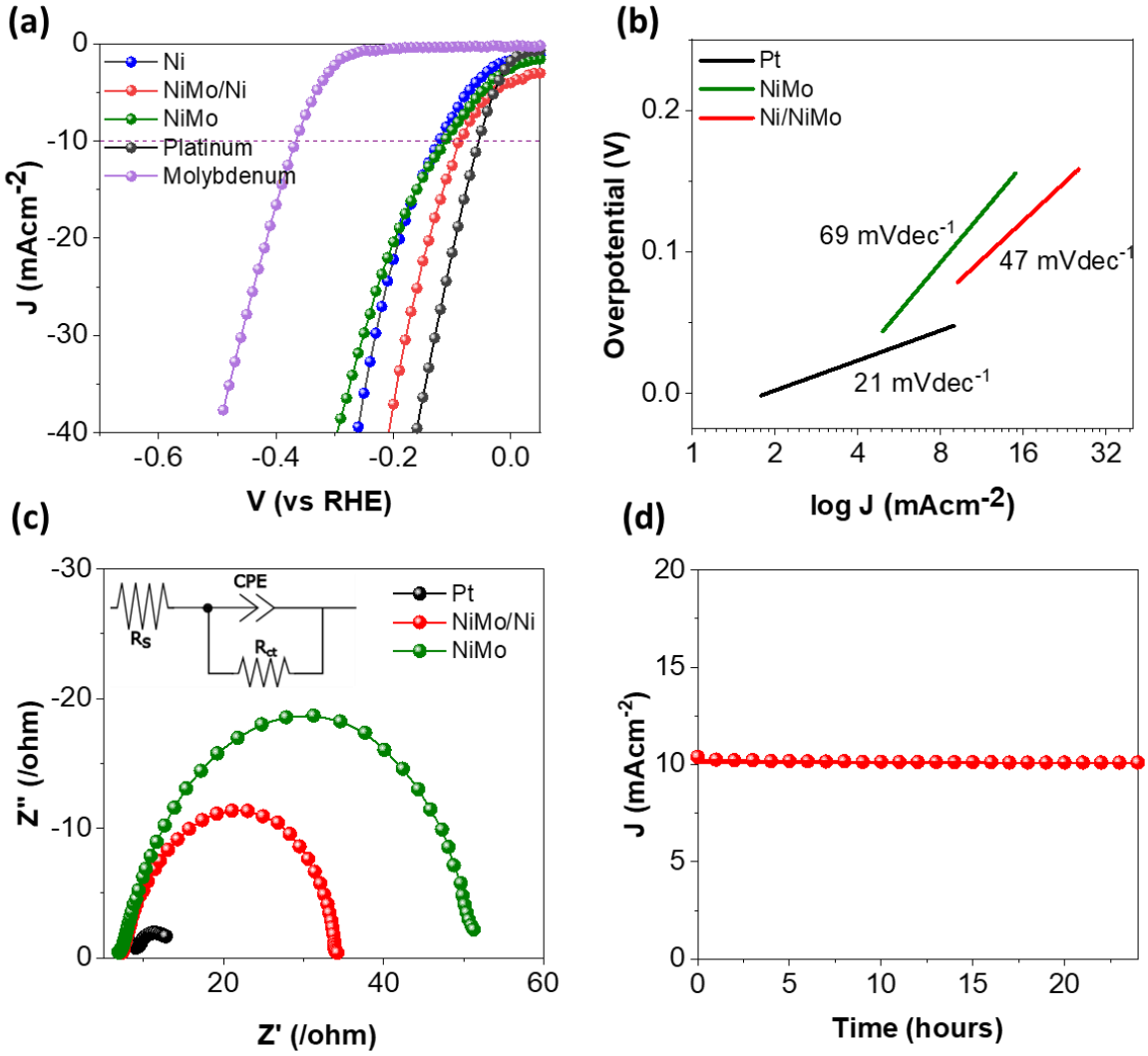

Figure 4.3: (a) Linear sweep voltammetry (LSV) curves of NiMo, NiMo/Ni, Pt, Ni and Mo for HER on FTO substrate. (b) tafel slopes of of NiMo/Ni, NiMo and Pt for HER on FTO substrate calculated from LSV curves (c) Electrochemical impedance spectroscopy (EIS), Nyquist plots of NiMo/Ni, NiMo and Pt for HER on FTO substrate. (b) Current density vs time (J-t) measurements of NiMo/Ni/FTO at 10 $mAcm^{-2}$. All the measurements are performed in three electrode configuration in 1 M KOH solution.

The HER overpotential of the catalysts is compared at a current density of 10 $mAcm^{-2}$. The NiMo with optimum alloy ratio shows superior HER activity with overpotentials as low as 113 mV at a current density of 10 $mAcm^{-2}$, lower than Ni and Mo with overpotentials of 123 mV and 366 mV respectively. Depositing a Ni interlayer (NiMo/Ni) further improves the catalytic performance, reducing the overpotential to 89 mV at 10 $mAcm^{-2}$ on a planer FTO substrate. Notably, this performance is comparable to that of high-cost Pt. NiMo/Ni achieved a low Tafel slope of 47 $mVdec^{-1}$, showing fast reaction kinetics (figure 4.3(b)). As discussed in the last section, improved performance for NiMo/Ni is attributed to formation of a non-conformal nanorod morphology that improves charge transfer to catalytic site. These results are in agreement with reports that alloying 3-D transition metals improves the HER electrocatalytic activity above that of the individual activities of the pure constituent metals [144]. This enhancement can be explained by the Brewer-Engel valence band theory: mixing of Ni (with half-filled d-bands) and Mo (with more fully filled d-bands) improves the M-H bond strength values compared to individual metals, and hence alters the HER activity, and reduces the overpotentials of the alloy compared to the individual metal catalysts [144, 154].

Figure 4.3 (c) shows the Nyquist plots measured using EIS. The addition of the Ni interlayer substantially reduces the charge transfer resistance (R_{ct} as shown in inset in figure 4.3 (c)) of the NiMo/Ni bilayer catalyst (22.33 Ωcm^2) compared to a single layer of NiMo (46.42 Ωcm^2), suggesting that the enhanced performance can be attributed to improved charge transfer to the catalytic sites. Chronoamperometry measurement demonstrate stable performance of NiMo/Ni catalyst on FTO at 10 $mAcm^{-2}$ for 24 hours of continuous operation (figure 4.3. (d)) and a Faradic efficiency of around 99% (table S 4.2).

4.5. Charge selective passivation layer for silicon photocathodes

In order to reduce the recombination losses at the Si/catalyst interface we introduce a SiO_X/n^+ polycrystalline Si (SiO_X/n^+poly-Si) charge selective passivation layer. Such passivation layers effectively reduce charge recombination due to c-Si defect states, and simultaneously act as selective contacts, allowing the flow of only one type of charge carrier.

4.5.1. Charge selective passivation layer fabrication and working mechanism

The charge selective passivation layers are adapted from the work of Yan and colleagues at the ANU [155]. Apart from the deposition of the passivation layer, the Si photocathode fabrication method is similar to that described in Chapter 3 section 3.3.1. A SiO_X/n^+poly-Si charge selective passivation layer is deposited after the diffusion of the front emitter region, and before the deposition of the front passivation/anti-reflection coating. A diffusion mask is deposited on the front surface to protect the boron diffusion of the emitter. An ultrathin SiO_X (1-2 nm) layer is then grown by dipping the wafers in boiling nitric acid at 85 ℃, followed by a-Si deposition at the rear using plasma enhanced chemical vapour deposition (PECVD). The a-Si layer is then subjected to heavy phosphorus doping, by thermal diffusion of $PoCl_4$ (phosphorus oxychloride) at 820 ℃, resulting in the formation of n^+doped polycrystalline Si film. A SiN_X layer is then deposited using PECVD followed by annealing in forming gas at 425 ℃ for 25 minutes for hydrogenation. The SiN_x layer and the front masking layer are then removed by HF fuming. For the samples without any passivation layer, a rear n^+ phosphorus doped layer is formed by thermal diffusion of $PoCl_4$ (phosphorus oxychloride). HF fuming is used to remove the front masking layer in these samples too.

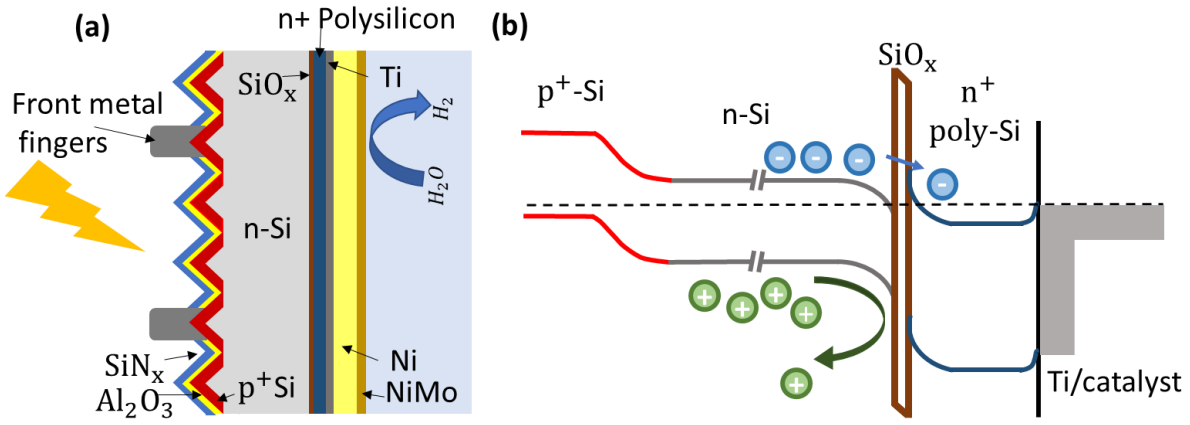

Figure 4.4: (a) Schematic and (b) band alignment of Si photocathode with SiO_X/ n^+polycrystalline Si passivation and NiMo/Ni Earth abundant catalyst

Figure 4.4 (a) shows the schematic of the Si photocathode with a charge selective passivation layer and NiMo/Ni catalyst at the rear. A thin Ti layer is introduced to improve the catalyst adhesion. The charge transfer mechanism across the charge selective passivation layer can be explained with reference to the band alignment as illustrated in figure 4.4 (b). The chemically grown ultrathin SiO_X layer provides effective chemical passivation at the c-Si/oxide interface, while still enabling charge transfer from c-Si to poly-Si through tunnelling across the ultrathin barrier. The highly doped poly-Si region results in significant band bending at the SiO_X interface which aids electron transfer while blocking hole transfer [135]. The high doping density of the order of $10^{19}cm^{-3}$ also allows the formation of an ohmic contact at the n^+poly-Si/Ti junction, ensuring good charge transfer across the interface.

4.5.2. Silicon photocathode performance analysis

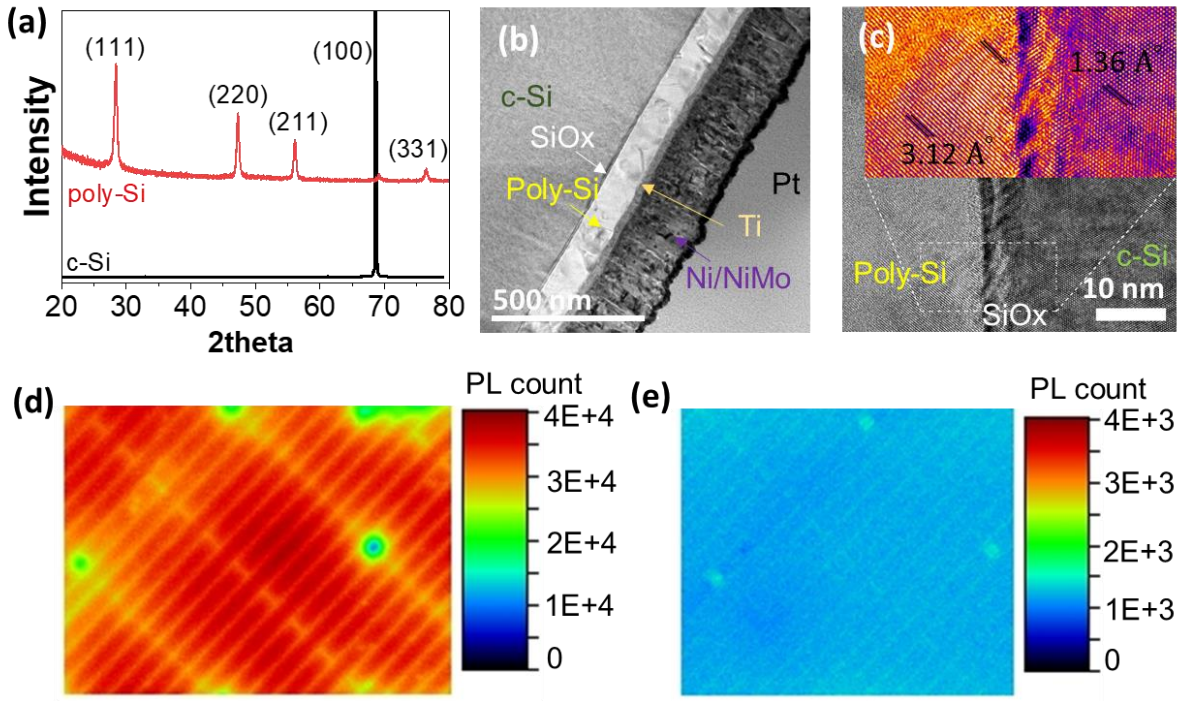

Figure 4.5: (a) X-ray diffraction (XRD) spectra of polycrystalline Si (red) and c-Si (black). (b) High resolution transmission electron microscopy (HR-TEM) image of NiMo/Ni earth abundant catalyst integrated Si photocathode with SiO_x/ n^+poly-Si passivation layer and (c) c-Si/ SiO_X/n^+poly-Si interface. Photoluminescence (PL) imaging of Si photocathode (d) with and (e) without / SiO_X/n^+ poly-Si passivation.

In this section the morphology and passivation quality of the polySi layer is analysed. The polycrystalline structure of the film is confirmed by XRD analysis, as shown in **Figure 4.5** (a). The c-Si (black) XRD spectrum shows a dominant peak appearing at 2θ value of 69.2 corresponding to (100) plane, while the n^+poly-Si (red) spectrum shows clear peaks appearing at 2θ values of 28.5, 47.3, 56.1, 69.2 and 76.45 corresponding to (111), (220), (211), (100) and

(331) planes, indicating that the film is polycrystalline. The HR-TEM image of the Si photocathode (figure 4.5 (b)) clearly identifies All the separate layers and shows uniform deposition and thickness thought the region. Figure 4.5 (c) shows a zoomed in HR-TEM image of the c-Si/SiO_x/n^+poly-Si interface. The coloured inset image is a further magnified image of the selected area with false colouring for better contrast. The n^+poly-Si film has lattice fringes with interplanar spacing of 3.12 Å corresponding to the dominating (111) plane of n^+ poly-Si, in agreement with the XRD measurements. The crystalline-Si wafer shows the (100) planes of the single crystalline phase.

The quality of the interface passivation for the Si photocathodes with and without the SiO_X/ n^+poly-Si charge selective passivation layer is compared using photoluminescence (PL) imaging, which is a standard measurement technique used in the solar cell community to compare the carrier lifetimes of samples and finished cells. In this technique, the strength of the measured PL signal (in counts) is proportional to the carrier lifetime and hence passivation quality. Figure 4.5 (d) and (e) show the PL images of the Si photocathode with (d) and without (e) SiO_X/ n^+poly-Si layer. The large features in the passivated film (figure 4.5 (d)) are attributed to uneven HF fuming during removal of the rear SiN_X masking layer. The passivated photocathodes have a PL count which is more than an order of magnitude higher than the Si photocathode without any passivation. The higher PL count of the passivated Si photocathode directly translates to higher effective carrier lifetime and better passivation quality at the SiO_X/n^+poly-Si/Ti interface compared to n^+c-Si/Ti interface.

To further investigate the improvement in the performance of Si photocathode upon passivation, PEC measurements are performed. Si photocathode integrated with NiMo/Ni

catalysts, with and without SiO_X/n^+poly-Si charge selective passivation layer are measured in a three-electrode configuration in 1 M KOH solution under AM1.5G illumination. **Figure 4.6** (a) shows the LSV response of the Si photocathodes with (red) and without (black) passivation. The results suggest that even with a high activity HER catalyst, recombination losses at the interface limit the conversion efficiency of the Si photocathode without passivation, demonstrating a low photocurrent density of 31.1 $mAcm^{-2}$ and onset potential of 528 mV . However, with a SiO_X/n^+ poly-Si charge selective passivation layer, the current density improves markedly to 37.8 $mAcm^{-2}$, as does the onset potential to 570 mV.

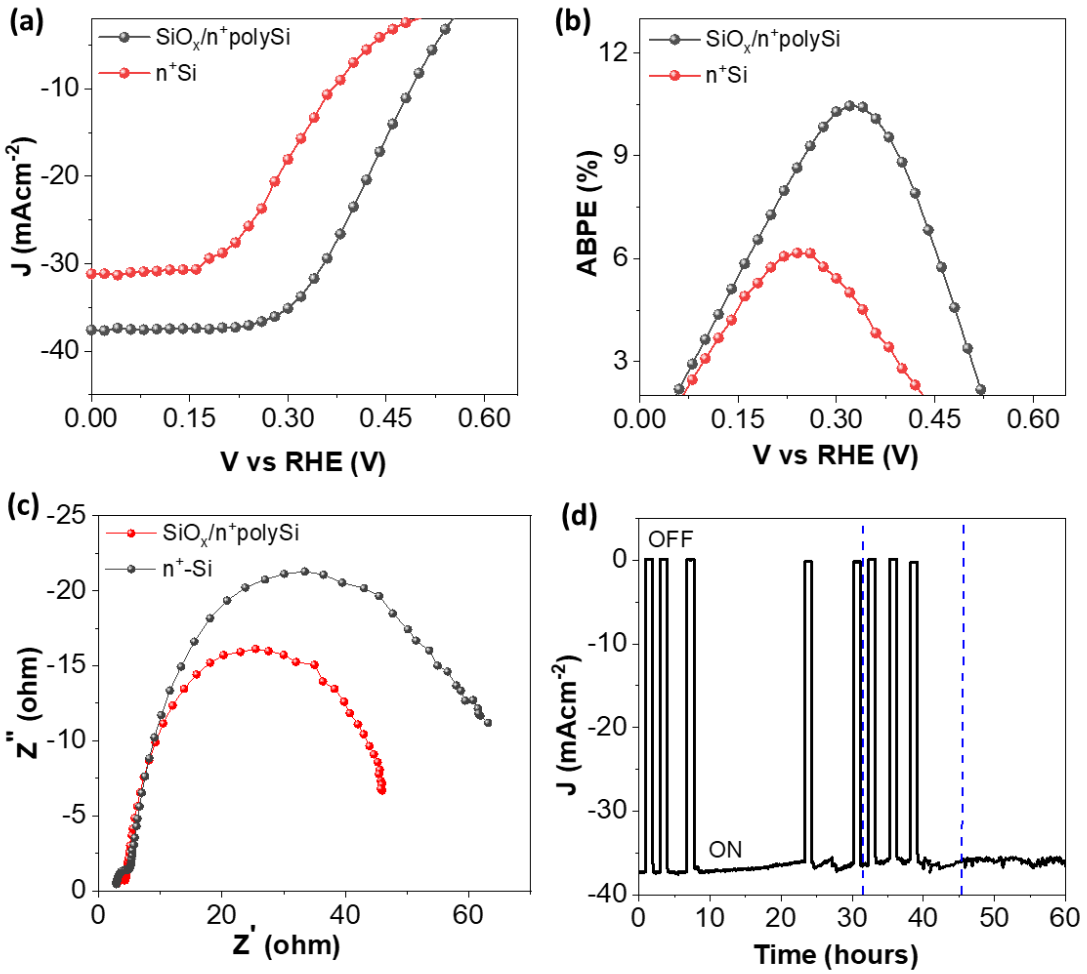

Figure 4.6: Photoelectrochemical performance of Si photocathodes with (red) and without (black) charge selective passivation layer. (a) Three electrode linear sweep voltammetry (LSV), (b) applied bias to photon conversion efficiency (ABPE) and, (c) photoelectrochemical impedance spectroscopy (P-EIS). All measurements were performed in three electrode configuration in 1 M KOH. (d) Current density vs time (J-t) stability measurements of Si photocathode with SiO_x/ n^+polycrystalline Si passivation layer in 1 M KOH. Blue dashed line represents electrolyte change and reference electrolyte clean.

Figure 4.6. (b) shows the resultant ABPE for Si photocathode with (red) and without (black) any passivation calculated from LSV curves. The Si photocathode without any passivation shows a low ABPE of 6.2%, while addition of the SiO_X/n^+p- Si layer improves the ABPE to 10.5%. This translates to a relative improvement of 70% in ABPE upon passivation.

Next, we perform photoelectrochemical impedance spectroscopy (P-EIS) measurements to compare charge transfer resistance in photocathodes with and without charge selective passivation layers. Figure 4.6 (c) shows the Nyquist impedance plots for Si photocathodes with (red) and without (black) SiO_X/n^+ poly-Si passivation layers. The P-EIS response for both the photocathodes show two distinguishable semi-circles. The second semicircle size reduces considerably upon SiO_X/n^+ poly-Si passivation indicating the decrease in the charge recombination at the interface, enhanced charge lifetime, and better charge transfer, in agreement with the PL image analysis in figure 4.5 (d and e) [122, 128].

Current density vs time (J-t) measurements are performed in a three-electrode configuration at 0 V vs RHE, in 1 M KOH. The passivated Si photocathode shows stable performance over 60

hours under 1 sun (AM1.5G) illumination, as shown in figure 4.6 (d). The light is turned on and off during the measurement as labelled in the plot. The fluctuations in the operating current density when the photocathode is under illumination are due to bubbles formed on the surface, which blocks the active catalyst area. The electrolyte was changed, and reference electrode was cleaned twice during the measurements, at the times indicated by dashed blue lines in the figure.

4.6. Photoelectrochemical system based on all low-cost materials for direct solar hydrogen generation

To achieve unassisted water splitting with a PEC system based on all low-cost materials, we incorporate a perovskite top cell with our Si photocathode in a 2-T tandem configuration, and a NiFe OER anode as shown in **figure 4.7** (a). A similar system has been demonstrated previously with 17% STH efficiency based on noble metal catalysts [64]. The NiFe OER catalysts is based on the work of Liu et. al. and has a nano-cone like structure [156]. The perovskite cells were fabricated by The Doung, at The Australian National University. NiFe OER anode synthesis and characterisation was performed by Peng Liu, at Tsinghua University. The design of the solar hydrogen generation system, as well as the integration, characerisation and analysis was performed by the author.

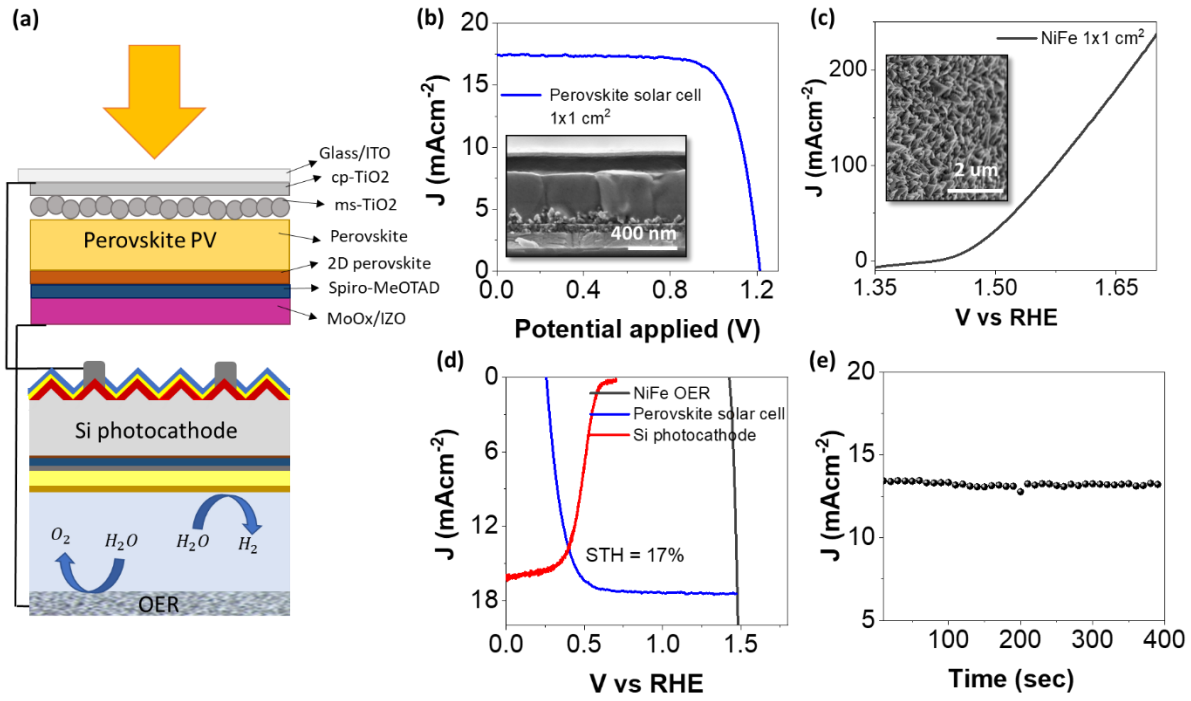

Figure 4.7: (a) Schematic of a PEC system in PV-PEC configuration based on low-cost materials, incorporating a large bandgap semi-transparent perovskite cell connected in two-terminal tandem configuration to NiMo HER catalyst integrated silicon photocathode and a NiFe anode. (b) J-V curve of 1x1 cm^2 high bandgap perovskite solar cell. Inset shows the cross-sectional SEM image of different layers in perovskite cell (c) Three electrode LSV curves of 1x1 cm^2 NiFe nanocone arrays OER in 1 M KOH. Inset shows the cross-sectional SEM image of the NiFe nano-cone arrays morphology. (d) Overlay of J–V curves of area matched (1x1 cm^2) high bandgap perovskite cell (red), the Si photocathode behind the perovskite cell (blue), and the NiFe nano-cones anode (grey). (e) Photocurrent response of the integrated system under AM1.5G solar illumination in 1 M KOH.

A semitransparent perovskite PV cell with bandgap 1.72 eV is used as a top cell absorber, which is close to the ideal top-cell bandgap for current matching with bottom Si cell in order

to obtain the maximum STH efficiency, as shown in Chapter 1 and 5 and published in [22]. One by one cm^2 perovskite solar cells are fabricated were fabricated by The Doung, at The Australian National University, using a 3D perovskite absorber consisting of the quadruple-cation mix-halide perovskite. It has been previously demonstrated that coating the 3-D perovskite absorber with 2-D perovskite passivates the surface defects and enhances the power conversion efficiency [61]. Details of the perovskite cell fabrication are discussed in Appendix C. Figure 4.8 (b) shows the J-V curve of the perovskite solar cell (blue). The cell achieves a PCE of 15.9%, with a J_{sc} of 17.4 $mAcm^{-2}$, FF of 75.5%, and high V_{oc} of 1.21 V with negligible hysteresis.

The NiFe nanocone arrays OER catalyst was fabricated by Peng Liu, at Tsinghua University on Ni foam by one step electrodeposition. The inset of figure 4.7 (c) shows an SEM image of the OER electrode with nano-cones array morphology. The nanocone arrays exhibit high curvature tips, which improves the local electric field, results in accumulation of hydroxide ions (OH^-) at the active sites, and promotes OER activity. The LSV response of the 1 x 1 cm^2 NiFe OER electrode in a three-electrode configuration presents a low overpotential of 233 mV at 10 $mAcm^{-2}$ (figure 4.7 (c)).

The representative performance of the PEC system is shown in figure 4.7 (d). The J-V curves of the perovskite top cell, Si photocathode (behind the perovskite, with respect to the 1-sun illumination) and NiFe/NF OER anode are plotted together to determine the operating current density of the overall system. The blue curve represents the J-V performance of the perovskite solar cell, and the grey curve represents the J-V response of the NiFe/NF OER electrode, identical to figure 4.7 (b,c). The Si photocathode behind the high bandgap perovskite PV

exhibits a photocurrent of 16.4 $mAcm^{-2}$ at 0 V vs RHE (red). The integrated system achieves an operating photocurrent density of 13.8 $mAcm^{-2}$, which corresponds to a high STH efficiency of 17 %, for an area matched system. The water splitting performance of the PEC system is evaluated in two-electrode configuration (figure 4.7 (e)). The integrated system shows a direct water splitting current of ~13.8 $mAcm^{-2}$, matching closely with that determined from the J-V curves of individual components.

Combining the high-performance Si photocathode together with high bandgap perovskite top cell, and optimum current matching between two absorbers in the tandem configuration results in a STH efficiency of 17%. These results demonstrate that PEC systems based on all low-cost materials can compete with recently demonstrated PEC systems based on perovskite/Si tandems, employing high-cost noble metal catalysts [64], and are comparable to systems based on III-V semiconductors [42].

4.7. Conclusion

In this work we develop a high efficiency PEC system in PV-PEC configuration based on low-cost materials, employing charge selective passivating contacts in Si photocathodes, and incorporating earth abundant catalyst materials for DSHG. To achieve this, NiMo hydrogen evolution reaction catalysts are developed using magnetron co-sputtering. We show that using a Ni interlayer allows formation of non-conformal nanorod morphology on planer substrate, supporting effective transport of reactants to the catalyst sites and improving performance. Si photocathodes with state-of-the-art charge selective passivation layer are developed, improving the photocathode performance by roughly 70%, and highlighting the performance limitations

due to recombination losses at the Si/catalyst interface. Finally, we demonstrate unassisted water splitting in a PEC system based on all low-cost materials, by combining our Si photocathode with a high bandgap perovskite PV top cell and an NiFe OER anode to achieve a STH efficiency of 17%. As well as demonstrating very high efficiencies, our system uses industrially compatible processes for the fabrication of both the catalysts and Si photocathode, which could enable an efficient transition to large-scale production in the near future by leveraging existing PV manufacturing infrastructure.

4.8. Supplementary Information

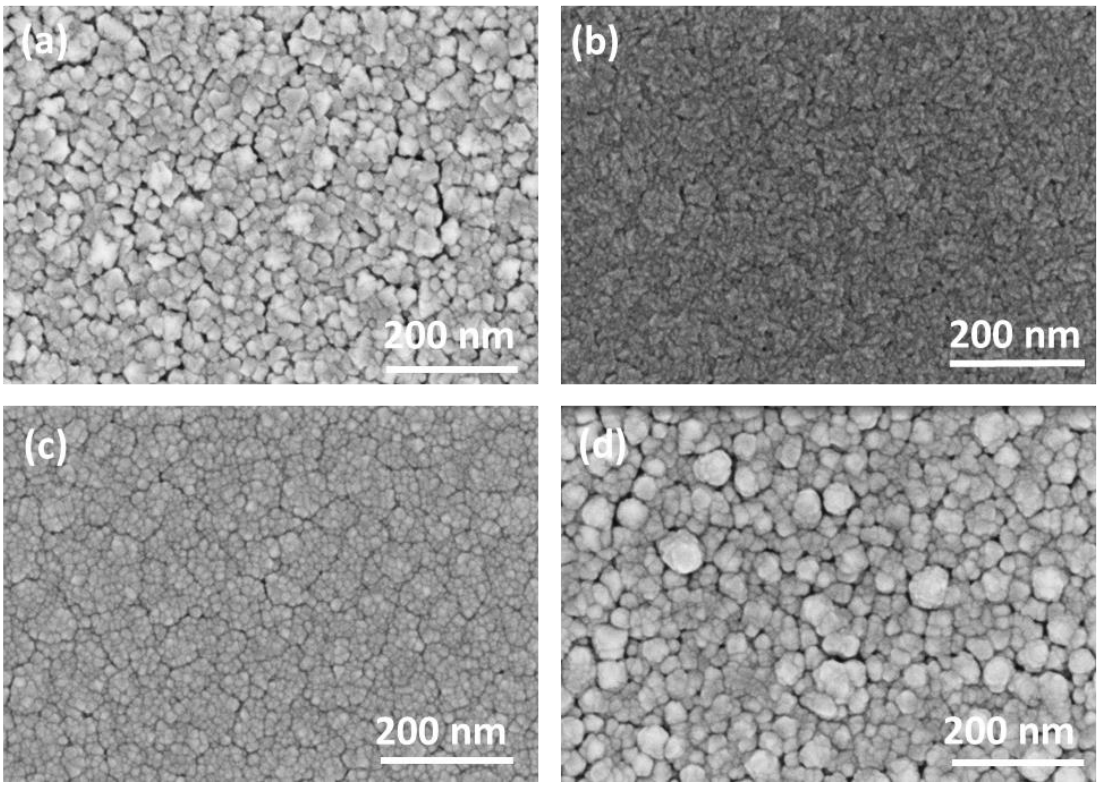

Figure S 4.1: SEM image of (a) Ni (b) Mo (c) NiMo and (d) NiMo/Ni films on SiOx/Si substrate

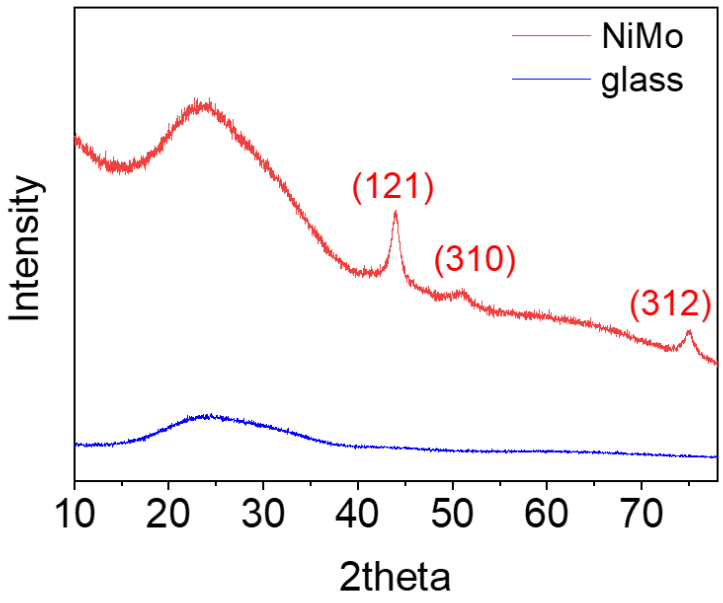

Figure S 4.2: X-ray diffraction of NiMo catalyst on glass substrate.

Table S 4.1: Interplanar spacing (d-spacing) calculations for hkl planes from the XRD.

(hkl)	2 theta	Theta	d-spacing
121	43.5	21.75	2.07
310	51.2	25.6	1.79
312	74.96	37.48	1.26

Table S 4.2: Flame ionisation detection (FID)-GC measurements for faradic efficiency (FE) calculation of NiMo/Ni HER catalyst

Current density	**H_2peak area**	**FE H_2 (NiMo/Ni)**
-10	3384	0.97
-10	3460	0.99
-10	3391	0.97
-20	9378	1.02
-20	9176	1.00
-20	9036	0.98
		0.988 = 98.8%

Pt (avg value) of H2 area for Pt
@ -10 mA – 3469
@ -20 mA - 9140

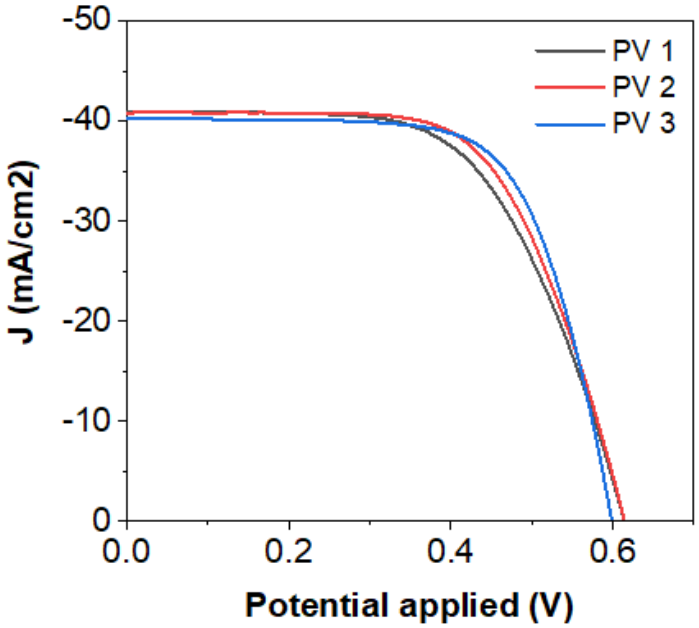

Figure S 4.3: Solid state J-V characteristics of Si photocathode with selective contact passivation layer and 400 nm e-beam deposited Ti rear

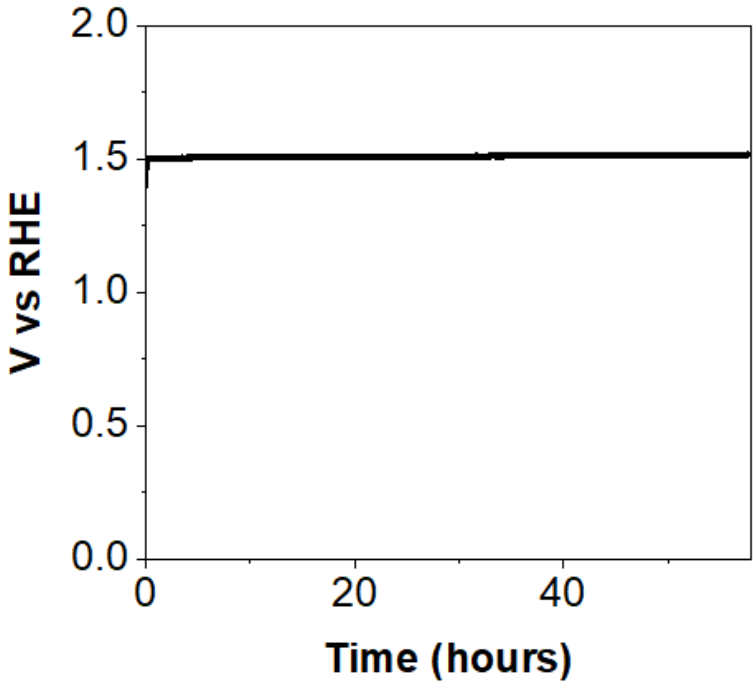

Figure S 4.4: Chronopotentiometry measurements of NiFe nanocone array OER anode in three electrode configuration, 1 M KOH

Table S 4.3: Unassisted solar water splitting systems with at-least one semiconductor-electrolyte junction and low-cost PV (text in red are all low-cost materials-based PEC systems)

	PV/Photoelectrode	Catalyst (HER/OER)	STH %	Year	Ref
1	Perovskite PV/Si photocathode	Pt IrRu (DSA)	17.5	2020	[64]
2	3 IBC Si (series)	Pt Ni	15.6	2020	[109]
3	Si PV/Si photocathode/Si photoanode	NiMo Ni	9.8	2019	[157]
4	a-Si:H/µc-Si:H/c-Si	Pt RuO2	9.5	2016	[158]
5	a-Si:H/a-Si:H/uC-Si:H	Pt ZnO:Co	9.1	2016	[159]
6	2 c-Si PV/Fe2O3/BiVO4 photoanode	Pt NiOOH/ FeOOH	7.7	2016	[160]
7	DSSC PV/WO3/BiVO4 photoanode	Pt NiOOH /FeOOH	7.1	2016	[40]
8	2Perovskite photoelectrode (series)	CoP Co3O4	6.7	2020	[161]
9	Perovskite PV/ CuInGa photocathode	IrRu-anode	6.3	2015	[162]
10	2 c-Si PV/BiVO4/CoOx photoanode	CoP Ni	5.3	2018	[163]
11	DSSC/BiVo4/WO3 photoanode	Pt cathode	5.7	2015	[39]
12	Si photocathode/BiVO4 photoanode	Pt FeOOH/NiOOH	3.7	2021	[127]
13	**Perovskite PV/Si photocathode**	**NiMo/Ni NiFe**	**16.5**	**2021**	**Current Work**

Chapter 5

Quantifying and Comparing Fundamental Loss Mechanisms to enable Solar to Hydrogen Conversion Efficiencies above 20% for Perovskite-Silicon Tandem Absorbers

5.1. Introduction

In this Chapter we introduce a new theoretical approach to quantify the losses in PEC system for DSHG and assess the potential of loss mitigation techniques to improve the STH efficiency. This Chapter is adapted from the paper [22] , published by author. In section 5.2 we give a brief overview of different approaches discussed in literature to improve the STH efficiency. We further demonstrate the need for a quantitative analysis of different loss mechanisms and give a brief overview of the Chapter. In section 5.3 we develop a theoretical model to quantify different losses in PEC systems for DSHG. Our analysis shows that the two largest losses in an ideal solar hydrogen generation system are current and voltage mismatch due to sub-optimal system configurations, and energy lost as heat in the photovoltaic component. In section 5.4 we analyse the effect of operating temperature on the performance of PV and EC components, and the performance of thermally integrated solar hydrogen generation systems at varying PV cell temperatures. We then develop a realistic temperature dependent model of PEC system for DSHG in section 5.5, taking into account loss factors to account for non-ideal diode characteristics in the photovoltaic components, and material-dependent reaction overpotential losses in the catalytic components. In section 5.6 we evaluate the relative potential of two

techniques to mitigate the key system losses: decoupling the PV component to remove current and voltage matching requirements; and thermal integration to use the heat losses in the PV cell to increase the electrolyte temperature and improve the reaction dynamics for water-splitting. We show that optimal system configuration strategies provide more than three times the increase in STH efficiency of thermal integration at high operating temperatures. Combining both techniques result in predicted STH efficiencies approaching 20% for low-cost perovskite-Si tandem-based systems with earth abundant catalysts at realistic working temperatures.

5.2. The need for quantitative analysis of losses in photoelectrochemical systems for direct solar hydrogen generation

Understanding theoretical STH efficiencies is important to identify performance limitations and to conceptualise practical device designs for low-cost, high-efficiency solar hydrogen generation. Several authors have developed frameworks to identify optimum bandgap combinations for tandem systems [19, 23, 85, 86]. Other works have demonstrated the importance of considering the effect of different electrical and optical configurations in tandem based systems [32, 87-89]. In particular, it has previously been shown that significant performance enhancements can be achieved by decoupling the PV components from the electrochemical electrodes and incorporating a power management unit, allowing the system to be operated at an optimum current and voltage to maximise the STH [21]. The operating temperature of the system has also been shown to be an important parameter [90, 91]. Tembhurne et. al. have demonstrated an integrated photoelectrochemical system design to take advantage of the higher PV operating temperatures and use thermal management as an effective

tool to increase the device efficiency [164, 165]. In general, these studies have tended to focus on a single aspect of the system design for example, choice of material, operating parameters, or device configuration.

As discussed in Chapter 2 and restated here, despite the importance of the studies discussed above, there is still a lack of understanding of the relative importance of different loss mechanisms for solar hydrogen generation systems. Loss mitigation techniques can be employed at different levels in the system to improve the STH efficiency, but generally add complexity and cost to the system. It is necessary to ensure that the most effective loss mitigation techniques are employed, however there have been no studies that systematically compare their potential to increase performance.

In this Chapter, we quantify and compare the relative contribution of different losses in PEC systems for DSHG and assess the potential of different loss mitigation techniques to improve the STH efficiency. We focus on Si-based tandem systems considering the commercial dominance of silicon for large-scale PV applications [46].

5.3. Fundamental losses in direct solar hydrogen generation system

We start by calculating the limiting efficiencies and fundamental loss processes in PEC system for DSHG. As discussed in Chapter 2, PEC system can be divided into two main components defined by their role in the hydrogen generation process: the PV component responsible for the conversion of light to electrical energy; and the EC component which mediates the conversion of electrical energy to chemical energy.

The PV component in a water-splitting device absorbs the incoming solar irradiation and generates photocurrent and photovoltage. The charge generation and separation phenomenon are the same irrespective of its design as a solar cell or a photoelectrode. A detailed balance approach is used to model the ideal efficiency of the individual PV components as well as the different loss processes occurring in the system. Details of the model are discussed in section 2.3, Chapter 2.

To understand the processes limiting the PV cell efficiency it is instructive to quantify these fundamental loss mechanisms separately [166] [167]. Firstly, energy is emitted from the cell due to radiative recombination. This results in the recombination current, $J_{rad,}$ as defined in equation 2.18 in Chapter 2, and can be converted into an energy loss,

$$L_{rad} = \frac{J_{rad}}{q} E_g \tag{5.1}$$

where $E_g$is the bandgap and q is the elementary charge. Secondly, not all the solar radiation can be absorbed, and photons with energy lower than the PV cell bandgap are lost in the form of below bandgap losses,

$$L_{E_\gamma < E_g} = \int_0^{E_g} E \cdot \phi(E, T_S, \Omega_{abs}) dE \tag{5.2}$$

where, $\phi(E)$ the incoming photon flux from a black body defined in equation (2.15), Chapter 2 and restated below

$$\phi(E,T,\Omega) = \frac{2\Omega}{c^2h^3}\frac{E^2}{exp\left(\frac{E}{kT}\right)-1}$$

The incoming photon flux is a function of photon energy, E, solid angle, Ω, and temperature, T. Here $c = 3 \times 10^8\ ms^{-1}$, is the speed of light, $h = 6.63 \times 10^{-34} Js$, is the Planck's constant and $k = 1.38 \times 10^{-23} JK^{-1}$, is the Boltzmann constant. To calculate the incident solar flux we take, $\Omega_{abs} = \Omega_{solar} = 6 \times 10^{-5}$ is the absorption angle from sun to the PV cell and $T_s = 6000K$ is the temperature of Sun.

Thirdly, the PV cell generates entropy in the process of converting optical radiation into electrical/chemical work [167, 168]. The energy lost to the environment due to the creation of entropy is known as Carnot loss[166],

$$L_C = E_g\left(\frac{T_{PV}}{T_S}\right)J_{op} \tag{5.3}$$

where, J_{op} is the operating current density and $T_{PV} = 300K$ is the PV cell temperature. Fourthly, mismatch in the angle of absorption and emission causes the expansion of photon modes and entropy generation. This reduces the free energy that can be extracted per carrier in the form of Boltzmann loss [17],

$$L_B = kT_{PV} ln\left(\frac{\Omega_{emit}}{\Omega_{abs}}\right)J_{op} \tag{5.4}$$

where, $\Omega_{emit} = \pi$, is the solid angle of emission.

Finally, any energy above the bandgap energy is lost as heat as the electron relaxes to the conduction band edge. This is known as thermalisation loss [169],

$$L_{Th} = \int_{E_g}^{\infty} E \cdot \phi(E, T_S, \Omega_{abs}) dE \; - \; E_g \int_{E_g}^{\infty} \phi(E, T_S, \Omega_{abs}) dE \tag{5.5}$$

The EC component of the water-splitting system consists of the series-connected HER and OER electrocatalysts, separated by an ion-conducting electrolyte. For a standalone water-splitting system, the voltage required to overcome the reaction potential and additional losses is given by equation 2.5 in Chapter 2 and restated below [79]:

$$V_{IN}(J,T) \geq E_{STH}(T) + V_{OER}(J,T) + V_{HER}(J,T) + V_e\,(J,T) \tag{5.6}$$

where E_{STH} is the electrochemical reaction potential which defines the minimum potential required to drive the water-splitting reaction (at a specific temperature, T, and pressure condition) and is given by equation (2.6) in Chapter 2; $V_{OER}(J,T)$ and $V_{HER}(J,T)$ are the temperature-dependent activation overpotential losses during the OER and HER respectively; and $V_e(J,T)$ is the resistive voltage loss due to charge transport.

As discussed in Chapter 2, in a PV-tandem based PEC system, the potential requirement to drive the electrochemical water-splitting reaction can be satisfied by using two PV cells with complementary bandgaps connected in a variety of configurations [21, 88]. As demonstrated by [21] systems can be fully *coupled*, with two PV cells connected in series with each other (2-T tandem cell configuration) and with the EC components through wires or an interface, such that the same operating current (J_{op}) is flowing through all the components (**Figure 5.1** (b))

[21]. Conversely, in a *fully decoupled* configuration, the two PV components are separately connected independently to the power management unit (PMU) (known as a 4-T configuration) (Figure 5.1 (d)) [21]. The PV cells can then be operated at their respective MPP while the PMU optimises the current and voltage provided to the EC components [21]. Here we recognise that it is also possible to partially *decouple* the EC and PV components by connecting a 2-T tandem solar cell to a PMU, which in turn is wired to the EC components (Figure 5.1 (c)). The 2-T tandem cell can then be operated at the matched current (J_{PV}) that maximises the output power of the solar cell, while the PMU provides the optimum operating current at the voltage required to drive the water-splitting reaction. The resultant voltage for different system configurations can be summarized as

$$\text{Coupled: } V_{IN}\left(J_{op}\right) = V_{PV,1}\left(J_{op}\right) + V_{PV,2}(J_{op}) \tag{5.7}$$

$$\text{2-T PV decoupled: } V_{IN}\left(J_{op}\right) = \frac{(V_{PV1}(J_{PV}) + V_{PV2}(J_{PV}))\, J_{PV}}{J_{op}} \tag{5.8}$$

$$\text{4-T PV decoupled system: } V_{IN}\left(J_{op}\right) = \frac{MPP_1 + MPP_2}{J_{op}} \tag{5.9}$$

where MPP_1 and MPP_2 are maximum power operating points of top and bottom PV cells. It is important to note that monolithic photoelectrochemical systems represented by figure 2.2 (b) in Chapter 2 (also known as 'artificial leaf' systems) are always in the coupled configuration, but any system that could be physically separated by wires can be decoupled.

The STH efficiency is defined by the fixed thermodynamic potential requirements of the water-splitting reaction (E_{STH} = 1.23 V) and is then given as (equation (2.22), Chapter 2 and restated below)

$$\eta_{STH} = \frac{J_{op}\, E_{STH}\, \eta_f}{P_{in}} \tag{5.10}$$

where, η_f is the Faradic efficiency and assumed to be unity.

To understand the cumulative effect of the system configuration and different loss processes and their dependence on the PV cell bandgap, we plot the efficiency and intrinsic losses as a function of top-cell bandgap ($E_g top$), as a fraction of total input solar energy, with a fixed solid angle of absorption and emission. We consider a series-connected solar hydrogen generation system using the standard 2-T PV tandem configuration (coupled system) with variable bandgap top-cell and Si bottom cell.

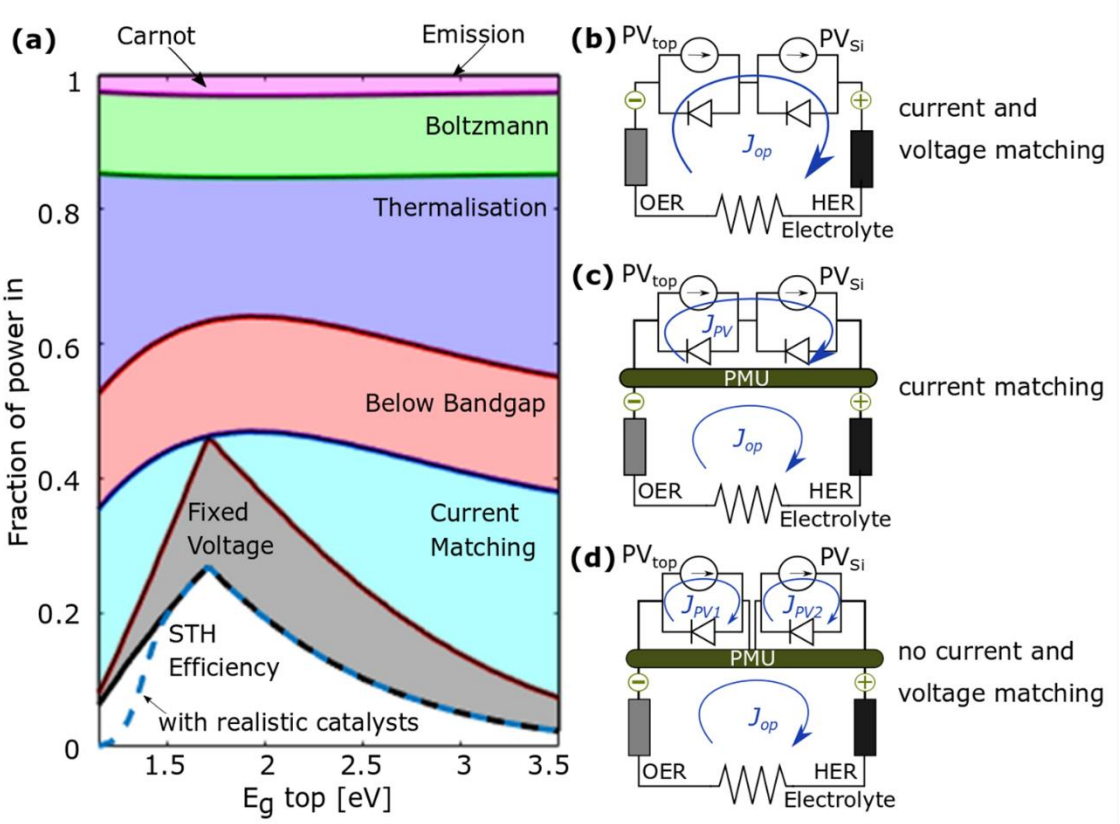

Figure 5.1: (a) Fraction of the input solar energy that is converted to energy in the form of hydrogen, and subsequent energy losses for an ideal solar hydrogen system as a function of top cell bandgap, in series with a Si bottom cell. The black and dashed blue line represent solar to hydrogen conversion efficiencies, with ideal and realistic catalysts, respectively. Equivalent circuit diagrams for (b) coupled, (c) 2-T PV tandem decoupled, and (d) 4-T PV tandem decoupled systems.

Figure 5.1 (a) shows the fraction of input solar energy that is converted to chemical energy in the form of hydrogen (black line, STH efficiency) in an ideal solar hydrogen generator as a function of the top cell bandgap, in series with a Si bottom cell. The different shaded areas of the graph represent different energy loss mechanisms in the system. These losses can be

characterised as reaction losses (due to realistic, high efficiency catalysts), losses due to system integration (fixed voltage and current matching), and intrinsic losses in the PV component (below bandgap, thermalisation, Boltzmann, Carnot, and emission). Figure 5.1 (b-d) show the equivalent circuit diagrams for different system integration (coupled, 2-T PV tandem decoupled, 4-T PV tandem decoupled).

The maximum STH efficiency for a coupled system with realistic catalysts is 27% (blue, dashed line) and occurs at a bandgap combination generating just enough photovoltage to overcome the reaction potential requirement ($E_g top = 1.73\, eV$). Any additional voltage supplied with a further increase in the top cell bandgap does not contribute towards the chemical reaction and will lead to energy loss and reduction in the efficiency [21]. Reaction losses are due to overpotential losses in the catalysts. If we neglect these losses and assume no overpotential (i.e.,$V_{OER/HER} = 0$, black line), the maximum STH efficiency is still limited to 27%, but the efficiency increases at lower bandgaps. This is because at larger bandgaps the system is not limited by voltage. Reducing the potential requirements by ignoring the overpotential losses does not improve the efficiency as the cell is already working at the maximum power point. However, at smaller bandgaps the system is limited by voltage, so ignoring overpotential losses allows the cell to work at lower voltages, closer to the maximum power point, increasing the current, and hence the efficiency slightly [21, 23]. Figure 5.1 (a) shows total losses of up to 73% at the maximum STH efficiency for a coupled system, represented by the equivalent circuit in figure 5.1 (b).

Introducing a PMU between the 2-T tandem PV and the EC component is equivalent to removing the voltage matching requirement, represented by the equivalent circuit in figure 5.1

(c). Assuming no overpotential losses, the STH efficiency is then equal to the PCE for a 2-T PV cell, giving a maximum STH efficiency of 46% at $E_g top = 1.73eV$ (brown line). PV cells in 2-T configuration require precise current matching of the top and bottom cells for maximum output, restricting the bandgap combination choices[170, 171].

Fully decoupling the system by moving to a 4-T PV tandem removes these current matching requirements, represented by the equivalent circuit in figure 5.1 (d). For an ideal catalyst system with no overpotential losses, the STH efficiency is then equal to the PCE of corresponding 4-T PV cell and has less stringent requirements for bandgap combinations to achieve high efficiencies. In total, 19% of the total available solar energy is lost due to current and voltage matching restriction losses for optimum bandgap combinations for 2-T coupled system.

The remaining losses are due to fundamental process in the PV components as discussed above. These losses can be further grouped as the energy that leaves the system due to radiation or reflection (i.e., emission, Carnot, and Boltzmann losses) and the energy that is converted into heat in the PV component (i.e., thermalisation and below bandgap losses). At maximum STH efficiency, 16% of the input energy is lost externally, while heat losses account for 38% of the total solar irradiation. This fraction is even higher at non-ideal bandgap combinations.

In the simple conceptual model above, we assume that heat dissipates, but in a real system it can cause the semiconductor to heat up, reducing the PV cell performance. However, it is also possible to harness this heat to increase the electrolyte temperature, improving the reaction kinetics and reducing the Gibbs free energy requirement [164]. In the next section, we introduce the concept of thermal integration and quantify the limits of this approach.

5.4. Thermal integration

Thermal integration allows heat losses from the PV component to be used to increase the electrolyte temperature, improving the catalytic reaction efficiency and hence the overall STH efficiency. **Figure 5.2** shows two possible ways to thermally integrate the PV and EC components in different types of solar hydrogen generation systems. Monolithic, coupled PEC systems are immersed directly in the electrolyte and therefore already directly transfer heat to the reactants, as shown in Figure 5.2 (a). To leverage all heat losses in the system – including below bandgap absorption, it is necessary to include a black body absorber, shown in black in Figure 5.2. Coupled or decoupled systems with PV-EC configuration - can also be thermally integrated by flowing the electrolyte through a heat exchanger at the rear of the PV components, as shown in Figure 5.2 (b).

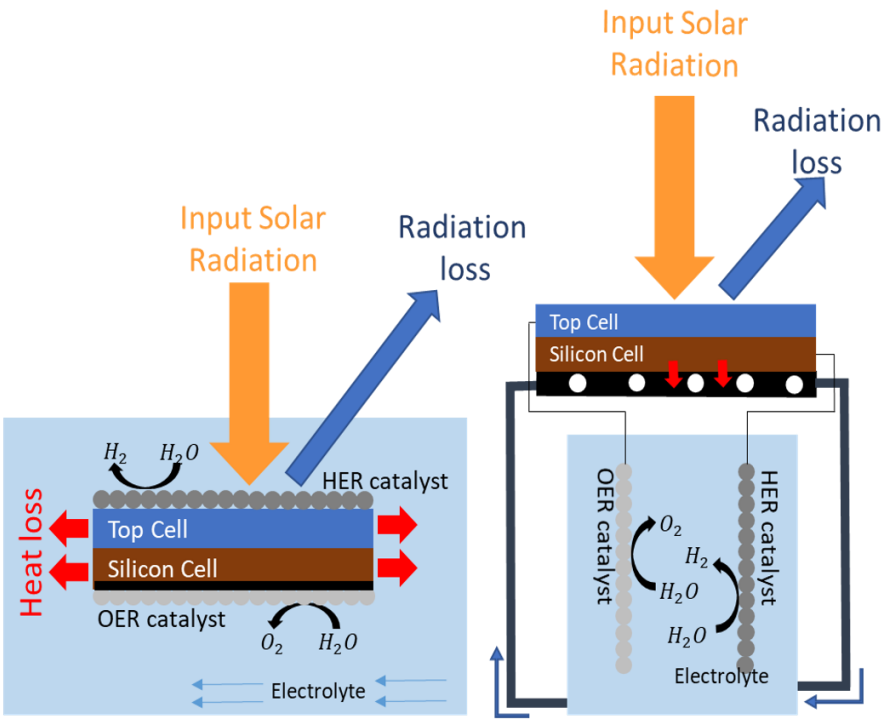

Figure 5.2: Schematics of the thermally integrated system in either (a) a monolithic, coupled configuration, or (b) a physically separated, coupled, or decoupled configuration.

The potential of thermal integration as a loss mitigation technique depends upon the PV cell operating temperature and heat transfer between PV and EC components. In the last section, we predicted the heat losses in the PV component as $L_{th} + L_{E_\gamma < E_g}$, using the detailed balance limit. Here, we use the calculated heat loss to estimate the upper limit for the electrolyte temperature, assuming perfect heat transfer ($\varepsilon_H = 1$). In this case, the maximum electrolyte temperature, T_{EC}, is only limited by the PV component operating temperature, T_{PV}, and there will be a mass flux rate of the electrolyte, j_m, that will allow $T_{EC} = T_{PV}$. **Figure 5.3** shows electrolyte mass flux rate requirements to achieve $T_{EC} = T_{PV}$, calculated using the relation below:

$$T_{EC} = T_{in} + \frac{(L_{th} + L_{E_\gamma < E_g})\varepsilon_H}{j_m C_p}, \tag{5.11}$$

where, $T_{in} = 300\ K$, is the initial electrolyte temperature, and $C_p = 4.2\ Jgm^{-1}K^{-1}$, is the specific heat capacity of the electrolyte (assumed to be equal to that of water). Hence, it is important to estimate T_{PV} in realistic operating conditions, as well as the temperature dependent behaviour of the electrocatalytic system.

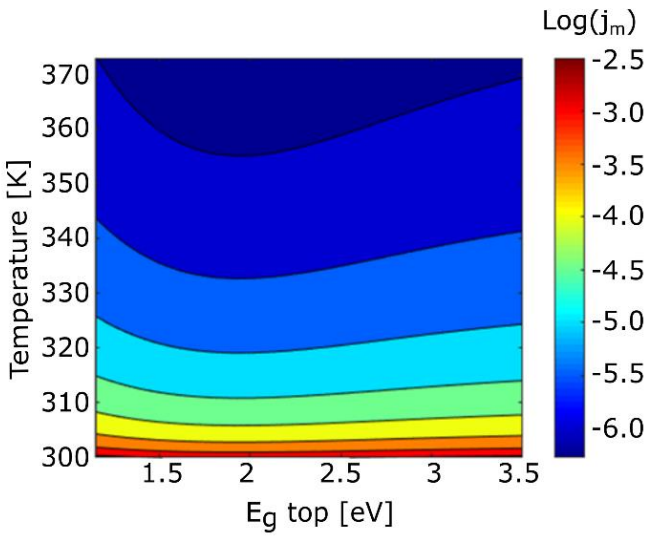

Figure 5.3: Mass flux rate as a function of required electrolyte temperature and top cell bandgap, for a PV cell operating at 373 K. The mass flux rate is given on a log scale. Bandgaps associated with maximum/high STH efficiency require slower mass flow rate for maximum heat transfer.

5.4.1. Estimation of practically achievable PV component operating temperatures

As a first step, we consider a steady state thermal model to estimate the practically attainable PV cell temperatures using energy balance equations [172]. The PV cell is in thermal equilibrium with a black body such that its emissivity $\epsilon_{PV} = 1$. This means that the below bandgap and thermalisation energy losses are absorbed and generate heat in the PV cell. To simulate the conditions in a realistic solar module, the PV cell is separated by an air gap from a glass plate cover with emissivity, $\epsilon_{glass} = 0.9$, and is otherwise insulated. The incident solar radiation is transmitted through the glass and absorbed by the PV cell, while radiation losses

from the cell can leave the system. As the cell heats up, emission losses increase. The PV component loses heat to the glass by radiation and convection across the air gap, Δx. In turn, the temperature of the glass, T_{glass}, increases and loses heat by radiation and convection to the environment (assumed to be at $T_{air} = 300\ K$). **Figure 5.4** shows the schematic of PV component for calculating practical PV operating temperatures (T_{PV}).

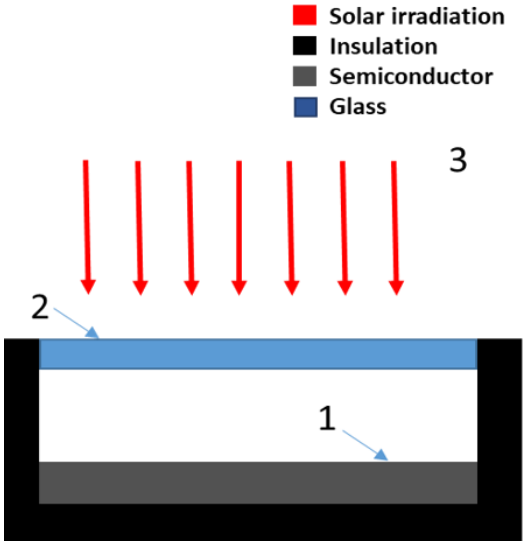

Figure 5.4: PV component schematic for estimated temperature calculations

Here, surface 1 is the Photovoltaic (PV) component, surface 2 is glass and, surface 3 is air.

The radiosity of a surface, J_r, is defined as the sum of energy emitted and the energy reflected when no energy is transmitted:

$$J_r = \epsilon E_b + \rho G \tag{5.12}$$

where, ϵ is emissivity, E_b is blackbody emissive power, ρ is reflectivity, and G is total irradiation incident upon a surface per unit time per unit area. It is assumed that glass does not transmit any of the thermal radiation, then the reflectivity can be defined as,

$$\rho = 1 - \alpha = 1 - \epsilon \tag{5.13}$$

where, α is the absorptivity or the fraction absorbed.

Replacing value of ρ from equation (5.13) in (5.12) we can rewrite J_r as

$$J_r = \epsilon E_b + (1 - \epsilon)G \tag{5.14}$$

When many heat transfer surfaces are involved, the energy balance can be written using nodal equations [172]. Net heat lost Q', is the difference of energy emitted and energy absorbed. This can be written mathematically as,

$$Q' = \epsilon E_b - \alpha G \tag{5.15}$$

Considering a system with many heat transfer surfaces, for the i^{th} surface, the total irradiation is the sum of all radiation G_j from all the other j surfaces. Thus for $\epsilon = \alpha$

$$Q_i' = \epsilon_i(E_{b_i} - \sum_j G_j). \tag{5.16}$$

The total irradiation, G, can be expressed in terms of radiosity and shape factor, F_{ji} as

$$G_j A_i = A_j J_{r_j} F_{ji} \tag{5.17}$$

where, A_j and A_i are areas of j^{th} and i^{th} surface, respectively.

From reciprocity

$$A_j F_{ji} = A_i F_{ij} \tag{5.18}$$

Substituting the value from equation (5.18) in equation (5.17) and then value of G_j in equation (5.19) we get,

$$Q_i' = \epsilon_i \left(E_{b_i} - \sum_j F_{ij} J_{r_j} \right). \tag{5.19}$$

Heat transfer can also be calculated as,

$$Q_i' = J_{r_i} - G_i = \left(J_{r_i} - \sum_j F_{ij} J_{r_j} \right). \tag{5.20}$$

Combining equation (5.19) and (5.20) gives us the radiosity of the i^{th} surface as:

$$J_{r_i} - (1 - \epsilon_i) \sum_j F_{ij} J_j = \epsilon_i E_{b_i}. \tag{5.21}$$

The heat transfer rate at each i^{th} surface can then be calculated from

$$Q_i' = \frac{\epsilon_i}{1-\epsilon_i} \left(E_{b_i} - J_{r_i} \right). \tag{5.22}$$

Solving the equation (5.22) for E_b gives us:

$$E_{b_i} = J_{r_i} + \frac{1-\epsilon_i}{\epsilon_i} Q_i' \tag{5.23}$$

Substituting equation (5.23) into (5.21) then gives us:

$$J_{r_i} = \frac{1}{1-F_{ii}} \left(\sum_{j \neq i} F_{ij} J_{r_j} + Q_i' \right) \tag{5.24}$$

We then use this derivation for a many surface system for our current system, and can rewrite equation (5.24) for the PV surface as

$$J_{r_{PV}} = \frac{1}{1-F_{11}} \left(\sum_{j \neq i} F_{1j} J_{r_j} + Q_{PV}' \right) \tag{5.25}$$

Solving the equation above and substituting the value $F_{11} = 0$ for $J_{r_{PV}}$ we get

$$Q_{PV}' = E_{b_{PV}} - F_{12} J_{r_{glass\_i}} \tag{5.26}$$

For PV cells in thermal contact to a black body absorber, ϵ = 1, and the total radiation emitted by the PV cell is $E_{b_{PV}}$, following the Stefan- Boltzmann law, $E_{b_{PV}}$ can be represented by:

$$E_{b_{PV}} = \sigma T_{PV}^4 \tag{5.27}$$

where, σ = $5.67 \times 10^{-8} Wm^{-2}K^{-4}$ is the Stefan-Boltzmann constant. The heat Q'_{PV}, transferred over to the PV component (surface 1), from the glass (surface 2), by convection the, is then given by:

$$Q'_{PV} = \frac{k_e}{\Delta x}\left(T_{glass} - T_{PV}\right) + Q'_{heat} \,. \tag{5.28}$$

where, $k_e = 0.059\, Wm^{-1}K^{-1}$ is the thermal conductivity of the air gap between the semiconductor and the glass and Q'_{heat} is heat transfer across the surface.

This, Equation (5.16) and (5.26) can be combined to get

$$E_{b_{PV}} - F_{12} J_{r\,glass\_i} = \frac{k_e}{\Delta x}\left(T_{glass} - T_{PV}\right) + Q'_{heat} \tag{5.29}$$

Where $J_{r\,glass\_i}$ is the radiosity inside the glass and F_{12} is the shape factor (fraction of energy leaving surface 1 and reaching surface 2) .

The overall energy balance for surface 2 (glass) can be defined by energy balance equation, and written as:

$$\frac{\epsilon_{glass}}{1-\epsilon_{glass}}\left(2E_{b_{glass}} - J_{r\,glass\_i} - J_{r\,glass\_o}\right) = \frac{k_e}{\Delta x}\left(T_{PV} - T_{glass}\right) + h_c\left(T_{air} - T_{glass}\right) \tag{5.30}$$

where, $h_c = 20\, Wm^{-2}K^{-1}$ is the convective heat transfer coefficient of air. For the overall system, a fraction of solar energy absorbed will eventually be lost by convection and radiation (Q'_{loss}) from the outside surface of glass (contributing to heat loss):

$$Q'_{heat} = h_c(T_{air} - T_{glass}) + \epsilon_{glass}\left(E_{b_{glass}} - E_{b_{air}}\right) . \quad (5.31)$$

Radiation lost from outside of the glass can be written in two ways,

$$Q'_{rad} = \epsilon_{glass}\left(E_{b_{glass}} - E_{b_{air}}\right) = \left(E_{b_{glass}} - J_{r\,glass\_o}\right)\frac{\epsilon_{glass}}{1-\epsilon_{glass}} \quad (5.32)$$

Solving above equations and rearranging them we get the energy balance equations for the overall system as,

$$\epsilon_{glass}\left(E_{b_{PV}} + E_{b_{air}} - 2E_{b_{glass}}\right) + \frac{k_e}{\Delta x}(T_{PV} - T_{glass}) + h_c(T_{air} - T_{glass}) = 0 \quad (5.33)$$

$$\epsilon_{glass}\left(E_{b_{glass}} - E_{b_{PV}}\right) + \frac{k_e}{\Delta x}(T_{glass} - T_{PV}) + Q'_{heat} = 0 \quad (5.34)$$

We can then estimate T_{PV} and T_{glass} by solving the energy balance equations as a function of top cell bandgap (through $L_{th} + L_{E_\gamma < E_g}$) for a 2-T PV configuration.

$$Q'_{heat} = L_{th} + L_{E_\gamma < E_g} \quad (5.35)$$

Also, From equation (5.27)

$$E_{b_{PV}} = \sigma T_{PV}^4$$

$$E_{b_{glass}} = \sigma T_{glass}^4$$

Subtracting equation (5.33) and (5.34) gives

$$-\epsilon_{glass}E_{b_{glass}} - hT_{glass} + (\epsilon_{glass}E_{b_{air}} + h_cT_{air} + (L_{th} + L_{E_\gamma<E_g})) = 0 \qquad (5.36)$$

PV temperature is calculated by solving (5.34), (5.35) and (5.36)

Figure 5.5 shows the calculated cell temperatures as a function of heat loss for single and 2-T PV tandem PV systems with fixed bottom Si cell.

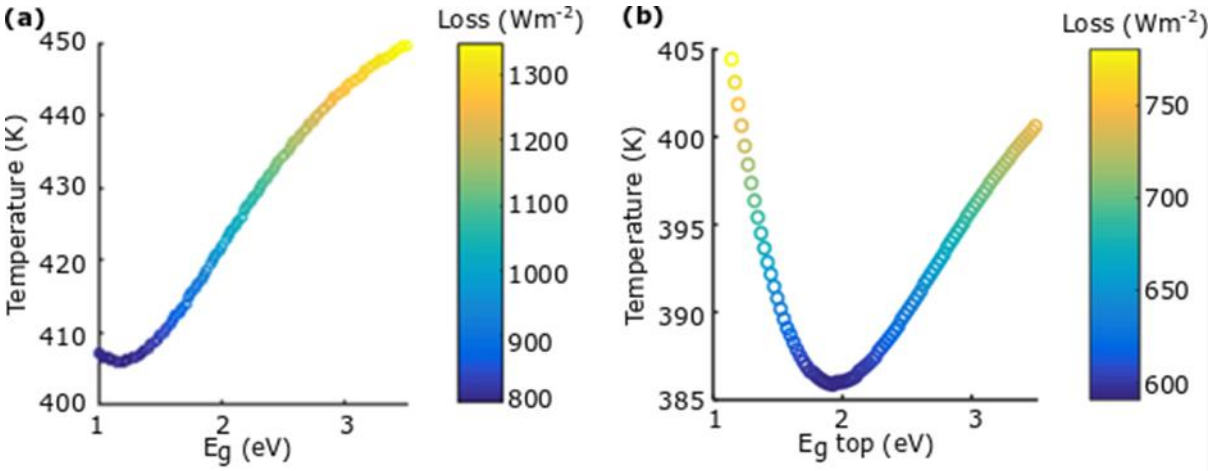

Figure 5.5: Maximum cell temperatures as a function of heat loss and (a) solar cell bandgap for single bandgap cell and (b) top cell bandgap for 2-T PV tandem with fixed bottom silicon cell

5.4.2. PV cell performance at elevated temperatures

The practically attainable PV cell operating temperatures under one sun illumination (black line); and the PCE of the PV component as a function of top cell bandgap and temperature are

given in **Figure 5.6**. Our calculations show that the PV cell temperatures can reach over 373 K (100 ℃) under one-sun operating conditions for all the top cell bandgaps investigated, in agreement with measured, roof-mounted module temperatures reported in [173]. Operating the PV cell at higher temperatures increases recombination and thermal losses, reducing the PCE of the device. For example, the PCE of PV component with a top cell bandgap of 1.73 eV reduces by 3% absolute at an operating temperature of 400 K compared to its performance at room temperature.

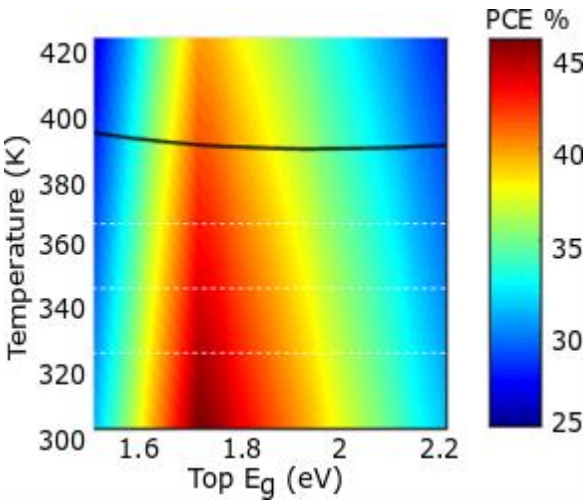

Figure 5.6: Surface plot of PV efficiency as a function of PV temperature and top cell bandgap for 2-T tandem configuration with bottom Si cell. The black line on the plot represents the maximum achievable cell temperature for given bandgap configurations.

The PV temperatures calculated here represent the upper limit of the electrolyte temperature assuming perfect heat transfer. These results demonstrate that it would be possible to heat the electrolyte to temperatures in the operating range of commercial PEM electrolysers, by optimising the electrolyte mass flux rate (i.e., the mass flow per unit area). The mass flux rates

required to attain these electrolyte temperatures are given in figures 5.3. These are consistent with realistic mass flow rates reported in literature [174] .

5.4.3. Temperature dependence of the catalytic reaction

To develop a thermally integrated PEC system, it is important to understand the temperature dependence of the water-splitting reaction and electrocatalytic system. Both, the Gibbs free energy, G, and the activation overpotential in the electrochemical system are sensitive to the operating temperature, T. The reaction potential required for water-splitting is defined by the Nernst equation and also depends upon temperature [83]. The dependence can be expressed by the Gibbs-Helmholtz thermodynamic relation between enthalpy, H, and G, given by [175]

$$\frac{\partial\left(\frac{G}{T}\right)}{\partial T} = -\frac{H}{T^2}$$

The change in Gibbs free energy of the reaction is due to the change in enthalpy, ΔH^0_{rxn}, and entropy, ΔS^0_{rxn}, of the reaction[16, 80, 81] as given by equation 2.8 in Chapter 2. The enthalpy of the reaction reduces by < 1% over the range of temperature considered here (300-400 K), while $T\Delta S^0_{rxn}$ increases significantly, by almost 20%. This reduces the Gibbs free energy required for dissociation of the water molecule and hence reduces the reaction potential required to drive the water-splitting reaction as the temperature increases.

An additional overpotential is needed to overcome the activation energy barrier for the reaction to proceed, calculated using the temperature-dependent Butler Volmer equation for redox reactions [80, 82-84]. The pre-exponential and activation energy values depend on crystallinity

and morphology of the catalyst and can result in different activation overpotential values [176]. The temperature dependence of the catalyst is also sensitive to the configuration and geometry of the electrodes, as well as the catalyst material [176]. To estimate an upper limit on performance, we assume a high-performance catalytic system based on the noble metals (Pt and IrOx) and choose representative values based on previous work [90]. Details of the electrochemical model are given in Chapter 2, section 2.2.

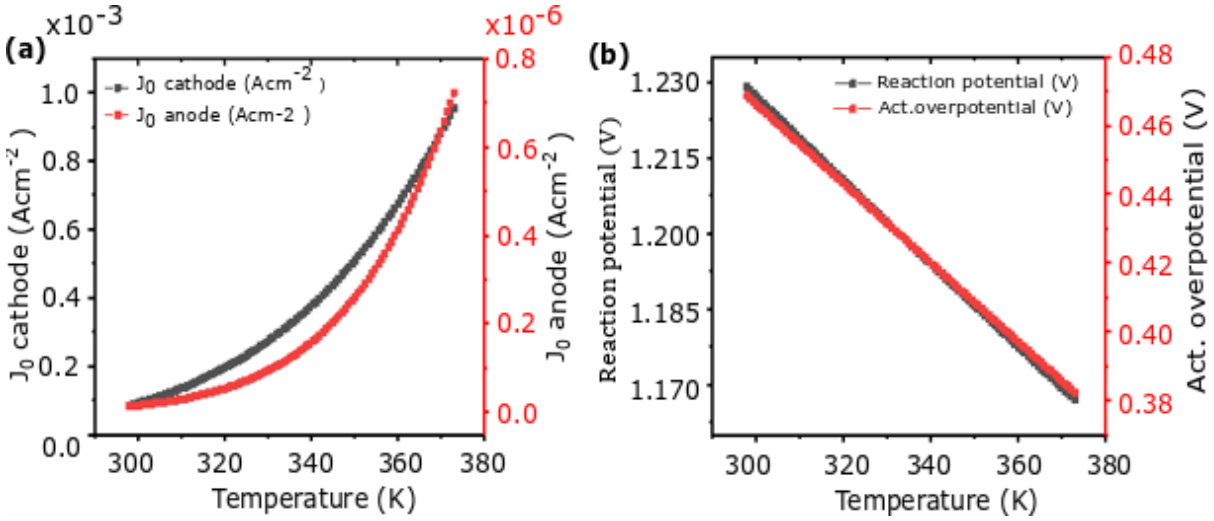

Figure 5.7: (a) Exchange current density of the anode and cathode as a function of temperature for Platinum and Iridium oxide catalyst (b) Reaction potential and activation overpotential as a function of temperature for Pt and IrOx catalyst.

Figure 5.7 (a) shows the temperature dependence of exchange current densities for the cathode, $J_0 cathode$, and anode, $J_0 anode$, for Pt and IrOx catalytic systems, respectively. Figure 5.7 (b) shows the temperature dependence of reaction potential and activation overpotential. It should be noted that the anode exchange current density values are roughly 3 orders of magnitude smaller than those of the cathode, which limits the reaction and determines the

activation overpotential [16]. The data shows that increasing the operating temperature increases the exchange current density of the anode and cathode, in agreement with literature [176]. The high exchange current density at elevated temperatures facilitates the reaction, reducing the activation overpotential, as shown in Figure 5.6 (b). Specifically, the reaction potential for water-splitting reduces by 7% over the range of temperature considered here (300-400 K).

5.4.4. Performance of the thermally integrated system

The final step is to integrate the temperature-dependent reaction properties into the ideal PEC system model for DSHG described above. To analyse the potential of thermal integration, we calculate the STH efficiencies as a function of operating temperature and top cell bandgap.

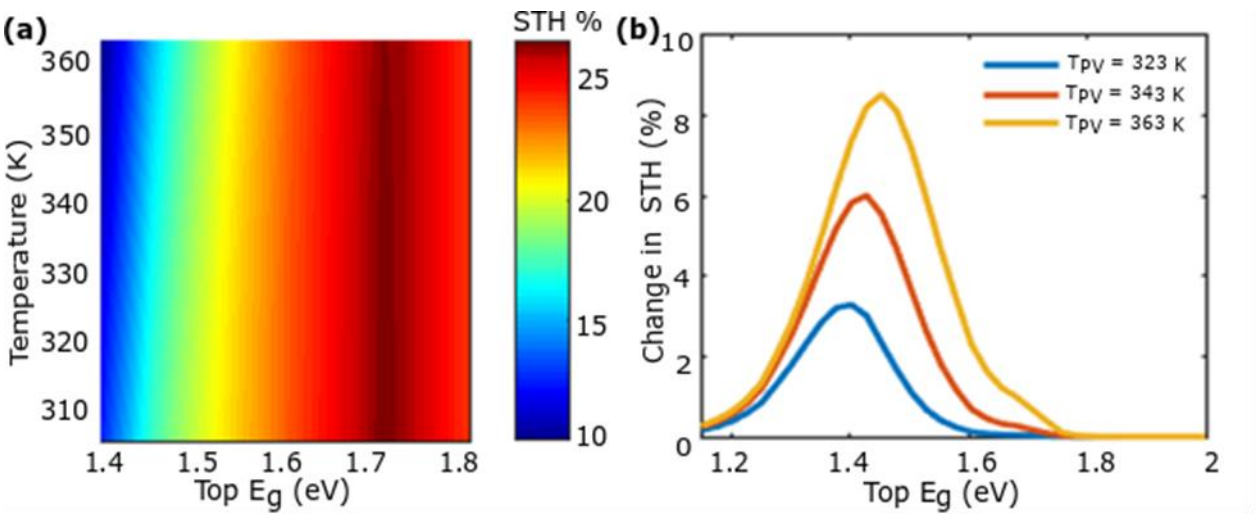

Figure 5.8: (a) Ideal STH efficiency for a thermally integrated system as a function of top cell bandgap ($E_g top$) and operating temperature of the system ($T_{PV} = T_{EC}$) (b) Absolute change in ideal STH efficiency ($\mathrm{STH}_{\text{thermal integration}} - \mathrm{STH}_{\text{no-thermal integration}}$) due to thermal

integration as a function of top cell bandgap for three different operating temperatures. The coloured circles in indicate the absolute Ideal STH efficiency without thermal integration in (a) corresponding to the change in STH in (b).

Figure 5.8 (a) shows the overall ideal STH efficiency of thermally integrated PV-based solar hydrogen generation systems, where $T_{PV} = T_{EC}$, over a range of temperatures from 298 K to 363 K. In all cases the ideal STH decreases with increasing operating temperature due to a reduction in the PV efficiency. However, thermal integration does help to mitigate the reduction in STH with increasing temperature compared to a non-thermally integrated system. Figure 5.8 (b) shows the absolute difference in STH efficiency with and without thermal integration, for three different PV operating temperatures. The coloured circles correspond to absolute STH efficiency in figure 5.8 (a). The STH efficiency of the PV-based solar hydrogen generation system increases significantly upon thermal integration for all three operating temperatures compared to a non-thermally integrated system up to 8.5% for certain top cell bandgaps. However, the maximum improvement for each temperature investigated, indicated by a coloured circles in Figure 5.8 (b), occurs at relatively low absolute STH efficiencies, corresponding to coloured circles shown in Figure 5.8 (a). For example, at a top-cell bandgap of 1.6 eV, thermal integration only improves the STH efficiency by 2.3%. These results demonstrate that the benefit of thermal integration can be significant but is sensitively dependent on the tandem cell bandgap combination.

5.5. Modelling realistic solar hydrogen generation system

The thermodynamic efficiency and intrinsic loss calculations for ideal - systems, given above, are useful for quantifying the relative contribution of different loss mechanisms. However,

realistic solar hydrogen systems suffer from additional, unavoidable material dependent losses which need to be taken into account when assessing the potential of different loss mitigation techniques to increase practically achievable STH efficiency.

In this section, we model realistic systems by including loss factors to account for non-ideal diode characteristics in the photovoltaic components, and material-dependent reaction overpotential losses in the catalytic components. We model the realistic PV and catalyst components under 1-sun conditions (using the AM1.5G spectra) using the temperature-dependent transcendental solar cell equation and the temperature-dependent Butler-Volmer and Nernst equations, where realistic losses in the system are introduced through loss parameters fit to experimental data.

The total input solar irradiation is equal to AM1.5G solar spectrum, given by equation (2.16), Chapter 2 and restated below

$$P_{in} = \int_0^{\infty} AM1.5G(E)dE \tag{5.39}$$

The photovoltage of a realistic PV component is given by solving the transcendental solar cell equation and loss parameters are introduced to account for non-ideal absorption, non-ideal recombination, and non-ideal diode behaviour.

$$V_{PV}(J) = \frac{kT_{PV}}{q} ln\left(\frac{J_L - J - \left(\frac{V_{PV}(J) - R_S J}{R_{sh}}\right)}{J_{rad}} + 1\right) - JR_s, \tag{5.40}$$

where, J_L, is the photocurrent, J_{rad} is the radiative recombination, $T_{PV,}$ is the temperature of the photovoltaic component, R_s and R_{sh} are the series and shunt resistance, respectively.

To determine non-ideal photo-current we calculate realistic absorption spectra, $A(E)$, and define the collection efficiency, f_c, to account for any charge carrier collection losses [21]. The absorption in the Si cell, $A_{Si}(E)$, is calculated as described below, assuming Lambertian light trapping and no reflection loss, following the work of Green [177], while a bandgap dependent analytical approximation is used to reproduce the shape of the absorption spectra of the top cells. An additional loss factor, f_{Para}, is defined for the top cells to account for parasitic absorption that would reduce the light incident on the bottom cell.

The photocurrent for the top cell is then given by:

$$J_{L,top} = qf_c \int_{AM1.5g} A_{top}(E)\phi(E)dE \tag{5.41}$$

where, $\phi(E)$ the incoming photon flux from a black body defined by eqn (2.15), Chapter 2

and for the bottom Si cell as,

$$J_{L,Si} = qf_c \int_{AM1.5g} A_{Si}(E)\big(1 - A_{top}(E) - A_{para}(E)\big)\phi(E)dE \tag{5.42}$$

For the bottom Si cell, resistive losses due to carrier transport in the semiconductor are introduced through the series resistance term, R_s, and non-ideal diode characteristics are

introduced through the shunt resistance, R_{sh}. The series and shunt resistances are modelled using the normalised resistance, r_s, r_{sh} for each cell, defined as

$$r_{s/sh} = R_{s/sh}\,\frac{J_L}{V_{oc}} \tag{5.43}$$

The loss parameters are fitted to reproduce the reported experimental current-voltage curves and solar cell.

5.5.1. Absorption in a single silicon cell

The absorption in the Si cell is calculated with Lambertian light trapping and no reflection loss, following the work of Green [177],

$$A_{Si} = \frac{1-\exp(-2\alpha_{Si}W)}{1-\left(1-\frac{1}{n_{Si}^2}\right)\exp(-2\alpha_{Si}W)} \tag{5.44}$$

Where, α_{Si} and n_{Si} are the wavelength dependent absorption coefficient and refractive index of crystalline Si. To account for absorption in the top cell, A_{Si} is multiplied by the transmission of the top cell, T_{Top}, the calculation of which is described below. A collection efficiency, f_c, defined as the fraction of photogenerated carriers that contribute to the current.

The temperature dependent bandgap of Si cell is calculated as [178]

$$E_g(T) = E_g(0) - \frac{\alpha T_{PV}^2}{(T_{PV}+\beta)} \tag{5.45}$$

where $E_g(0) = E_g$ at $T_{PV} = 0\ K$, and α and β are empirical parameters.

The light induced current is then calculated by integrating the product of these three terms with the photon flux in the AM1.5G solar spectrum:

$$J_{L,Si} = Aq \int_{E_{g\_bottom}}^{\infty} f_{c,Si} A_{Si} T_{Top} \phi(E) dE \quad (5.46)$$

5.5.2. Absorption in tandem configurations

Absorption in the silicon bottom cell

In tandem configuration, Si bottom cell receives the spectrum filtered by the top PV cell. Hence, we modified the limits of the integral to calculate the photocurrent of the Si bottom cell, considering the change in input spectrum.

$$J_{L,Si} = Aq \int_{E_{g\_bottom}}^{E_{g\_top}} f_{c,Si} A_{Si} T_{Top} \phi(E) dE \quad (5.47)$$

Absorption in the top cell

The total, bandgap dependent recombination current can be calculated as [178, 179]

$$J_{rad} = K' T_{PV}^3 \, exp\left(-\frac{eE_g}{kT_{PV}}\right) \quad (5.48)$$

where K' is an empirical parameter and E_g is the semiconductor bandgap.

To determine the photocurrent we calculate the absorption, and define the collection efficiency as before, $f_{c_{Top}}$

$$J_L = Aq \int_{E_{g\_top}}^{\infty} f_{cTop} A_{Top} \phi(E) dE \tag{5.49}$$

A simple, bandgap dependent, analytical approximation is used to model the shape of the absorption spectra of the top cells,

$$A_{Top} = 0.45\, erf\left(\frac{E-E_g}{\frac{5kT_{PV}}{q}}\right) + 0.05 erf\left(E - E_g\right) + 0.05 \tag{5.50}$$

An additional parameter is introduced to include parasitic (below bandgap) absorption in the top cell, f_{Para}:

$$A_{Para} = f_{para}\, erf\left(\frac{E-E_g}{\frac{kT}{q}}\right), \quad E < E_g \tag{5.51}$$

The transmission through the top cell is then calculated as:

$$T_{Top} = 1 - A_{Para} - A_{Top} \tag{5.52}$$

The bandgap dependent series and shunt resistances are modelled using a single normalised resistance for each cell type

$$r_{s/sh} = R_{s/sh} \frac{J_{sc}}{V_{oc}} \tag{5.53}$$

5.5.3. Fitting procedure

The three loss parameters for the Si cell - collection efficiency, $f_{c_{Si}}$, series, R_s, and shunt resistance, R_{sh} - are chosen to give the best fit to the solid state J-V measurements of the photovoltaic device reported by Park [65]**.** Once the Si cell parameters are chosen, $f_{c_{Top}}$ and f_{Para} were chosen to closely match the EQE profile of the perovskite cell. After fixing these parameters, K', r_s, and r_{sh} are chosen such that calculated IV-curves and the figures of merit of the top perovskite solar cell matched as reported in reference. The reported and calculated figures of merit are given in Table 5.1 below.

Table 5.1: Figures of merit for the reported and modelled photovoltaic components

Figures of Merit	Reported	Modelled
Bandgap (eV) top cell	1.6	1.6
Bandgap (eV) bottom cell	1.1	1.1
V_{OC} (V)	1.7	1.7
$J_{sc}(mAcm^{-2})$	17.76	17.7
Tandem efficiency (%)	23.1	23.1
Solar to Hydrogen efficiency (%)	17.5	17.5

Table 5.2: Parameters for modelling reported PV components

Parameters	Filtered Silicon	Top cell
Empirical parameter, K	5.5e+2	1e+4
Normalized series resistance, r_s	6.2e-1	0.6e-1
Normalized Shunt resistance, r_{sh}	5e+1	1e+1
Collection efficiency, f_C		0.73
$E_g(0)$	1.170	-
$\alpha(eVdeg^{-1})$	4.730e-4	-
$\beta(\text{deg})$	636	-

The catalytic exchange current density and activation energy values are chosen to best fit to the experimental data and obtain the reported solar to hydrogen conversion efficiency for the reported work.

Table 5.3: Parameters for modelling reported catalyst components

Parameters	Anode	Cathode
Pre exponential factor	142e+4	46.2e+4
Activation energy	34.3e+3	12e+3

5.6. Comparing different loss mitigation techniques in realistic systems

To compare the relative improvement in the STH efficiency for different loss mitigation techniques, we model a low-cost, high efficiency system, consisting of perovskite-Si tandems coupled with Earth-abundant catalysts. We base our model on the work of Park et.al, who have reported STH = 17.5% for a coupled system under standard operating conditions [65]. For the decoupled case, we also include the efficiency loss due to the PMU, taken to be 97%, which is consistent with literature [180-184].

Figure 5.9 (a) shows the STH efficiency for a realistic Perovskite-Si tandem based system with and without different loss mitigation techniques applied. Data is shown at three different temperatures corresponding to the operating temperature range of a standard commercial electrolyser: room temperature (300 K); an intermediate temperature (323 K); and a high temperature (343 K).

At room temperature, the standard coupled system without any loss mitigation demonstrates an STH efficiency of 17.5%, in agreement with the reported results [65]. As expected, the STH efficiency reduces with increasing temperature to 10.9% at a high operating temperature (grey circles). By implementing thermal integration (red squares), the STH efficiency of the coupled system is improved to 13.4% at 343 K.

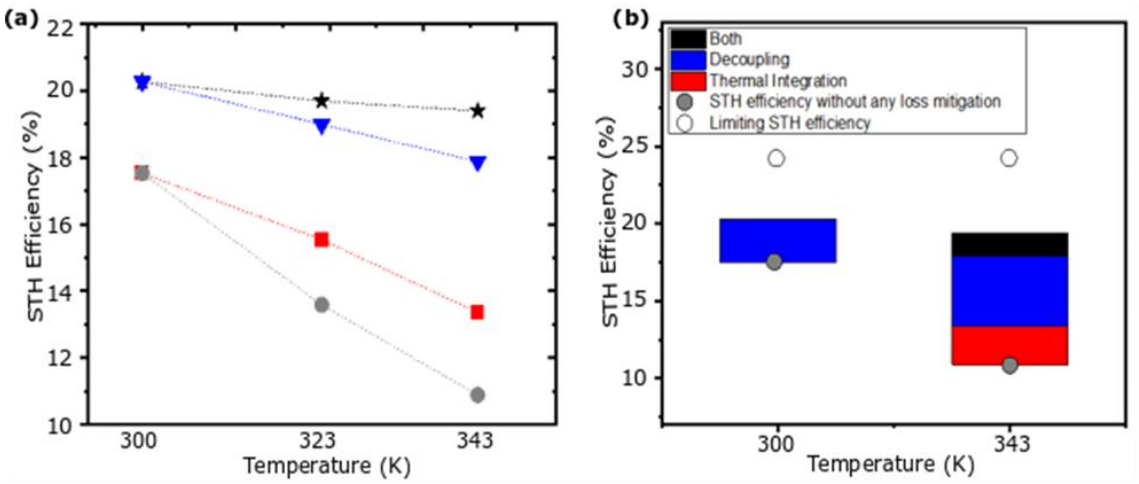

Figure 5.9: (a) Solar to hydrogen conversion efficiency for perovskite-Si tandems without (grey circles) and with different loss mitigation techniques: thermal integration (red squares), decoupling (blue triangles), both thermal integration and decoupling (black stars). Results are given at three different temperatures: room temperature (300 K); an intermediate temperature (323 K); and a high temperature (343 K) (b) Solar to hydrogen conversion efficiency as a function of different loss mitigation techniques at room temperature (300 K) and high temperature (343 K). Grey circle represents the solar to hydrogen conversion efficiency without any loss mitigation and white circle represents the theoretically limiting solar to hydrogen conversion efficiency. Coloured blocks represent solar hydrogen generation system with different loss mitigation techniques: thermal integration (red), decoupling (blue), and both thermal integration and decoupling (black).

If we remove integration losses by decoupling the system (blue triangles) the STH efficiency is increased to 20.3% at room temperature, reducing to 17.9% at high operating temperatures without any thermal integration. Combining the two different loss mechanism techniques gives

maximum improvement resulting in an STH efficiency of 19.4% at realistic operating temperatures of 343 K for a thermally integrated decoupled system.

Figure 5.9 (b) compares the realistic case study directly with the ideal thermodynamic limits calculated earlier, to show the effect of different loss mitigation techniques at room temperature (300 K), and high temperature (343 K). White circles represent the theoretically limiting STH efficiency, while grey circles represent the STH efficiency without any loss mitigation. The coloured bars show the improvement in solar to hydrogen conversion efficiency due to different loss mitigation techniques. These results demonstrate that the two loss mitigation techniques provide significantly different performance enhancements. At high operating temperatures, thermal integration improves the STH efficiency of the coupled system by 23% relative to a coupled system without any thermal integration. By comparison, decoupling the system can improve STH efficiency by 16% at room temperature, and by 64% at high operating temperature (343 K). Combining the two loss mitigation techniques results in improvement of 78% for a thermally integrated decoupled system at higher temperature relative to non-thermally integrated coupled system.

For thermal integration, we consider perfect heat transfer from the PV to EC components. We assume the electrolyte temperature equal to the PV operating temperature for STH efficiency calculations for thermally integrated system. However, perfect heat transfer is not possible in practical conditions, and the system will always suffer losses during the heat transfer process. This could result in electrocatalytic system operating at a lower temperature than the PV and reduce the efficacy of thermal integration.

Both thermal integration and decoupling will add to the costs and complexity of the system. Decoupling the system increases the cost of the PV component due to the need for a PMU, while thermal integration will result in increased costs for balance of plant, particularly in the case of monolithic systems where hydrogen gas collection systems will need to be decentralised. We have avoided a detailed techno-economic comparison of the systems considered here because of the difficulty in cost estimations for emerging technologies, and the loss of generalisation. However, it will be important to understand the economics of different loss mitigation techniques for commercial systems. In all cases it will be necessary to ensure that the concurrent increase of system complexity and cost is justified by the improvement in the STH efficiency.

5.7. Conclusion

The comprehensive system analysis in this Chapter allows us to quantify the losses in the solar hydrogen generation and compare loss mitigation techniques that can be employed to improve the STH efficiency.

We show that for an ideal Si-tandem based system, thermal and system integration losses account for the majority of energy losses. In total, 19% of the input solar radiation is lost due to system integration and 38% due to thermal losses. This suggests that the two-loss mitigation techniques – thermal integration and optimal system integration strategies are most important for optimising performance.

These loss mitigation techniques are a useful tool in targeting the major losses in solar hydrogen systems, and we show that they can achieve STH efficiencies above 20% for realistic, low-cost

solar hydrogen systems. Thermal integration can significantly improve the STH efficiency for low-cost perovskite-Si tandem PV and earth abundant catalyst-based realistic systems. However, the benefit of thermal integration is sensitive to the operating temperature and the tandem PV bandgap combination. Decoupling the system improves the STH efficiency even at low temperatures and provides more than three times the performance boost of thermal integration at high operating temperatures. Our results show that optimal system integration strategies provide a much larger improvement in performance than thermal integration.

Ultimately, the best design choice is the one that will give the lowest cost of hydrogen. To achieve this, there will be a trade-off between high efficiency and reducing hydrogen production costs. For this reason, it is critical to quantify the impact of different loss mitigation techniques to ensure the best performance for the lowest additional costs.

Chapter 6

Direct Solar Hydrogen Generation at 20% Efficiency Using Low-Cost Materials

6.1. Introduction

In this Chapter, we demonstrate direct solar hydrogen generation using an all-low-cost materials-based PEC system consisting of perovskite-Si PV tandem and Ni-based earth-abundant catalysts in PV-EC configuration. We discuss the current PV tandem based system architecture for unassisted solar hydrogen generation and its benefits in section 6.2. Section 6.3 covers the synthesis and electrochemical characterisation of NiMo-based HER catalysts with an innovative 'flower-stem' morphology, with increased reaction sites and NiFe/NF oxygen evolution reaction catalysts. In section 6.4 we describe the development of perovskite solar cells with an unprecedentedly high open circuit voltage enabled by an optimised perovskite composition and improved surface passivation and present the performance of 2-T perovskite-Si PV tandem. When the NiMo hydrogen evolution catalyst is combined with an optimally designed NiFe-based oxygen evolution catalyst and a high-performance perovskite-Si tandem cell, the resulting integrated water splitting cell achieves a record STH efficiency of 20%, as discussed in section 6.5. In section 6.6 we discuss potential ways to increase the STH efficiency. Detailed analysis of the integrated system reveals that simply decoupling the system could improve the STH efficiency to 23%, while efficiencies of 25% could be achieved with realistic improvements in the perovskite cell in a coupled system. Decoupling this system further can improve the STH to 32%. In section 6.7, we perform a technoeconomic analysis to

assess the cost competitiveness of direct solar hydrogen generation systems compare to off-grid electrolyser system powered by commercial Si PV module or perovskite-Si tandem reported in this work. The calculated LCOH is estimated at $4.1/Kg for the current system, which can reduce to below ~$3.0/Kg with projected cost reductions in PV modules and membranes in future. We show that combining the predicted improvement in efficiency to 25% and cost reductions in components can improve the STH efficiency to ~$2.3/Kg.

This work was done in collaboration with Dr Chuan's group in the University of New South Wales (UNSW) and Dr. The Duong from the perovskite PV research group at The Australian National University (ANU). I designed the solar hydrogen generation system and evaluated the requirements to achieve 20% STH efficiency. I worked closely with Dr Yuan Wang and her team at UNSW who synthesised and characterised the HER and OER catalysts. We worked towards designing catalytic system for optimum current and voltage matching with the PV component to achieve 20% STH efficiency. Dr The Doung from ANU developed the high semi-transparent perovskite solar cells and performed PL and stability measurements. I worked closely with Dr The Duong in design requirements for perovskite cells, particularly the need of voltage improvement to match with catalysts for achieving high efficiency. I performed solar hydrogen generation system integration, characterisation, and analysis. I further analysed different ways to further improve the system to increase the STH efficiency. I performed the techno-economic analysis to assess the cost competitiveness of the current system and future pathways to improve. The text in the Chapter is adapted from a paper which is under review and is co-authored by Yuan Wang*, Astha Sharma* The Duong, Hamidreza Arandiyan, Tingwen Zhao, Doudou Zhang, Zhen Su, Magnus Garbrecht, Fiona J. Beck, Siva Karuturi, Chuan Zhao, and Kylie Catchpole. (*authors contributed equally to the paper).

6.2. Tandem PV based photoelectrochemical system for high efficiency direct solar hydrogen generation

In Chapter 4 we achieved an STH efficiency of 17% using perovskite PV cells and earth abundant catalysts integrated Si photocathodes in 2-T tandem architecture. The NiMo/Ni catalysts, developed using sputter deposition, show high performance and can be integrated with current Si manufacturing processes, but its performance is low compared to catalysts fabricated using wet chemical methods. To further improve the STH efficiency, we physically separate the PV and catalyst system in a PV-EC configuration, as discussed in Chapter 2 figure 2.2(a). Removing the requirement of integrating catalysts directly on the Si photocathode removes the restrictions for catalyst substrate and synthesis fabrication methods. Physically separating the PV and EC also allows for better voltage and current matching, as we are not restricted to size match the components.

As discussed in Chapter 4 section 4.3, earth abundant catalysts based on Ni alloys with other transition metals have shown excellent HER/OER performance and stability under harsh alkaline conditions[71-73, 75, 76]. Catalysts with larger numbers of reaction sites and good stability can be fabricated using wet chemical synthesis methods on a variety of substrates, resulting in high performance. Ni alloyed with Mo is a well-known non-noble metal-based electrocatalyst for HER under alkaline conditions.[73, 140, 141] Among Ni-based OER catalysts, NiFe (oxy)hydroxide presents a commendable performance for OER.[185-187] Although Ni-based catalysts have shown promise, their performance and operational stability need to be further improved, in order to match with PV cells, and construct robust, high-efficiency direct water splitting systems.

Achieving optimum voltage-current matching between PV and electrocatalytic components, in addition to fulfilling the voltage requirements for the water splitting reaction, is crucial in improving the STH efficiency. With Si solar cells already close to their practically achievable limits, improvements in the perovskite solar cell voltage is required in order to further improve the STH efficiency to attain the 20% benchmark.

As discussed in Chapter 5 and published in [22], PV-EC configuration also allows us to fully decouple the PV and EC components by introducing a PMU (Chapter 5, figure 5.1(d)). This eases the current and voltage matching requirements and the PV cells can be operated at its maximum power point and PMU provides optimised current and voltage to the EC component. This not only improves the STH efficiency but also the bandgap combinations to achieve high efficiency.

Previous experimental demonstrations of physically separated perovskite-Si PV tandem and catalyst systems have achieved STH efficiency of 18.7% using partially noble metal catalysts [188]. High STH efficiency of 17.5% is achieved using earth abundant Ni based catalyst with perovskite-Si tandem PV [65].

Despite promising results, reaching 20% STH efficiency is still elusive. In this Chapter we work towards improving both the PV and EC components and the device architecture to achieve the US DOE target of 2020 of 20% STH efficiency.

6.3. Synthesis and characterisation of electrocatalysts

The catalyst synthesis and characterisation were performed by Yuan Wang and team at the university of New South Wales. Details of catalyst fabrication and characterisation are given in Appendix B. I worked closely with them in designing the HER and OER catalysts, for optimum matching with the PV cells to achieve high STH efficiency. The section below includes a brief summary of the catalyst characterisation and performance analysis.

NiMo catalysts for HER were prepared on nickel foam (NF) using a two-step method involving hydrothermal synthesis and calcination in a reducing environment. As shown in the SEM images (**figure 6.1** a), high density flower-like nanosheets and stem-like nanowires resembling a flower-stem morphology grow uniformly on the 3-D NF skeleton. Such a morphology can improve electrolyte-catalyst interaction through capillary forces and reduce the adhesion of gas phase products, thereby enhancing the reaction kinetics[189]. The flower-like nanosheets are closely connected to the surface of the Ni foam through the stem-shaped nanowires, providing significantly enhanced accessible surface area with good mass and electron transfer properties. The unique "flower-stem" structure of the NiMo catalyst also provides a hierarchical architecture for uniform dispersion of highly active NiMo alloy nanograins (figure 6.1 b,c), thereby maximizing the catalytic performance. The performance of an electrocatalyst is highly dependent on its morphology. As discussed above the flower-stem morphology of the NiMo catalyst not only promotes increased number of accessible active sites, but also simultaneously facilitate efficient mass/charge transfer and fast gas bubble dissipation, resulting in an overall enhanced catalytic performance [190].

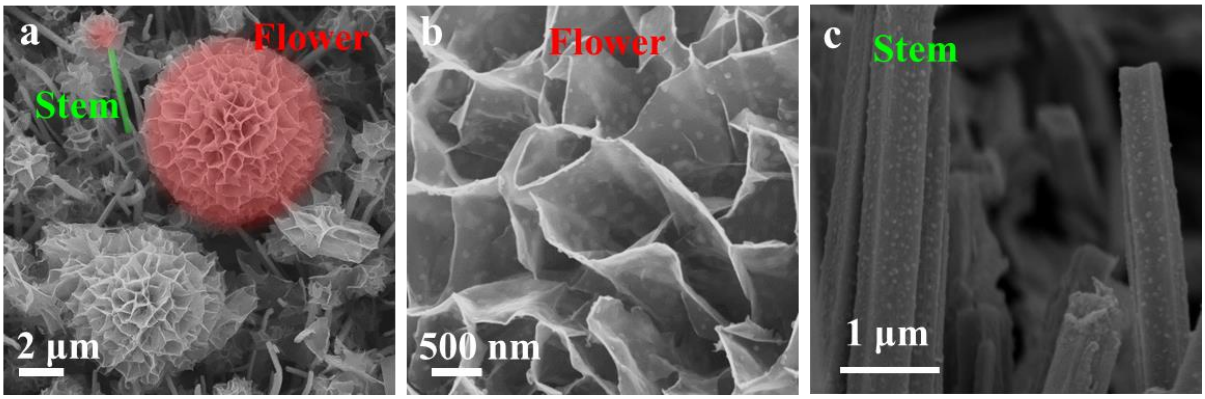

Figure 6.1: Scanning electron microscopy (SEM) images of NiMo/NF (a) flower-stem morphology (b) flower morphology (c) stem morphology

Electrochemical performance of the as-synthesised catalysts is tested in 1 M KOH in both three-electrode and two-electrode configurations to evaluate the individual HER and OER performances and the combined overall water splitting performance, respectively. Pt-C/NF and Ir-C/NF electrodes were used as benchmarks.

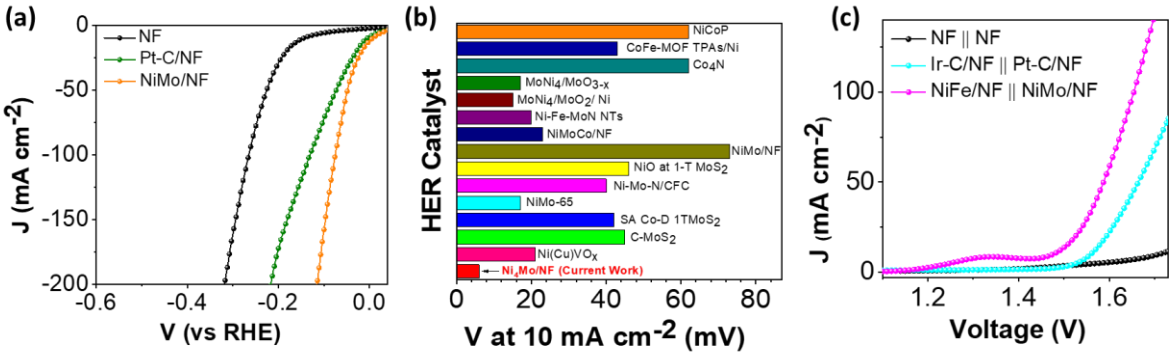

Figure 6.2: Electrochemical performance of HER and OER electrodes. (a) LSV curves of NiMo/NF, Pt-C/NF and NF electrodes for HER (b) Comparison of overpotential of NiMo/NF

at $mAcm^{-2}$ with other reported HER electrocatalysts. (c) LSV curves of NiFe/NF||NiMo/NF, Ir-C/NF||Pt-C/NF, NF||NF for overall water splitting in a two-electrode system using 1 M KOH.

As shown in **figure 6.2** (a), the as-synthesized NiMo/NF presents an HER onset potential close to the thermodynamic potential, and low overpotentials of 6 and 70 mV to obtain the current densities of 10 and 100 $mAcm^{-2}$. In comparison, the benchmark Pt-C/NF and unmodified NF show much higher overpotentials of 130 and 270 mV at 10 and 100 $mAcm^{-2}$, respectively. Moreover, the NiMo/NF electrode exhibits excellent longstanding stability, maintaining a stable HER activity at a high current density of 100 $mAcm^{-2}$ after 100 h of continuous operation (Appendix B). Such a performance ranks NiMo/NF catalyst among the best non-noble metal HER catalysts in alkaline media (figure 6.2 (b)).

The NiMo/NF HER electrode is combined with NiFe/NF OER electrode, in two electrode configuration to achieve overall water splitting. The NiFe/NF OER electrode is fabricated by electrodeposition and the details are given in Appendix B. Figure 6.2 (c) shows that the NiFe/NF||NiMo/NF delivers 10 $mAcm^{-2}$ current at a voltage of 1.48 V, which is 80 and 230 mV better than Ir-C/NF||Pt-C/NF and NF||NF, respectively. Besides the excellent activity, the NiFe/NF||NiMo/NF, shows high stability with no degradation at 20 $mAcm^{-2}$ after 100 h operation. In summary, the electrochemical performance tests confirm the as-developed NiFe/NF||NiMo/NF electrodes form a highly active and robust catalytic system for overall water splitting.

6.4. Perovskite-Si PV tandem for water splitting

To achieve stand-alone solar hydrogen production in an integrated system using the Ni-based electrodes, we fabricated perovskite and Si cells in 2-T tandem configuration. I performed the solar cell characterisation and solar hydrogen system integration and analysis were performed. Perovskite solar cell fabrication, PL and stability measurements were performed by The Duong at ANU.

Figure 6.3 (a) illustrates the device structure of the tandem cell consisting of a semi-transparent perovskite solar cell and a monocrystalline n-type Si solar cell. As discussed in Chapter 5 and published in [22]the perovskite cell bandgap is optimized at 1.72 eV, which is close to the ideal top-cell bandgap to achieve current matching with the Si bottom cell in the tandem configuration and to obtain the maximum STH efficiency.

Semitransparent perovskite solar cells were fabricated using a 3D perovskite light absorber ($Rb_{0.05}Cs_{0.095}MA_{0.1425}FA_{0.7125}PbI_2Br$). To realise high photovoltage, the surface of the active perovskite layer was passivated with a large organic cation n-dodecylammonium bromide ($C_{12}H_{28}BrN$) consisiting of a long alkyl chain, which is known to form two-dimensional (2D) perovskites.[191] The organic cation with long alkyl chain presents better surface passivation compared to the previously reported n-butylammonium bromide ($C_4H_{12}BrN$) which has a much shorter alkyl chain. Area matched bottom Si cells were fabricated with rear n-doped electron-selective passivation layer. [192] Details of solar cell fabrication and additional characersitation are given in Appendix C.

The J-V characteristics of the semi-transparent perovskite top cell and the silicon bottom cell were evaluated under continuous AM1.5G illumination (figure 6.3 (b)). The efficiency of the semi-transparent perovskite cell is 15.3%, with a V_{oc} of 1.271 V, J_{sc} of 17.8 mAcm^{-2}, and a FF of 68%. It is worth noting that the V_{oc} exhibited by the semi-transparent perovskite cell is the highest open circuit voltage for large area (> 1cm^2) semi-transparent perovskite solar cells ever reported (Appendix C). This achivement can be ascribed to the excellent passivation property of the two-dimensional perovskite formed by n-dodecylammonium bromide used in this work. An Si cell with an initial PCE of 21.8%, J_{sc} of 38.7 mAcm^{-2}, and V_{oc} of 0.699 V, presents a PCE of 10.1%, J_{sc} of 18.8 mAcm^{-2}, and V_{oc} of 0.675 V when measured under the perovskite cell. When the perovskite and Si cells were series-connected in 2-T tandem configuration, the tandem cell achieves a V_{oc} of 1.92 V, a J_{sc} of 17.6 mAcm^{-2} and a FF of 72.5%, corresponding to a PCE of 24.3% , when measured through a 1 cm × 1 cm aperture mask.

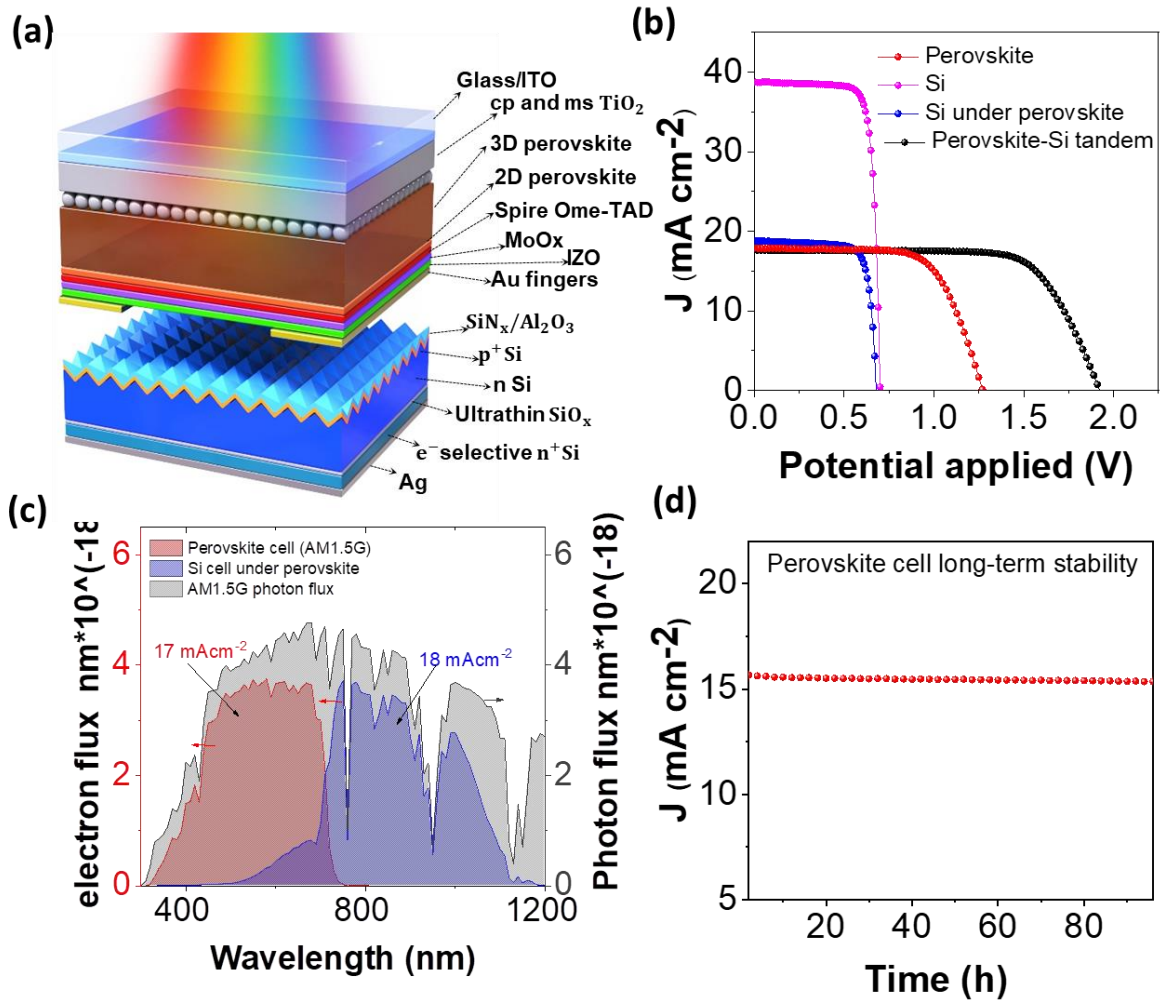

Figure 6.3: Photovoltaic performance of perovskite and Si cells. (a) Schematic illustration of the device architecture of series-connected perovskite-Si tandem cell. (b) J-V curves of the individual perovskite and Si solar cells and the series-connected tandem cell under AM1.5G illumination. (c) AM1.5G photon flux spectrum and electron flux at the top perovskite cell and bottom Si cell calculated from the EQE measurements. (d) Long-term stability of perovskite solar cell under continious AM 1.5G illumination at a fixed voltage close to the maximum power point.

The maximum obtainable electron flux values for the perovskite cell and Si cell under the perovskite cell are calculated using their respective EQE data and incident photon flux as shown in figure 6.3 (c). This translates to calculated photocurrents of 17.0 and 18.0 $mAcm^{-2}$ for the perovskite and Si cells, respectively, which match closely with the J_{sc} values obtained from J-V curves. The electron flux data shows that the two subcells possess a close current matching with little room to improve. Additionally, the perovskite cell tested in an N_2 environment shows excellcent stability up to 100 h (figure 6.3 (d)). Suitably encapsulated perovskite cells are expected to show similar stability under real world operating conditions. This result, together with the stability results of the Ni-based electrodes, verifies that the low-cost material system presented in this work can be made into a durable water splitting system.

6.5. Direct solar hydrogen generation system

We then integrate the PV and EC components in PV-EC configuration to achieve unassisted solar hydrogen generation system. **Figure 6.4** (a) illustrates the integrated water splitting sytem. The operating performance of the integrated system can be calculated by overlaying the J-V curve of the series connected perovskite-Si tandem cell with the LSV curve of the two-electrode catalyst system as shown in figure 6.4 (b). The intersection point indicates an operating current density (J_{op}) of 16.27 $mAcm^{-2}$ for solar-driven water splitting. The STH conversion efficiency of the integrated system is calculated using equation (2.22) Chapter 2. The integrated system achieves a remarkable STH efficiency of 20% for unassisted solar water splitting.

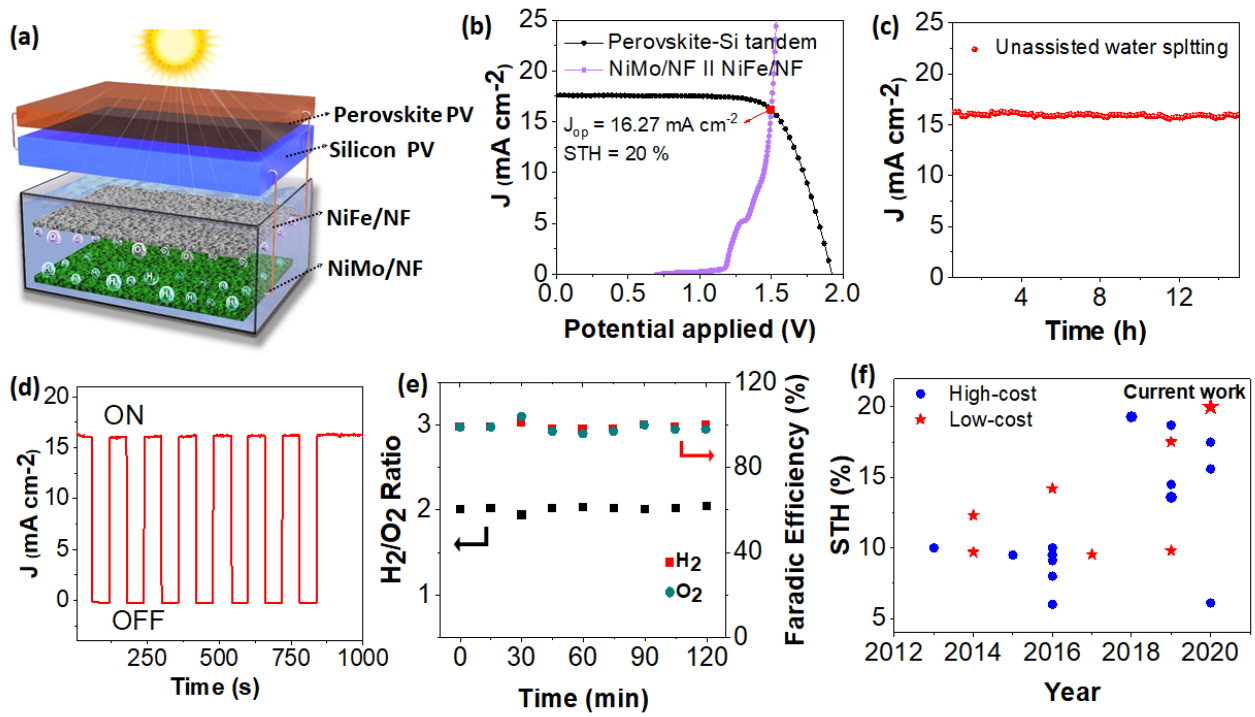

Figure 6.4: Direct water splitting using perovskite-Si PV integrated electrocatalyst system. (a) Schematic illustration of the direct solar water splitting system consisting of perovskite-Si tandem cell integrated with NiFe/NF||NiMo/NF electrodes. (b) Overlay of the J-V curve of perovskite-Si tandem cell (1 cm × 1 cm) with the LSV curve of NiMo and NiFe electrodes (1 cm × 2 cm) in two-electrode configuration. (c) Unassisted water splitting current generated by the integrated system under continuous AM1.5G illumination with the tandem PV placed in N_2 environment. (d) The light response of the integrated system under chopped AM1.5G illumination. (e) Faradic efficiency and H_2:O_2 gas ratio measurements (f) Comparision of the STH efficiency achieved in this work with the reported values for other solar-driven water splitting systems under 1 sun illumination. The systems made of expesnive semiconductors and/or noble-metal catalysts are categorized as high-cost systems as summarized in Table S6.1, in section 6.9 supplementary information.

Furthermore, the integrated system shows excellent stability with no noticeable degradation after 15 h of continuous operation under AM1.5G illumination (figure 6.4 (c)). The current fluctuation observed during the long operation is attributed to bubbles formation on the electrode surfaces. The integrated system assessed under chopped illumination shows a rapid photoresponse (inset of figure 6.4 (d)). Two electrode gas measurements are performed for NiMo/NiFe catalysts at the operating current density calculated in figure 6.4 (b). As shown in figure 6.4 (e) the gas measurements demonstrate more than 99% FE and H_2:O_2 gas ratio of 2:1. Within the experimental error, these results confirm that the two-electrode system is faradaic with no parasitic reactions involved. It is estimated that the efficiency and the amount of gas produced will be equal to the calculated values from the J-V curves (within the experimental error).

A systematic comparison of the STH efficiencies reported in the literature confirms the present work achieves the highest reported STH efficiency under 1 sun illumination (figure 6.4 (f) and table S6.1, section 6.9). It is noteworthy that a number of previous demonstrations relied on expensive III-V semiconductors and/or noble-metal catalysts for achieving higher STH efficiencies, while this work leverages commercially relevant tandem solar cells and earth-abundant catalyst materials. This record STH efficiency is achieved by realising significant improvements in the performance of the Ni-based catalysts and the perovskite PV cell, as well as optimising the integration of the system as a whole.

6.6. Pathways to further improve the STH efficiency

Previous studies have identified the STH efficiency as a critical parameter for reducing the levelized cost of hydrogen [17]. For this reason, potential pathways for efficiency enhancements were investigated that could lead to cost reductions.

As discussed in Chapter 5, voltage and current mismatch is one of the major loss mechanisms in a directly coupled system. We employ the loss mitigation technique of decoupling the PV system to remove the current and voltage matching requirements, following the method discussed in Chapter 5, and evaluate the improvement in the STH efficiency.

We model the solar hydrogen generation system following the method presented in Chapter 5. The three loss parameters for the Si cell - collection efficiency, $f_{c_{Si}}$, series resistance, R_s, and shunt resistance, R_{sh} - were chosen to give the best fit to the soli- state J-V measurements of the photovoltaic device as in figure. 6.3 (b). Once the Si cell parameters were chosen, $f_{c_{Top}}$ and f_{Para} were chosen to closely match the EQE profile of the perovskite cell (figure 6.3 (c)). After fixing these parameters, ERE, $R_s$and R_{sh} were chosen such that calculated IV-curves and the figures of merit of the perovskite solar cell matched as reported in figure-6.3 (b). The calculated figures of merit and loss parameters are given in Table 6.1 and 6.2 below.

Table 6.1: Calculated figures of merit for the modelled photovoltaic components

Figures of Merit	Si	Perovskite
Bandgap (eV)	1.1	1.72

Jsc (mA/cm^2)	18.8	17.6
Voc (V)	0.68	1.2
FF (%)	84	68
Single cell efficiency (%)	10.8	15
Tandem efficiency (%)	24.3	

Table 6.2: Parameters for modelling reported PV and photocathode components

Parameters	**Si**	**Perovskite**
External Radiative efficiency factor (ERE)	-	5.7e-4
Normalized series resistance r_s	0.8e-1	2.5e-1
Normalized Shunt resistance r_{sh}	6e3	2e4
Collection efficiency f_c	0.972	0.787
Parasitic absorption factor, f_{para}	-	0.15
Recombination current, j_0	7.2e-11	-

Catalytic exchange current density values were chosen to best fit to the experimental data and obtain the reported solar to hydrogen conversion efficiency for perovskite-Si 2-T tandem PV and NiMo/NiFe catalysts reported in the current work. Table 6.3 summarizes the parameters used to model the catalyst system.

Table 6.3: Parameters for modelling reported catalyst components

Parameters	Ideal catalyst
Exchange current density of anode J_{O_a} ($mAcm^{-2}$)	3e-1
Exchange current density of cathode J_{O_c} ($mAcm^{-2}$)	2e-0
STH efficiency at Perovskite bandgap of 1.72 eV (%)	20

Figure 6.5 shows the STH (star) and PCE (circle) comparison for a coupled (blue) and a decoupled (red) system. The coupled system represents the developed system with STH efficiency of 20%, and 2-T PV efficiency of 24.3%. As discussed in Chapter 4, in a *fully decoupled* configuration, the two PV components are separately connected independently to the PMU (known as a four-terminal (4-T) configuration). Decoupling the PV and EC components results in the predicted STH efficiency of 23% and PCE of 26% respectively, without any material improvements.

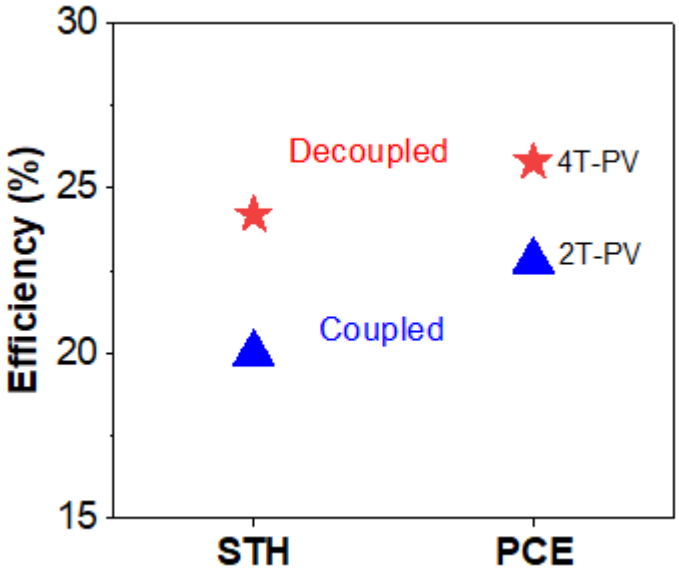

Figure 6.5: Comparison of STH (star) and PCE (circle) for a coupled (blue) and decoupled (red) system.

Another approach was to investigate the improvement in the STH efficiency as a function of improvement in the performance parameters. The current record for perovskite/Si tandem cell PCE is 29.0%, which significantly surpasses the single junction Si solar cell record efficiency of 26.7% [126, 193], yet it represents only 64% of the detailed balance efficiency limit for such tandems[21]. With Si solar cell efficiencies nearing practically achievable efficiency limits, there is a greater chance of improving the tandem PV and STH efficiencies by improving the perovskite cell efficiency. Therefore, we examined realistic improvements in perovskite solar cell performance, estimated from analysis of experimental demonstrations and theoretical projections [194, 195]. Losses are included as a function of various loss parameters; parasitic absorption (A_{para}), optical losses (collection efficiency, f_{cTOP}), series resistance (R_s) and external radiative efficiency (ERE).

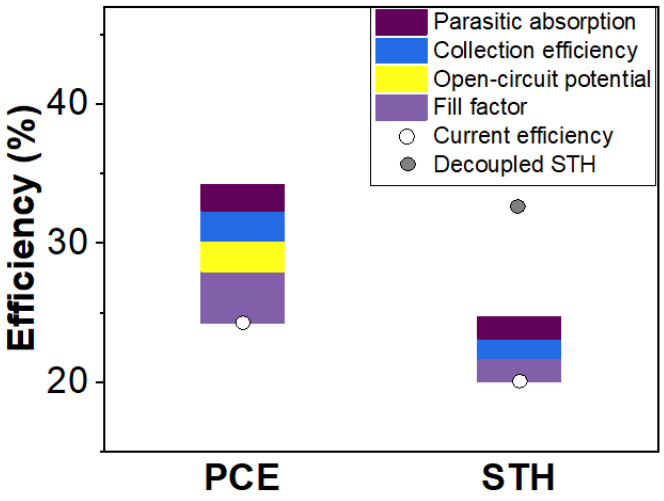

Figure 6.6: Efficiency and cost analysis of the integrated water splitting system. Realistically achievable STH conversion efficiencies by improving the perovskite solar cell as a function of parasitic absorption (A_{para}), collection efficiency (f_{cTOP}), series resistance (R_s) and external radiative efficiency (ERE).

Figure 6.6 shows the improvement in the PCE and STH efficiency for the direct solar hydrogen system, with improvement in perovskite cell performance. Currently, the performance of perovskite solar cells is limited by low fill factor due to high R_S [196]. Reducing the series resistance strongly changes the slope of the current−voltage characteristic close to the open-circuit voltage and MPP region, improving the STH efficiency of DSHG system. Series resistance in perovskite solar cells can be optimised by better charge management [197]. Different approaches such as optimising the metal finger contacts [194], electron and hole transport layers [198, 199] have been proposed in literature to improve the fill factor. Here we show that reducing the R_S close to absolute 0 (here 0.07)-$\Omega\ cm^2$[194] improves the FF to 85% , leading to an absolute increase of 3.7% in the PCE and 1.7% in STH efficiency.

Improvement in the V_{oc} of perovskite cells with a given bandgap occurs primarily by reducing recombination. Recent reports of large V_{oc} for high bandgap perovskite cells suggests that improvements in V_{oc} of up to 1 V is realistically possible for semi-transparent cells [200-202]. Increasing the V_{oc} would result in considerable improvement in the PCE of 2.2% percentage points, but it does not further improve the STH efficiency due to a fixed voltage requirement for water splitting.

Optical losses and A_{para} in the perovskite cells are crucial factors influencing the 2-T tandem PV efficiency[203]. Realistic improvement in the optical performance of the perovskite solar cells is difficult to predict, but the learning curve of Si and GaAs cells [126, 204], and recent improvements in perovskite solar cells suggest that absorption above 95% could be achieved, while minimising A_{para} Targeted optical losses in the perovskite solar cell can be reduced by better photon management [52], such as moth eye texturing, which can improve the absorption to close to unity [205]. Our model indicts that improving the incoming irradiation f_{cTOP} to 95% increases the PCE by 2.2% and the STH by 1.5% absolute.

Absorption by contacts and material layers contribute to parasitic absorption in the top cell, reducing the irradiation reaching the bottom Si cell. High transparency and low resistivity novel contacting techniques such as silver nanowires, graphene, and wire-metal-oxide hybrids, demonstrates that the A_{para} can be reduced to around 5% [52]. This results in improvement of the current densities of the individual cells and hence the tandem PV, increasing the PCE by 1.9%, and thus further improving the STH efficiency by 1.6% percentage points.

Cumulatively, optimizing the top perovskite cell could realistically improve the 2-T perovskite Si tandem solar cell efficiency to 35%, consistent with the previous reports [194]. This results in a realistically achievable STH efficiency close to 25%, based on the Si cell and catalytic system presented in this work. Employing loss mitigation technique of decoupling the system can further improve the STH efficiency to 32% as shown by grey dot in figure 6.6. Given the trajectory of perovskite cell PCE improvements over the past few years, our analysis suggests that direct solar hydrogen systems based on perovskite-Si tandems have the potential to achieve the US DOE target of 25% STH by 2025.

6.7. Technoeconomic analysis of direct solar hydrogen generation system

The LCOH is calculated for a hydrogen plant consisting of a DSHG system or a solar module plus electrolyser system, and including additional plant as needed, known as BoS. The systems are designed for a production rate of 10 tons H_2/day for a plant lifetime of 20 years and solar capacity factor of 20%. The total costs of the systems were estimated using the methods and assumptions for component costs from recent works on similar systems.[17, 206]

The LCOH of our DSHG is calculated and compared with an off-grid electrolyser (OGE) systems powered by either commercial Si modules (c-Si) or the perovskite-Si tandem cells presented in this work (P/Si). The DSHG system for hydrogen production is designed using a perovskite-Si tandem module integrated with a Ni-based electrocatalytic cell, using a polypropylene chassis at the rear to house the electrocatalysts. A semi-impermeable membrane is considered to be in between the electrodes to separate the gases.

Hard BoS costs include the balance of physical system components. The costs for the water delivery, gas collection and compressor systems are defined the same way as in ref [206]. For the OGE system, an electrolyser efficiency of 61% is assumed. For both the systems, the lifetime of the catalysts and membranes are assumed to be of 7 years and the reductions in replacement costs were assumed to be 75% and 60% of the initial cost after 7 and 14 years, respectively.[206] The tandem PV module is assumed to last 20 years.

Soft BoS costs include system installation and engineering costs and are assumed to be 20% and 5% of the module and hard BOS cost. Contingency cost is assumed to be 20% of the module and hard BOS cost.

Baseline assumptions for the techno-economic analysis are summarized in the table Table 6.4 below and details of individual components considered for the three systems in section 6.9.

Table 6.4: Operating and financial parameters

Parameter	Value
Hydrogen production rate (H_2/day)	10,000 Kg/day
Plant lifetime (n)	20 years
Solar capacity ($S_{capacity\ factor}$)	20%
Discount rate (r)	12%
$ basis year	2017
Average solar irradiation	1000 Wm^{-2}
Construction period	1 year
Catalyst and Membrane lifetime	7 years

Total plant area, A_{plant} and levelized cost of hydrogen, LCOH are calculated using the formulas below. For a given amount of hydrogen, area of the plant, A_{plant}, can be calculated as

$$A_{plant} = \frac{H_2/day \times \mathrm{U}}{1000 \times \eta_{\mathrm{STH}} \times 3600 \times S_{capacity\ factor}} \quad (6.1)$$

where, $U = 1.2\text{x}10^8 \left(\frac{\text{J}}{\text{Kg}H_2}\right)$, is the energy density of hydrogen. As evident from the formula, A_{plant} depends upon the STH efficiency and plant area reduces with improvement in STH efficiency, for a defined hydrogen production requirement. The capital, operations, and maintenance cost of the plant (that includes modules, hard and soft BoS) depend upon the plant area. Table 6.5 below summarises the STH efficiency, plant area and capital cost used for LCOH calculation for all three systems.

Table 6.5: System specifications and STH efficiency calculation

	DSHG	**OGE with 2-T PV tandem**	**OGE with commercial Si**
PV efficiency	24.3 %	24.3 %	18 %
Electrolyser efficiency	NA	61 %	61 %
STH Efficiency	20 %	14.82 %	10.9 %
Plant area (for 10 t H_2/day)	3.7e+5 m^2	5.5e+5 m^2	6.74e+5 m^2

The levelized cost of hydrogen (LCOH) is the ratio of the sum of the discounted capital and maintenance costs over the amount of total hydrogen produced over a lifetime and is given by equation 1.1, Chapter 1, and restated below

$$\text{LCOH} = \text{Capital cost} + \frac{\sum_{t=0}^{n} \frac{\text{O\&M}}{(1+r)^t}}{\sum_{t=0}^{n} \frac{\text{H}_2 \text{ production}}{(1+r)^t}} \quad (6.2)$$

where, n is the plant lifetime, O&M is the operations and maintenance cost, r is the discount rate and t is the time in years.

Figure 6.7 (a) shows a comparison of the LCOH and cost breakdown for all the three cases. The LCOH for the DSHG system is calculated to be $4.1/Kg. For the OGE system using commercial Si module with 18% efficiency and electrolyser with 61% efficiency results in LCOH of $7.4/Kg. Replacing the Si modules with high efficiency tandem PV reported in this work with PCE = 24.3% and additional invertor/power management efficiency of 90%, the LCOH can be reduced to $6.6/Kg.

Figure 6.7 (b) shows the LCOH as a function of the STH efficiency, assuming all component costs remain the same, and demonstrates that increasing the STH efficiency of the current system to 25% can reduce the LCOH to $3.3/Kg. This implies that realistic improvements in the perovskite cell alone could provide a pathway to significantly reduce the LCOH in the future.

Finally, we consider the effect of the cost of different components in the integrated system on the estimated LCOH for STH efficiency 20% and 25%. The tandem PV panel and membrane costs represent significant fractions of 23% and 17% of the overall costs, respectively. Perovskite-Si tandems are not yet commercially available, and there is significant uncertainty about the lower limit of tandem module costs once production moves down the learning curve [54]. The lower limit of the cost of perovskite-Si tandems is taken to be equal to the cost of a standard silicon module, while the upper limit is assumed to be 40% higher. Further, membrane cost is estimated based on current production values. Following the learning curve of other

technologies, membrane cost is expected to decrease significantly when produced on large-scale.

Figure 6.7 (c) shows the impact of the costs of the tandem PV module and membrane on the LCOH, assuming an STH efficiency of 20%. This shows that LCOH below \$3/Kg can be achieved for membrane cost of \$15/m^2 and tandem PV module costs of \$49.9/m^2, equal to current Si module cost. Combing the projected efficiency enhancements with the projected cost reductions discussed above, the LCOH reduces to \$2.3/Kg (figure 6.7(d)).

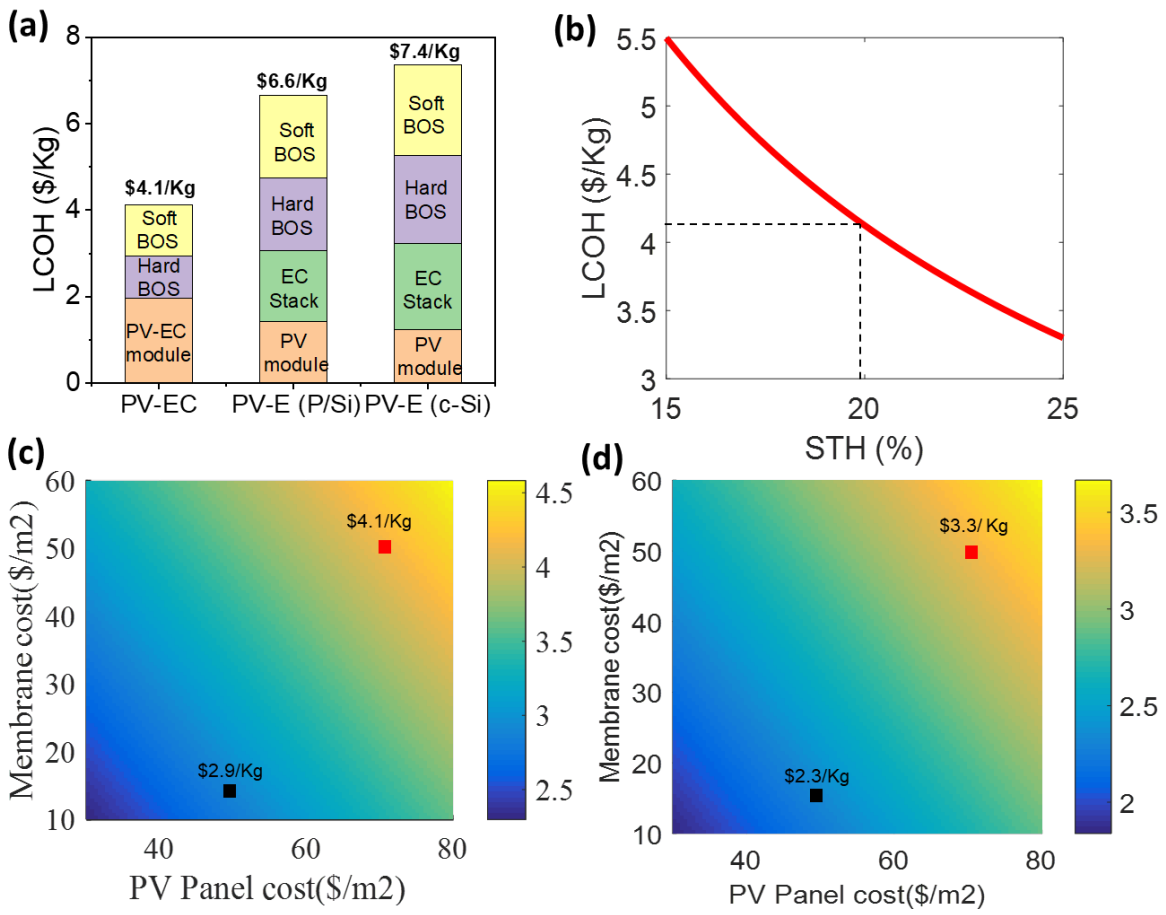

Figure 6.7: Technoeconomic analysis (a) Comparison of LCOH for direct solar to hydrogen (DSHG) and off-grid electrolyser (OGE) systems. Costs are broken down into module cost, hard BOS (balance-of-system) and soft BOS. (b) LCOH as a function of STH efficiency for the current DSHG system for the same component costs. Contour plot of the LCOH for the DSHG system as a function of PV module and electrocatalyst costs for an STH efficiency of (c) 20% (d) 25%. The red square shows the LCOH estimated for the DSHG system with current costs, while the black square shows LCOH with reduced costs for the membrane and PV tandem.

Direct solar water splitting is a developing technology and there is no data on long term costs and operation of such systems, hence there will likely be variations from the current assumptions. Nevertheless, our calculations show promising LCOH projections, assuming that improvements in the performance of low-cost solar hydrogen systems continue to occur, and realistic cost reductions in components are achieved as the manufacturing expands. In summary, the current system achieves a substantial efficiency milestone based on low-cost materials and demonstrates potential to accomplish an STH efficiency close to 25%, desired operational stability, and competitive LCOH, thereby promising its large-scale application.

6.8. Conclusion

High efficiency direct solar water splitting systems made of low-cost light-absorbers and catalysts are a promising pathway to enable commercialisation of solar hydrogen technologies. We have demonstrated a direct solar water splitting system with 20% STH efficiency by coupling earth abundant electrodes with high-performance perovskite-Si tandem cells,

fulfilling the STH efficiency target set by the DOE for the year 2020. To achieve this, we have developed NiMo electrodes with a high density of NiMo active sites in a flower-stem morphology, exhibiting an exceptional HER performance, and an improved perovskite top cell with a record open circuit voltage achieved using n-dodecylammonium bromide. In addition, we have assessed the potential for further improvement in STH efficiency and cost competitiveness of solar hydrogen production using the reported low-cost material system. Our analysis shows that an LCOH of $4.1/Kg can be achieved with current cost estimates based on an STH efficiency of 20%. Decoupling the current system can improve the STH efficiency to 23% without any material improvement. Improving solely the perovskite cell could enhance the STH efficiency close to 25%. Combined with future reductions in the PV panel and membrane costs, an LCOH of $2.3/Kg could be achieved, presenting a remarkable opportunity to realise cheap renewable hydrogen.

6.9. Supplementary Information

Table S 6.1: Comparison of STH efficiency of reported water splitting systems.

Year	Semiconductor	Catalyst Cathode/anode	STH %	Integration type	Ref
2015	GaAs/GaInP	Ni/Ni	9.5	PEC	[207]
2016	GaAs/GaInP	Ni/CoP	10	PEC	[208]
2018	GaAs/GaInAs/GaInP	Rh/RuOx	19.3	PEC	[209]
2019	GaAs/QW/GaInP	PtRu/IrO_x	13.6	PEC	[210]
2020	GaAs/GaInAsP/	MoS_2/RuO_2	6.1	PEC	[211]
2014	4 Si PV	NiMoZn/NiB	9.7	PV-E	[212]
2016	a-Si:H/a-Si:H/uC-Si:H	Pt/RuO_2	9.5	PEC	[158]
2016	a-Si:H/μc-Si:H/c-Si	Pt/ZnO:Co	9.1	PEC	[159]
2016	3 Si IBC cells	Pt/RuO_2	8	PV-E	[213]
2016	3 heterojunction Si	Micro structured Ni	14.2	PV-E	[214]
2017	4 heterojunction Si PV	Inverse opal NiFe	9.54	PV-E	[215]
2019	2 Si PV + Si PC + Si PA	NiMo/Ni	9.8	PV-PEC	[157]
2020	3 IBC/Pt	Pt/Ni	15.6	PEC	[216]
2019	3 Si IBC	Pt/RuO_2	14.5	PV-E	[217]
2013	CuInGaSe	Pt	10	PV-E	[218]
2014	Perovskite	NiFe LDH	12.3	PV-E	[219]
2016	Triple junction polymer cell	NiMoZn/RuO_2	6	PV-E	[220]
2020	Perovskite-Si tandem	Pt/IrRu	17.5	PV-PEC	[64]

2019	Perovskite-Si tandem	NiMo/NiFe	17.52	PV-E	[221]
2019	Perovskite-Si tandem	TiC-Pt/NiFe LDH	18.7	PV-E	[222]
2020	**Perovskite-Si tandem**	**NiMo/NiFe**	**20**	**PV-E**	**This work**

PC: Photoanode; PA: Photocathode; PEC: photoelectrochemical; PV-E: Photovoltaic-electrolysis; PV-PEC: Photovoltaic-photoelectrochemical.

Technoeconomic Analysis

Table S 6.2: Detailed summary of overall costs for DSHG system.

	Sub part	**Value ($\$m^{-2}$)**
PV module and hard BOS	PV panel- Si	49.95
Assumed 40% of Si	PV panel- perovskite	19.98
	Mounting material (PV and catalyst electrodes)	15.27
	Wiring (PV and EC components)	1.21
Electrocatalyst stack	Cathode – NiMo	0.5
	Anode – Ni	0.5
	Membrane	50
	Chassis (polypropylene)- for EC stack	25
Hard BOS for EC	Water pump	0.003
	Water piping	2.45
	Gas compressor	17.73
	Condenser	0.39
	Intercoolers	0.85
	Gas piping	2.45
	Water level controllers	3.14
	Hydrogen sensors	3.34
	Other control equipment	0.34

Soft BOS	DSHG installation	20 % of module and hard BOS
	DSHG contingency	20 % of direct costs
	DSHG engineering	5 % of module and hard BOS

Table S 6.3: Detailed summary of overall costs for OGE system

	Sub part	Value ($\$m^{-2}$)
PV module and hard BOS	PV panel Si	49.95
	PV panel Perovskite	19.98
	Mounting material	13.32
	Wiring	14.99
Electrolyser	Electrolyzer stack	54.97
and hard BOS	Hard BOS	54.64
	Total	106.60
OGE soft BOS	PV installation	15.65
	PV contingency	15.65
	PV engineering	3.91
	Installation stacks electrolyser	20% of electrolyser stack
	Installation hard BOS electrolyser	20% of hard BOS
	Contingency electrolyser	20% (elec + Hard BOS)
	Engineering and design	5% OF (elec + hard BOS)
	electrolyser	
	Other soft BOS	5 %

Chapter 7

Summary and Future Work

This thesis aimed to develop low-cost and high-efficiency DSHG generation based on perovskite-silicon PV tandems and earth abundant catalysts. Perovskite-Si tandems have recently emerged as a potentially low-cost and high-efficiency alternative to III-V semiconductors. With current PCE records of close to 30% for perovskite-Si tandems, and the potential to reach up to 35%, they are promising candidates for solar hydrogen generation.

Firstly, we demonstrated a PEC system based on all-low-cost materials, with Si photocathodes integrated with novel earth abundant catalysts, and a perovskite PV cell in 2-T tandem PV-PEC configuration. High-performance Si photocathodes were developed by incorporating state of the art charge selective passivation and earth abundant catalysts, demonstrating an ABPE of over 10%. Binary metal NiMo HER catalysts with Ni interlayers were deposited using magnetron co-sputtering, exhibiting non-conformal nanorod morphology. The nanorod morphology of NiMo/Ni allows concentrated porosity in perpendicular direction to the substrate, supporting effective transport of reactants to the catalyst sites. The HER catalysts showed low overpotentials of 89 mV at 10 $\mathrm{mAcm^{-2}}$ on planer substrates.

We separate the requirements of protection and passivation, by employing a $\mathrm{SiO_X/n^+}$ poly-Si state-of-the-art charge selective passivation layer, combined with a continuous thick metal catalyst layer on the rear of the photocathode to provide protection against corrosion in the electrolyte. The $\mathrm{SiO_X/n^+}$ poly-Si charge selective passivation layer improves the silicon

photocathode ABPE to 10.5%, compared to 6.2% without any passivation. This translates to a 70% relative improvement in the performance due to passivation, highlighting importance of the efficiency loss due to recombination at the Si/catalyst interface.

Unassisted water splitting with STH efficiency of 17% was achieved by combining the Si photocathode with a high bandgap top perovskite cell, and a NiFe OER anode in PV-PEC configuration. This efficiency is closely comparable to 17.6% achieved using noble metal catalysts. Additionally, this work leverages the existing advances in Si technology in terms of photocathode design and passivation. The hydrogen evolution reaction catalysts integrated on Si photocathode are fabricated using industrially relevant methods and can be easily integrated into current Si manufacturing.

Secondly, we developed a new theoretical framework to identify the performance limitations and conceptualise practical device designs to improve the STH efficiency towards 20%. Such models are invaluable to quantify and compare different loss mechanisms in PV-based solar hydrogen generation systems and evaluate the potential of different loss mitigation techniques to improve the solar to hydrogen generation efficiency. Our analysis showed that the two largest losses in the system are due to energy being lost as heat in the PV component, and current and voltage matching requirements between the PV components and the water-splitting reaction imposed by sub-optimal connection strategies. We considered two different ways in which these losses could be mitigated: decoupling the PV system from the reaction through a power management unit, and thermal integration to use the heat losses to increase the electrolyte temperature and improve the reaction dynamics for water-splitting.

To assess the potential of different loss mitigation techniques to increase practically achievable STH efficiencies, we developed a temperature dependent model of realistic solar hydrogen generation systems, taking into account the non-ideal behaviour and unavoidable material dependent losses. For series-connected perovskite-Si tandem PV systems coupled with nickel-based earth-abundant catalysts, thermal integration can increase the STH efficiency from 10.9% to 13.4% at realistic operating temperatures, translating to a 23% relative improvement in the efficiency upon thermal integration. However, decoupling the same system in the absence of thermal integration increases the STH efficiency to 20.0% at room temperature and 17.9% at realistic operating temperatures, resulting in a relative improvement of 16% at room temperature and 64% at higher operating temperature relative to the coupled system. Combining the two loss mitigation techniques shows maximum improvement at realistic operating temperatures, increasing the STH to 19.4% for a thermally integrated decoupled system, translating to an improvement of 78% compared to non-thermally integrated coupled system. These results show that optimal system configuration strategies provide more than three times the STH efficiency increase of thermal integration at high operating temperatures. These results demonstrate that the two loss mitigation techniques result in significantly different performance enhancements. Is it possible to achieve close to 20% STH efficiency at realistic operating temperatures with existing systems, without further improvement in the separate components.

Finally, we report an unprecedented STH efficiency of 20% by DSHG using an all-low-cost material system. We modified the solar hydrogen generation system design from our initial work by physically separating the PV and EC components in a PV-EC configuration. This design eases the catalyst fabrication requirements. Physically separating the PV and EC also

allows for better voltage and current matching, as we are not restricted to size match both the components. Unassisted water splitting is achieved by high performance perovskite-Si PV tandem coupled with Ni based Earth abundant catalysts.

To achieve this, we developed NiMo HER electrodes with a 'flower-stem' morphology. The as synthesized HER catalysts exhibited a low overpotential of 6 mV @ 10 $\mathrm{mAcm^{-2}}$ with stable performance of over 100 hours, outperforming noble metal catalysts. This is one of the best performing earth abundant HER catalysts reported in literature in an alkaline medium. On coupling with a NiFe OER electrode the system achieves high performance of 10 $\mathrm{mAcm^{-2}}$ @ 1.48V and a remarkable stability of over 100 h for overall water splitting.

We develop an optimized bandgap (1.72 eV) quadruple perovskite solar cell with a high V_{oc} of 1.271 V. This is the highest reported V_{oc} for large area (> $1\mathrm{cm^2}$), wide bandgap semi-transparent perovskite cells ever reported. PCE of 24.3% is achieved when paired with a monocrystalline n-Si cell in a series-connected 2-T tandem configuration.

Upon combining the tandem PV and electrocatalyst electrodes, the integrated system achieves a record STH efficiency of 20% with low-cost materials. This is the highest reported STH efficiency under 1 sun illumination, also achieving the US-DOE target for 2020 for photoelectrochemical hydrogen generation.

Further analysis of realistic efficiency improvements reveals that employing the loss mitigation technique of decoupling, proposed in Chapter 5, improves the STH efficiency of the DSHG system to 23% without any improvements in the individual components. Further optimising

the perovskite cell in the coupled system has the potential to improve the STH efficiency close to 25%, and 35% when decoupled. Given the trajectory of improvements in the perovskite cell performance over the past few years, DSHG system based on perovskite-Si tandem has the potential to achieve the US DOE target of 25% STH efficiency by 2025.

We performed technoeconomic analysis (TEA) to assess the potential of developed DSHG system for large scale implementation. Technoeconomic analysis calculations reveals LCOH of $4.1/Kg can be achieved for the current system. We show that LCOH is sensitive to efficiency and improving the STH efficiency of the current system to 25% alone can reduce the LCOH to $3.3/Kg. This implies that realistic improvements in the perovskite cell alone could provide a pathway to significantly reduce the LCOH in the future. Combing the projected efficiency enhancements with the proposed cost reductions can reduce the LCOH to ~$2/Kg. These results make it a cost-competitive approach to fossil fuel-based hydrogen production with a current LCOH of ~$1.5/Kg. Our calculations show promising LCOH projections, assuming that improvements in the performance of low-cost solar hydrogen systems continue to occur, and realistic cost reductions in components are achieved as the manufacturing expands.

These results show that perovskite-silicon tandem based photoelectrochemical systems have the potential to make large scale direct solar hydrogen generation a reality by lowering the cost. This work will encourage dedicated research with a clear awareness of the improvements in components and system design that needs to be focused on, towards achieving the aim of low-cost, large scale solar hydrogen generation.

The future of perovskite-Si PV tandem systems for large scale solar hydrogen generation

Perovskite-Si tandems offer the opportunity to realise large-scale direct solar hydrogen generation. The results presented in this thesis are promising and reflect the progress of direct solar hydrogen generation technologies. Our analysis shows that an LCOH of $4.1/Kg can be achieved with current system and has the potential to reduce to ~$2/Kg with future reductions in component costs and realistic improvements in STH efficiency. Promising LCOH predictions make DSHG a cost-competitive technology compared to fossil fuel-based hydrogen generation. To realise commercial large-scale direct solar hydrogen generation, it is essential to further improve the STH efficiency and simultaneously assess the feasibility and limitations of the current system.

Improving the perovskite cell performance can increase the STH efficiency towards 25%, simultaneously playing an important role in reducing the levelized cost of hydrogen. Our analysis in Chapter 6, shows that it is important to optimise the tandem PV based on the catalytic system water splitting potential requirements to achieve high STH efficiency.

Dedicated efforts to design PV tandems for direct solar hydrogen generation are required to improve the STH efficiency. In Chapter 6 we show that the most critical factors to improve in the perovskite solar cells for water splitting are fill factor and reduction in parasitic absorption and optical losses. This will improve the tandem PV and STH efficiency towards 25%. Learning from the improvements in the lower bandgap perovskite cells efforts are required in reducing the series resistance of high bandgap semi-transparent perovskite cells. Targeted optical losses can be reduced by better photon management, such as moth eye texturing which

can improve the absorption close to unity. Parasitic absorption can be reduced by developing high transparency and low resistivity contacting techniques.

Further efforts are required to evaluate the potential of the loss mitigation techniques discussed in the thesis. This will include experimental validation of power management unit (PMUs) using dc/dc convertors, and thermal integration techniques. It is important to verify the relative improvements in the efficiency and corresponding complexity added to system configuration, balance of plant and hydrogen production costs on addition of different loss mitigation techniques.

For large scale implementation the overall system stability requires enormous improvements. Catalytic systems are required to be stable for years to be economically viable and dedicated efforts are required to improve the stability of catalytic systems without compromising on their electrocatalytic performance. For PV-PEC and monolithic PEC configurations, robust protection layers are required that can protect the photoelectrode from corrosion under the electrolytic environment for long term operation. Long term stability of the perovskite cells is another limitation. However, this is under active investigation by the PV community and any advancements can be directly leveraged for solar hydrogen generation.

Apart from improving the STH efficiency and stability, it is important to focus the research on the prototyping stage. Numerous practical challenges exist in scaling up the perovskite-Si tandem based PEC systems for DSHG. STH efficiency reduces rapidly on increasing the device area compared to equivalent smaller area devices [223]. This is due to added losses in the system on increasing the area. For example, the electrocatalytic performance does not improve

linearly with increase in the electrode area. Due to limited conductivity of the substrate, increase in the electrode area substantially increases the voltage losses in the system. Similar issues have been observed for perovskite cell performance as well, where increase in area introduces additional losses resulting in the reduced device efficiency [224].

PEC systems will also require gas impermeable membranes over a large area resulting in additional Ohmic overpotential losses and increased costs. These systems operate at much lower current densities and pressures compared to conventional electrolyser systems and hence the optimised membrane for PEC systems will be different to that of electrolysers. Dedicated membrane design for PEC systems is required that will allow efficient ion transport under low operating pressures, without additional ohmic overpotential losses and gas permeation across the membranes. Robust and low-cost membranes with improved stability, easy handling and maintenance are required.

In this thesis, PV-EC and PV-PEC configurations based on perovskite-Si tandem PVs are developed. It is possible to further expand to monolithic PEC configuration by directly integrating catalysts on a monolithic tandem PV. Scaling up a particular configuration for large scale DSHG will also depend upon the ease of fabrication and handling apart from its performance. Further system optimisation and modelling are required to design solar hydrogen generation modules. It is essential to optimise integration of the membrane, design of electrode dimensions, and connection strategies to minimise voltage loss in the system. Designing and modelling the prototypes, followed by experimental validation of solar to hydrogen generation performance will help in understanding the feasibility and limitations.

Though previous techno-economic analysis, including the one in Chapter 6 in this thesis show promising levelized costs of hydrogen for direct solar hydrogen generation, they are based on general assumptions in the absence of an optimal system design. It is important to extend the above-mentioned prototyping work towards detailed techno-economic analysis to assess the potential of this technology to provide low-cost renewable hydrogen at scale. This will also assist in identifying the areas for potential improvement and pathways towards further cost reductions. Dedicated research on full integrated systems should be the focus to realise large scale direct solar hydrogen generation.

Appendix

Appendix A

Table A 1: List of constants and their values

Symbol	Parameter	Value
c	Speed of light	$3 \times 10^{8}\ ms^{-1}$
h	Planck's constant	$6.63 \times 10^{-34} Js$
k	Boltzmann constant	$1.38 \times 10^{-23} JK^{-1}$
q	Electric charge	$1.6 \times 10^{-19}\ C$
Ω_{solar}	angular diameter of sun as viewed from earth	$6\ \times 10^{-5}$
T_s	Temperature of sun	$6000\ K$
T_{PV}	Temperature of PV cell	$300\ K$
E_g	Semiconductor bandgap	eV
Ω_{emit}	solid angle of emission of the PV component	π
Ω_{abs}	Angle of absorption of PV from Sun	$6\ \times 10^{-5}$
E_{STH}	Thermodynamic potential for water splitting	$1.23\ V$
η_f	Faradic efficiency	1
C_p	Specific heat capacity of water	$4.2\ Jgm^{-1}K^{-1}$
σ	Stefan-Boltzmann constant	$5.67 \times 10^{-8} Wm^{-2}K^{-4}$
R	Gas constant	$8.314\ Jmol^{-1}K^{-1}$
n	Number of electrons exchanged	2
F	Faraday's constant	$96485.3 Cmol^{-1}$

P_{H_2}	Partial pressure, Hydrogen	1
P_{O_2}	Partial pressure, Oxygen	1
P_{H_2O}	Partial pressure, Water	1
P_O	Reference pressure	1

Table A 2: List of abbreviations and acronyms

Abbreviation/acronym	Full form
2-T	Two terminal (series connected)
4-T	Four terminal
ABPE	Applied bias to photon efficiency
ALD	Atomic layer deposition
AM1.5G	Standard solar spectrum
ARC	Antireflection coating
BoP	Balance of plant
CCS	Carbon capture and storage
c-Si	Crystalline Silicon
DSHG	Direct solar hydrogen generation
EC	Electrochemical
EIS	Electrochemical impedance spectroscopy
ERE	External radiative efficiency
EQE	External quantum efficiency
FF	Fill factor
FFT	fast Fourier transform
GHG	Green-house gas
HAADF-STEM	High-angle annular dark-field scanning transmission electron microscopy
HER	Hydrogen evolution reaction

HF	Hydrogen fluoride
IRENA	International renewable energy agency
J-t	Chronoamperometry
J-V	Current density-voltage
KOH	Potassium hydroxide
LCOH	Levelized cost of hydrogen
LPCVD	Low pressure chemical vapour deposition
LSV	Linear sweep voltammetry
MIS	Metal insulator semiconductor
OER	Oxygen evolution reaction
PC	Photochemical
PCE	Power conversion efficiency
PEC	Photoelectrochemical
PECVD	Plasma enhanced chemical vapour deposition
PERC	Passivated emitter rear contact
PERL	Passivated emitter rear locally diffused
PERT	Passivated emitter rear totally diffused
PMU	Power management unit
PV	Photovoltaic
PL	Photoluminescence
Poly-Si	Polycrystalline Silicon
RCA	Radio corporation of America
R_s	Series resistance

SAED	Selective area electron diffraction
SEM	Scanning electron microscopy
SMR	Steam methane reforming
STH	Solar to hydrogen conversion
TEM	Transmission electron microscopy
TMAH	Tetramethylammonium hydroxide
TRPL	time-resolved photoluminescence
V-t	Chronopotentiometry
XPS	X-ray photoelectron spectroscopy
XRD	X-ray diffraction

Table A 3: Reagents and chemical processes

Task	Reagent	Company	Composition specifications
TMaH etching	Tetramethylammonium	JT baker	25% concentrated solution, heated to 70-75 C. Samples are cleaned in DI water and followed by HF dip and clean again
RCA- 1 Solution			DI water: Ammonia (30%) : Hydrogen peroxide (30%) In 7:1:1 by volume. Solution is heated to 50-60 ℃ and wafers are cleaned for min 10 mins
	Ammonia	Chem supply	30% concentration w/w
	Hydrogen peroxide	Chem supply	30 % concentration
RCA-2 Solution			RCA-2 cleaning is performed after RCA-1 cleaning. DI water: HCl (36%) : Hydrogen peroxide (30%) In 7:1:1 by volume.

			Solution is heated to 50-60 ℃ and wafers are cleaned for min 10 mins
	Hydrochloric acid (HCl)	RCI labscan	32% concentration
HF dip	Hydrofluoric acid (HF)		After RCA-1 and RCA-2 cleaning 1% HF (v) + 1% HCl (v) + 98% DI water (v)
HF fuming	Hydrofluoric acid (HF)	Ensure	48% (w/v)
Surface texturing			TMaH:Monotex texturing solution- 1200ml DI water + 230 ml TMaH (25% conc) + 150 ml monotex working sol. Solution is heated to ~80 ℃
	Monotex	Technisol	Monotex working sol- 17 ml monotex + 1000 ml DI water
Photo electrochemical/ Measurements	KOH electrolyte	Alfa Aesar	85% 1M solution in DI water
Photolithography	AZ 4562 photoresist	Microchemicals	
	Ti prime	Microchemicals	

Thin SiOx by chemical method	Nitric acid (HNO_3)	RCI labscan	70% concentrated nitric acid boiled to ~80 ℃ on temperature gun.
External contacts	Silver paint/soldering	RS pro	RS 186-3593
Encapsulation	Epoxy	Hysol 9460	

Table A 4: Instrument specifications

Task	Instrument	Company	Process specification
Thin SiOx masking	Furnace		666 ℃, ramp up and down
SiNx masking layer	Low pressure chemical vapour deposition (LPCVD)	CVD equipment corporation	Ammonia flow rate- 120 DCS flow rate- 30 Temp- 775 ℃
Diffusion	Tempress	594 tempress systems	Precursor for Boron doping – Boron tribromide (BBr3) Precursor for phosphorous doping- Phosphoryl chloride (PoCl3)
a-Si deposition	Plasma enhanced chemical vapour deposition PECVD	Roth and rau	Temp- 500 ℃
Al2O3	Atomic layer deposition (ALD)	Beneq	Thermal ALD Temp- 200 ℃ Dep rate~ 0.1 nm/cycle
SiNx antireflection layer	Plasma enhanced chemical vapour deposition (PECVD)	Oxford Plasmalab 100	Temp- 400 ℃

Metal fingers, busbars	Metal evaporation	Varian	Pressure- $5x10^{-5}$ torr
Ti	e-beam evaporation	Temescal BJD-2000 Ti pellet purity 99.995%,size 3x3mm	Pressure- $1x10^{-5}$ torr
Ni, NiMo	Sputter	AJA sputter systems	Pressure- $1x10^{-6}$ torr

Appendix B

The catalyst synthesis and characterisation in Chapter 6 was performed by Yuan Wang and team at the university of New South Wales. Appendix B discusses the details of catalyst fabrication and characterisation.

B.1. NiMo/NF and NiFe/NF catalyst synthesis

Materials

Ammonium molybdate tetrahydrate ($(NH_4)_6Mo_7O_{24}$ $4H_2O$, >99.98%,), nickel nitrate hexahydrate ($Ni(NO_3)_2$ $6H_2O$, >98.5%), iron nitrate nonahydrate ($Fe(NO_3)_3$ $9H_2O$, >98%) and Nafion (5 wt% in lower aliphatic alcohols and water) were purchased from Sigma-Aldrich. Formamidinium iodide, formamidinium bromide, methylammonium iodide, methylammonium bromide, *n*-BABr, *iso*-BABr, *t*-BABr, and TiO_2 paste were procured from GreatCell Solar Materials. Lead iodide was purchased from Alfa Aesar. Spiro-MeOTAD was purchased from Lum-Tech. Refractive index matching layer (series AA, refractive index = 1.414) was obtained from SPI Supplies. Other materials were purchased from Sigma-Aldrich and used as received.

Synthesis of electrocatalysts

Before use, NF substrates were cleaned sequentially in 3 M HCl solution, acetone and deionized water in an ultrasonic water bath. NiMo/NF electrodes were fabricated by a modified

hydrothermal and hydrogen reduction method. First, NF substrates (2 cm × 4 cm) were placed in a mixed aqueous solution of 0.03 M ($(NH_4)_6Mo_7O_{24}$ $4H_2O$ and 0.12 M ($Ni(NO_3)_2$ $6H_2O$ in a 25 mL Teflon-stainless steel reactor, followed by a hydrothermal reaction at 150 °C for 15 h in an oven. The obtained NF samples was cleaned by deionized water and ethanol, and dried at 70 °C for 5 h, after which they were calcined in a vacuum furnace under the flow of 10 vol% H_2 in Ar (55 ml/min) for 3 h.

NiFe/NF electrodes were fabricated by electrodeposition in a mixed aqueous solution of 3 mM $Ni(NO_3)_2$ $6H_2O$ and 3 mM $Fe(NO_3)_3$ $9H_2O$ using a three-electrode system, with saturated calomel electrode (SCE), NF and Pt plate as the reference, working and counter electrodes, respectively. The electrodeposition process was carried out at a constant potential of -1.0 V (vs. SCE) for 300 s.

To prepare Pt-C/NF and Ir-C/NF electrodes, commercially available 20% platinum on carbon (Pt/C) and 20% iridium on carbon (Ir/C) powders purchased from fuel cell store were prepared into inks by sonicating 5 mg powder with 475 µl ethanol, 500 µl distilled water and 25 µl Nafion. The uniformly mixed inks were drop casted on NF substrates and dried at room temperature to obtain Pt-C/NF and Ir-C/NF electrodes.

B.2. Characterisation of electrocatalysts

Figure B1 (a-d) shows the SEM images of NiMo/NF electrode. B1 b,c and d have been discussed in Chapter 6 figure 6.1 and have been repeated here for clarity. As discussed in Chapter 6, the NiMo/NF catalyst forms high density flower-like nanosheets and stem-like

nanowires resembling a flower-stem morphology grow uniformly on the 3D NF skeleton (figure B1 a,b). Such morphology can improve electrolyte-catalyst interaction through capillary forces and reduce the adhesion of gas phase products, thereby enhancing the reaction kinetics [189].

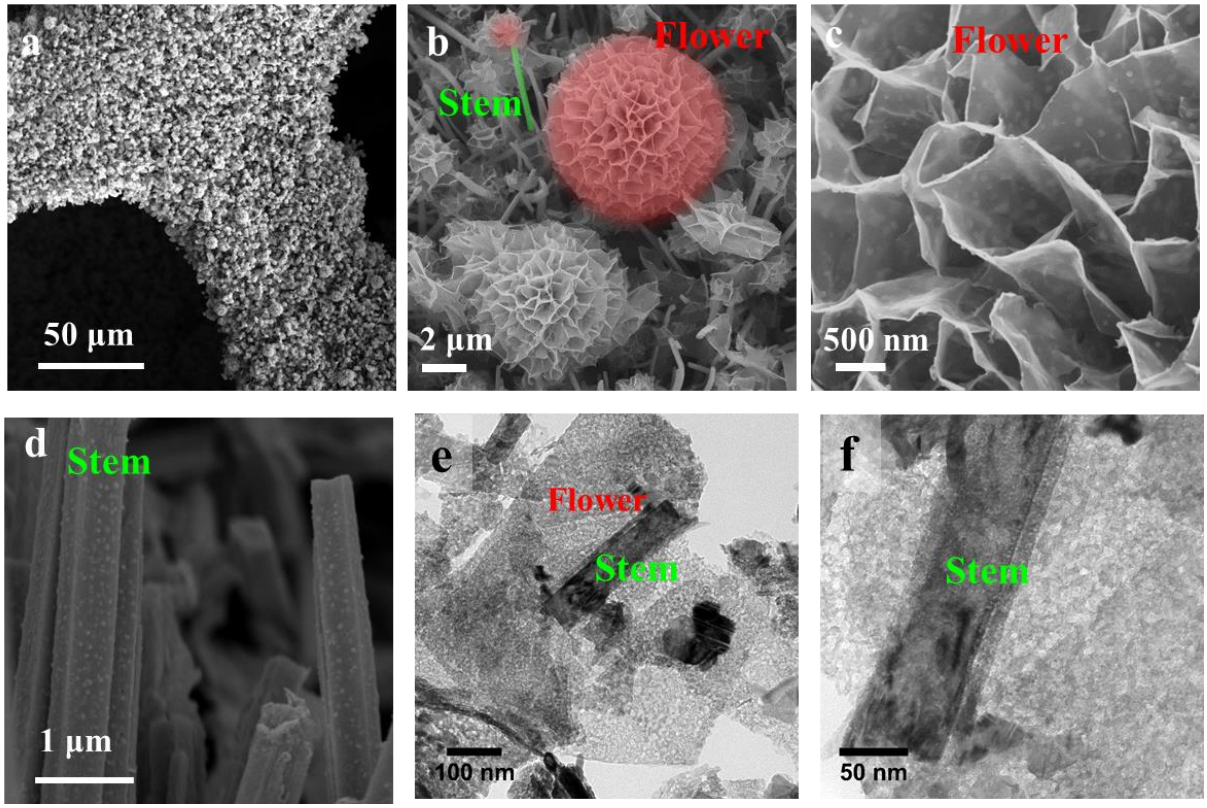

Figure B1: (a-d) Scanning electron microscopy (SEM) images of NiMo/NF. (e-f) TEM images of NiMo/NF

The flower-like nanosheets are closely connected to the surface of the Ni foam through the stem-shaped nanowires, providing significantly enhanced accessible surface area with good mass and electron transfer properties. After H_2 treatment, homogeneous nano-grains are observed on the surface of the nanosheets and nanowires (figure B1 c,d). Calcination in a

reducing environment is expected to form NiMo particles on the catalyst surface, which serve as active sites for HER [73, 141]. The transmission electron microscopy (TEM) (figure B1 (e,f) analysis confirms that both the flower-like and stem-like structures (rolled nano-sheet) are composed of hollow nanosheets.

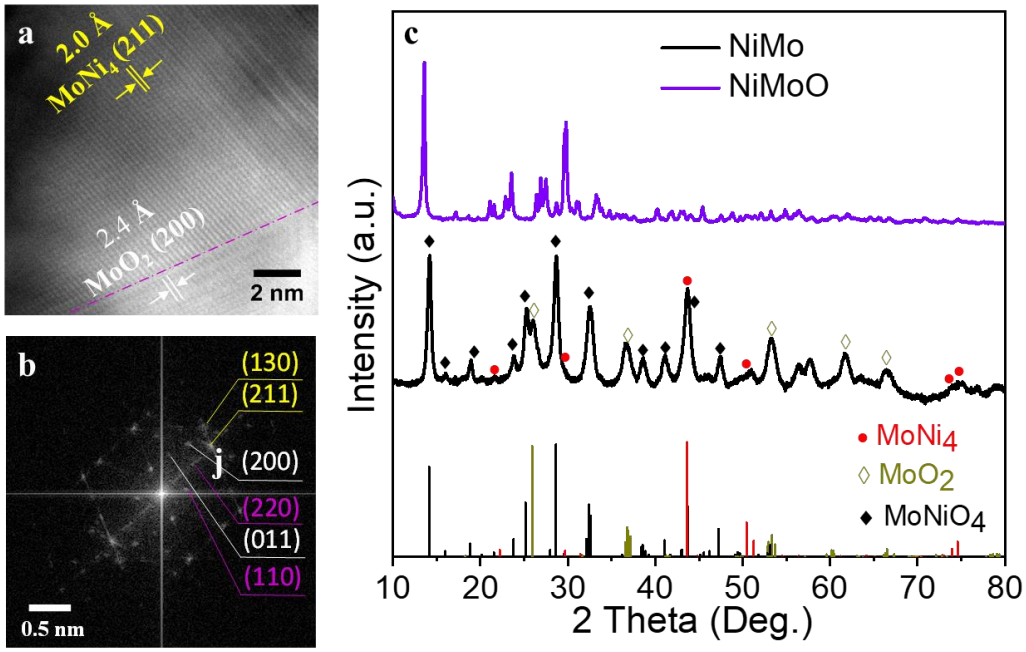

Figure B2: (a) HAADF-STEM image, (b) FFT image, where crystal facets of $MoNi_4$, MoO_2 and $NiMoO_4$ are labelled in yellow, white and purple colours, respectively (c) XRD pattern of NiMo/NF and references including $MoNi_4$ (03-065-1533), MoO_2 (01-078-1071) and $MoNiO_4$ (00-033-0948).

The interplanar spacing of the lattice fringes determined from the high-angle annular dark-field scanning transmission electron microscopy (HAADF-STEM) image (**figure B2** (a)) are 2.0 and 2.4 Å, which are assigned to the (211) plane of $MoNi_4$ and (200) plane of MoO_2,

respectively. The fast Fourier transform (FFT) pattern shown in figure B2 (b) indicates a mixed chemical composition of $MoNi_4$ ((130) and (211)), MoO_2 ((200) and (011)), and $NiMoO_4$ ((220) and (110)), which is further confirmed by the X-ray diffraction (XRD) patterns (figure B2 (c)). It can also be seen from the XRD patterns of the catalyst before and after H_2 calcination that the $MoNi_4$ phase is formed only after the reduction treatment.

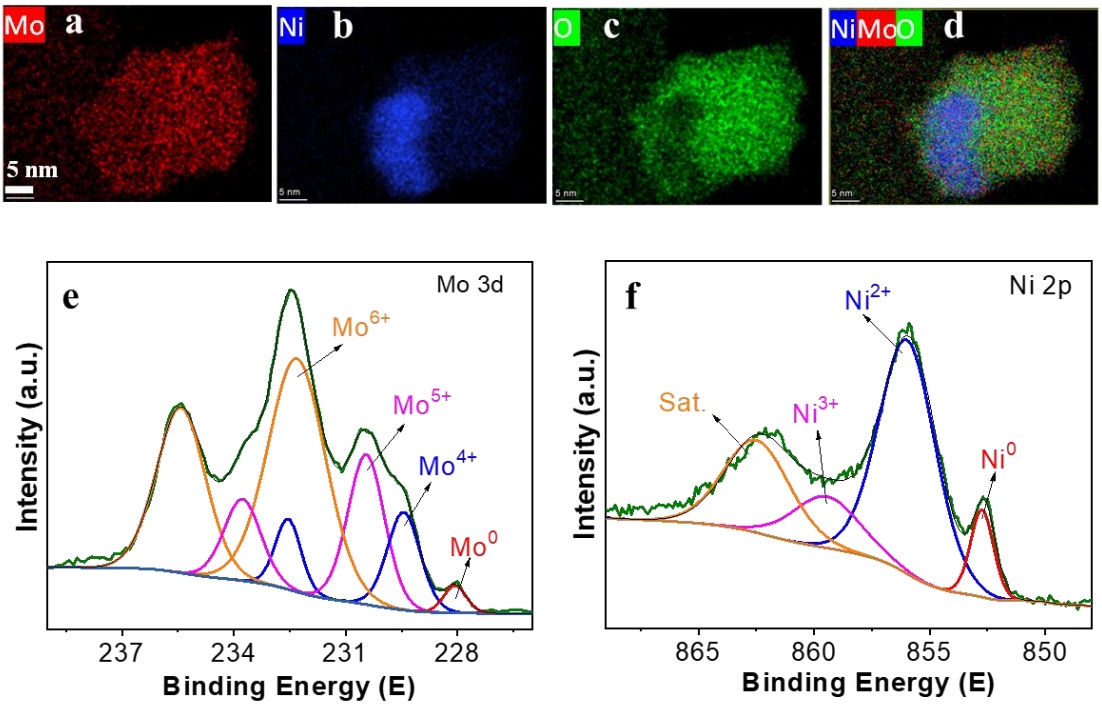

Figure B3: (a-d) EDS mapping, (e) Mo 3d XPS spectra, and (f) Ni 2p XPS spectra of NiMo/NF.

The energy-dispersive (EDS) elemental mapping in **figure B3** (a-d) confirms an even distribution of Ni, Mo, O in NiMo/NF catalyst. The surface chemical composition of the NiMo/NF was analysed by X-ray photoelectron spectroscopy (XPS). The deconvulated peaks of the Mo 3d spectrum at 228.1 eV, 229.4/232.5 eV, 230.4/233.8 eV, and 232.3/235.4 eV can

be fitted to the binding energies of Mo^0, Mo^{4+}, Mo^{5+} and Mo^{6+}, respectively (figure B3 e). Similarly, the Ni 2p spectrum of NiMo/NF deconvulated into four peaks at 852.7, 856.0, 859.5 and 862.7 eV are attributable to Ni^0, Ni^{2+}, Ni^{3+} and satellite peak, respectively (figure B3 f). These results confirm the co-existence of $MoNi_4$ alloy with various Ni-Mo oxide compounds.

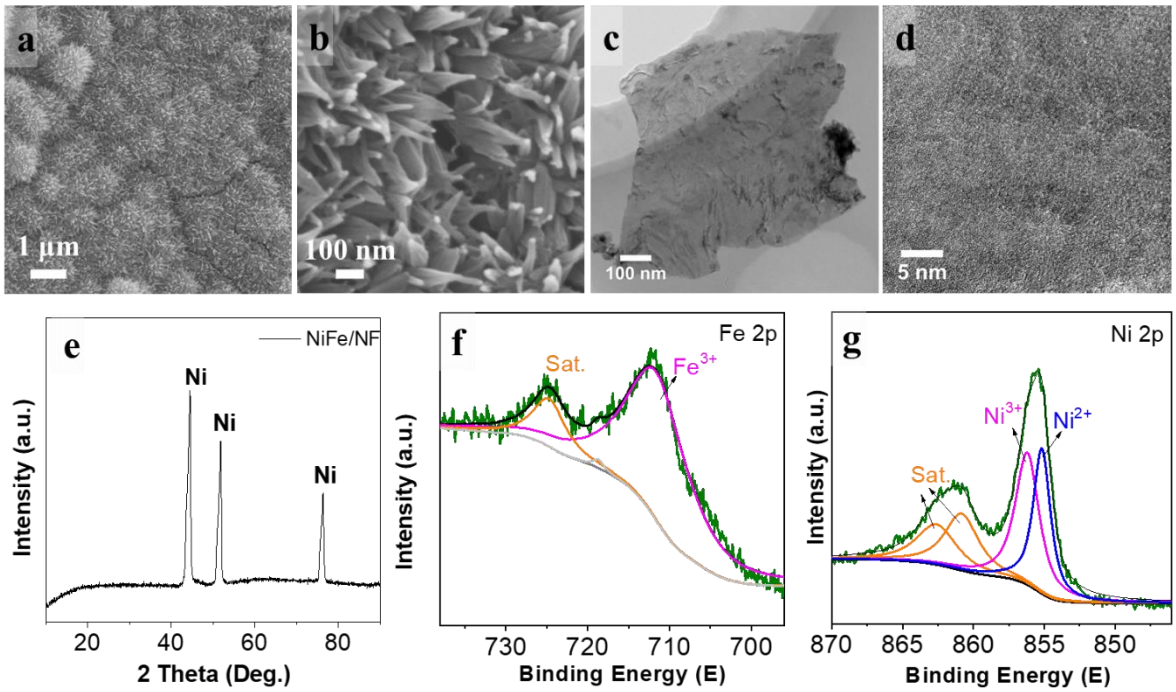

Figure B4: (e) XRD pattern of NiFe/NF (f) Fe 2p XPS spectra, and (g) Ni 2p XPS spectra of NiFe/NF.

To pair with NiMo/NF, we prepared NiFe/NF electrodes for OER using electrodeposition method, producing vertically grown Ni-Fe nano-needles completely covering the Ni foam surface (**figure B4** (a,b)). The TEM (figure B4 (c,d)) and XRD analyses (figure. B4 (e)) of NiFe/NF confirm that the NiFe catalyst consists of ultrathin amorphous nanosheets. From the

XPS analysis of NiFe/NF (figure B4 (f,g)), the Fe 2p and Ni 2p spectra show highly oxidized states (Ni^{2+}/ Ni^{3+} and Fe^{3+}), which are favourable for oxidation reactions.[186]

B.3. Evaluation of electrochemical performance for water splitting

After synthesising the electrocatalysts, we tested their electrochemical performance in 1M KOH in both three-electrode and two-electrode configurations to evaluate the individual HER and OER performances and the combined overall water splitting performance, respectively. For benchmarking purposes, we also prepared Pt-C/NF and Ir-C/NF electrodes. The LSV plots for NiMo HER, NiFe OER and NiFe/NF||NiMo/NF are already discussed in Chapter 6, figure 6.2 and are repeated here for clarity.

As discussed in Chapter 6 and shown in **figure B5** (a), the as-synthesized NiMo/NF presents an HER onset potential close to the thermodynamic potential, and low overpotentials of 6 and 70 mV to obtain the current densities of 10 and 100 $mAcm^{-2}$. In comparison, the benchmark Pt-C/NF and unmodified NF show much higher overpotentials of 130 and 270 mV at 10 and 100 $mAcm^{-2}$, respectively. The Tafel slope obtained for NiMo/NF (78 $mVdev^{-1}$) is substantially lower than that of Pt-C/NF (86 $mV\ dev^{-1}$) and NF (110 $mV\ dev^{-1}$), suggesting rapid reaction kinetics. These results confirm the surface $MoNi_4$ nano-grains formed after the reduction process supply abundant electrocatalytic active sites for HER. Moreover, the NiMo/NF electrode exhibits excellent longstanding stability, maintaining a stable HER activity at a high current density of 100 $mAcm^{-2}$ after 100 h of continuous operation (figure B5 (b)).

As shown in figure B5 (c), NiFe/NF electrode presents a low overpotential of 255 mV at 10 $mAcm^{-2}$, and small Tafel slope (30 $mV\ dec^{-1}$,) for OER, outperforming the benchmark Ir-C/NF and pristine NF. To obtain a current density of 100 $mAcm^{-2}$,, the NiFe/NF requires a low overpotential of 299 mV, which is considerably lower than the overpotential needed by Ir-C/NF and NF. The performance of NiFe/NF in the current study is comparable or superior to many other recently developed transition metal OER electrocatalysts.[225, 226]

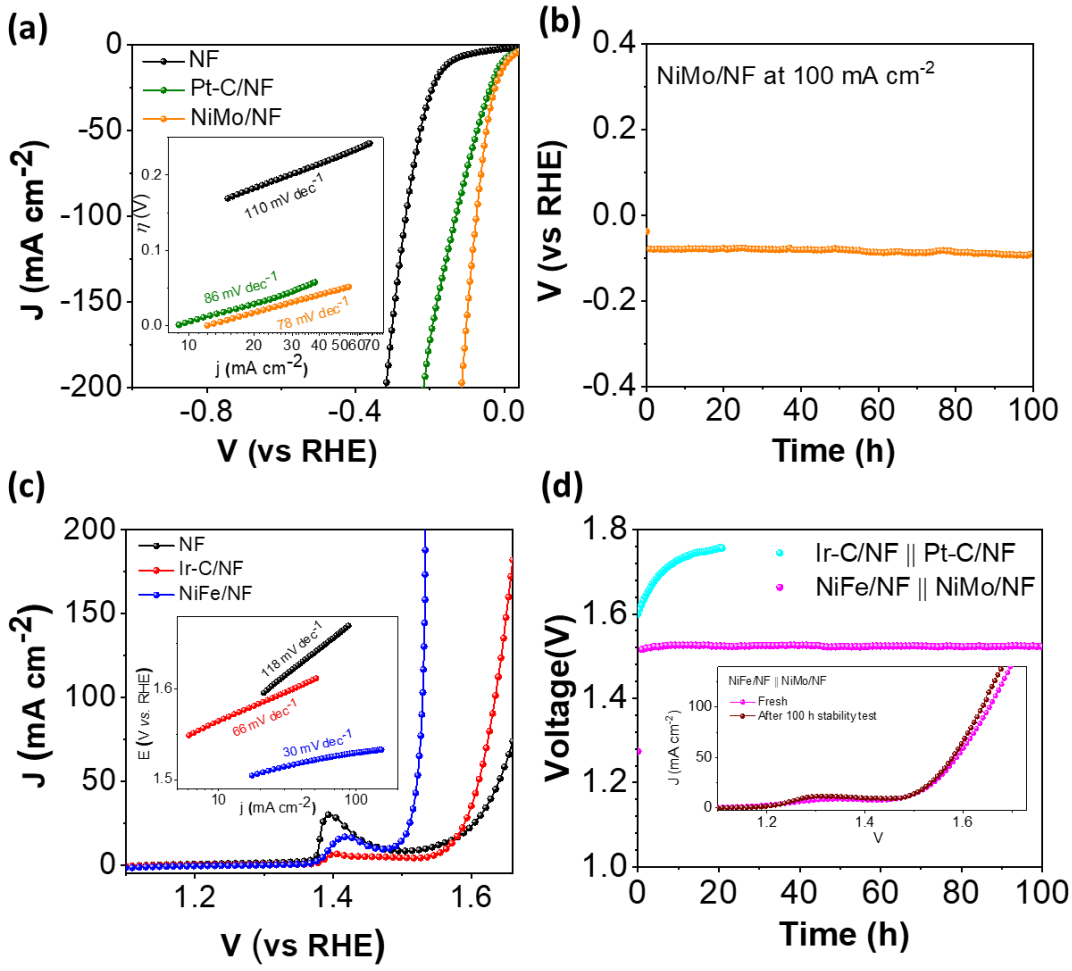

Figure B5: Electrochemical performance of HER and OER electrodes. (a) Linear sweep voltammetry (LSV) curves of NiMo/NF, Pt-C/NF and NF electrodes for HER with their

respective Tafel plots shown as an inset. (b) Chronopotentiometry of NiMo/NF at 100 $mAcm^{-2}$ in 1M KOH. (c) LSV curves of NiFe/NF, Ir-C/NF and NF for OER with their respective Tafel plots shown as an inset. (d) Chronopotentiometry of NiFe/NF||NiMo/NF and Ir-C/NF||Pt-C/NF at 20 $mAcm^{-2}$ in 1M KOH with LSV curves of NiFe/NF||NiMo/NF, in a two-electrode system before and after chronopotentiometry test.

The overall water splitting was evaluated in a two-electrode configuration in 1M KOH by employing NiFe/NF and NiMo/NF as anode and cathode, respectively. As discussed in Chapter 6, figure 6.2 (c), and shown in inset of figure B5 (d) the NiFe/NF||NiMo/NF delivers 10 $mAcm^{-2}$ current at a voltage of 1.48 V, which is 80 and 230 mV better than Ir-C/NF||Pt-C/NF and NF||NF, respectively. Besides the excellent activity, the stability of NiFe/NF||NiMo/NF is also superior to Ir-C/NF||Pt-C/NF, showing no degradation at 20 $mAcm^{-2}$ after 100 h operation while significant activity loss is observed for Ir-C/NF||Pt-C/NF within 20 h. Compared with the LSV curve for the as-prepared catalysts, the LSV curve taken after 100 h stability shows negligible change in overpotentials.

(a)

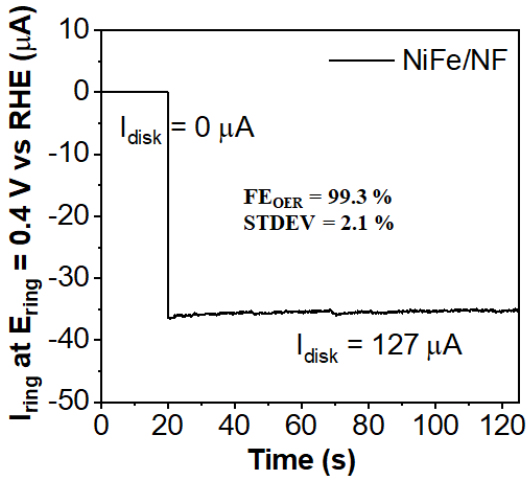

(b)

E / V vs. SCE	I / mA	Ar flow rate	H_2 peak	FE_{HER}
-1.118	-22.8	20	2820708	1.015157963
-1.118	-22.9	20	2766411	0.991269087
-1.118	-22.9	20	2751075	0.985773844
-1.168	-35.5	20	4426394	1.023132918
-1.168	-35.6	20	4295403	0.99006626
-1.168	-35.7	20	4416293	1.015079379
			FE_{HER}	99.7 ± 1.6 %
			STDEV	1.6%

Figure B6: (a) Faraday efficiency of OER by rotating ring disk electrode (RRDE), (b) Faraday efficiency of HER by flame ionisation detection- gas chromatography (FID-GC) method

The Faradaic efficiencies are calculated to be 99.7% for NiMo/NF electrode (figure B6 (b)) and 99.3% for NiFe/NF electrode (figure B6 (a)), respectively, suggesting there are no side reactions other than the hydrogen evolution and oxygen evolution reactions at the respective electrodes. In summary, the electrochemical performance tests confirm the as-developed NiFe/NF||NiMo/NF electrodes form a highly active and robust catalytic system for overall water splitting.

Table B1. Comparison of HER performance of NiMo/NF with previously reported HER electrocatalysts in 1 M KOH

Catalyst	Overpotential	Electrolyte	Ref.
NiMo/NF	**6 mV at 10 mA cm^{-2} 70 mV at 100 mA cm^{-2}**	**1M KOH**	**This Study**
Ni(Cu)VO_x	21 mV at 10 mA cm^{-2}	1M KOH	[227]
C–MoS_2	45 mV at 10 mA cm^{-2}	1M KOH	[228]
SA Co-D 1T MoS_2	42 mV at 10 mA cm^{-2}	1M KOH	[229]
NiMo-65	17 mV at 10 mA cm^{-2}	1M KOH	[230]
Ni-Mo-N/ CFC	40 mV at 10 mA cm^{-2}	1M KOH	[231]
NiO at 1T-MoS_2	46 mV at 10 mA cm^{-2}	1M KOH	[232]
NiMo/Ni foam	73 mV at 10 mA cm^{-2}	1M KOH	[233]
NiMoCo at NF	23 mV at 10 mA cm^{-2}	1M KOH	[234]

$NiCo_2Mo$/Cu	125 mV at 10 mA cm^{-2}	1M KOH	[235]
Ni-Fe-MoN NTs	20 mV at 10 mA cm^{-2}	1M KOH	[236]
$MoNi_4/MoO_2$ at Ni	15 mV at 10 mA cm^{-2}	1M KOH	[141]
$MoNi_4/MoO_{3-x}$	17 mV at 10 mA cm^{-2}	1M KOH	[73]
Co_4N at NC	62 mV at 10 mA cm^{-2}	1M KOH	[237]
CoFe-MOF TPAs/Ni	43 mV at 10 mA cm^{-2}	1M KOH	[238]
NiCoP/CC	62 mV at 10 mA cm^{-2}	1M KOH	[239]

Appendix C

Perovskite solar cells fabrication used in Chapter 4 and 6, PL and stability measurements in Chapter 6 were performed by The Duong, The Australian National University. Appendix C covers the fabrication and additional characterisation details of perovskite cells.

C.1. Perovskite cell fabrication

ITO glass substrates were first cut into 2.0 cm × 1.8 cm rectangles and cleaned sequentially in an ultrasonic bath with acetone, 2-propanol and ethanol. Compact TiO_2 films were deposited on the substrates by spinning a solution of Titanium isopropoxide (TTIP) in 2-propanol at 5000 rpm for 15 s followed by annealing at 500 ^oC for 30 mins in air. Mesoporous TiO_2 was deposited on the substrates by spinning a solution of TiO_2 paste in ethanol at 5000 rpm for 15 s followed by an annealing at 500 ^oC for 30 mins in air. Perovskite precursor (1 ml) was prepared by mixing of $FAPbI_2Br$ (0.75 ml, 1.3 M in N,N-Dimethylformamide (DMF) / Dimethyl sulfoxide (DMSO) 4:1 volume ratio), $MAPbI_2Br$ (0.15 ml, 1.3 M in DMF/DMSO 4:1 volume ratio), $CsPbI_2Br$ (0.1 ml, 1.3 M in DMSO) and RbI (0.05 ml, 1.3 M in DMSO). Perovskite was deposited on the substrates by spinning the solution (40 µl) at 2000 rpm for 10 s (acceleration rate 200 rpm/s) and 6000 rpm (acceleration rate 1000 rpm/s) for 20 s. Chlorobenzene (150 µl) was dropped at the middle of the substrates 5 s before the spinning program ends. This was then followed by annealing at 100 ^oC on a hotplate for 30 mins. n-butylammonium bromide (90 µl) diluted in 2-propanol with a concentration of 1.1 mg/ml was spun on the substrates at 5000 rpm for 30 s followed by a short annealing step at 100^oC for 5 mins (for perovskite cells used in Chapter 4). N-dodecylammonium (90 µl) diluted in 2-

propanol with a concentration of 3.1 mg/ml was spun on the substrates at 5000 rpm for 30 s followed by a short annealing step at 100 ^{o}C for 5 mins (for perovskite cells used in Chapter 6). Spiro-MeOTAD layer was deposited on the perovskite films by spinning the solution of Spiro-MeOTAD (40 µl, 72 mg/ml) in chlorobenzene with Li-TFSI (17.5 µl, 520 mg/ml in acetonitrile) and 4-tBp (28.5 µl) at 4000 rpm for 30 mins. 5 nm of MoO_3 was deposited on the substrate by thermal evaporation at very low vacuum (2×E-7 Torr). 30 nm of IZO was then deposited on the substrates by radio frequency sputtering through a shadow mask. Finally, metal grids were deposited on top of the IZO layers by electron-beam evaporation technique.

C.2. Perovskite cell additional characterisation

Semitransparent perovskite solar cells were fabricated using a 3D perovskite light absorber ($Rb_{0.05}Cs_{0.095}MA_{0.1425}FA_{0.7125}PbI_2Br$). For perovskite cells used in Chapter 4, n-butylammonium bromide ($C_4H_{12}BrN$) 2D perovskite layer is used for surface passivation.

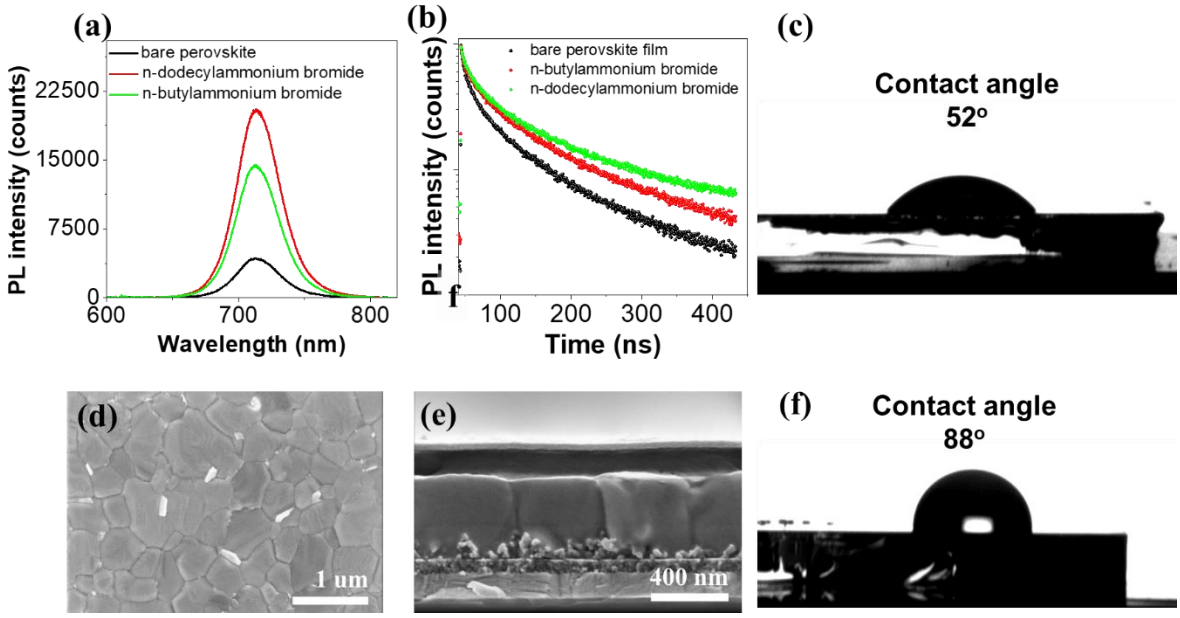

Figure C1: (a) Steady state photoluminescence (PL) spectra (left) and (b) time-resolved photoluminescence (TRPL) (right) of bare perovskite film and perovskite films passivated with n-butylammonium bromide and n-dodecylammonium bromide. (c,f) H_2O contact angle of bare perovskite film and perovskite films passivated with n-butylammonium bromide and n-dodecylammonium bromide. (d) Top and (e) cross sectional SEM of perovskite solar cell.

To improve the STH efficiency, it is important to design the perovskite-Si tandem to match the potential requirements of the catalysts to achieve unassisted water splitting. Perovksite cell performance is further improved to improve the open circuit potential of perovskite cell and hence the perovskite-Si tandem cell to match with the NiMo-NiFe catalysts. To realise high photovoltage, the surface of the active perovskite layer was passivated with a large organic cation n-dodecylammonium bromide ($C_{12}H_{28}BrN$) consisiting of a long alkyl chain, which is known to form two-dimensional (2D) perovskites.[191] The organic cation with long alkyl chain presents better surface passivation compared to the n-butylammonium bromide ($C_4H_{12}BrN$) used in Chapter 4, which has a much shorter alkyl chain. This is evidenced by a significantly higher photoluminescence (PL) intensity and carrier lifetime in the n-dodecylammonium bromide passivated perovskite film as compared to the bare perovskite film and perovskite film passivated by n-butylammonium bromide (**figure C1** a,b). In addition, the use of a long alkyl chain organic cation on the perovskite surface substantially increases the hydrophobicity of the perovskite film. As shown in figure C1 (c,f), the contact angle of perovskite film to water increases from 52^o to 88^o upon passivating the perovskite film with n-dodecylammonium bromide, which could potentially lead to enhanced moisture stability of perovskite solar cells. Figure C (d,e) shows the top-view and crosssectional SEM images of the

perovskite cell, where the semi-transparent rear contact is comprised of a MoO_3 buffer layer and a indium doped zinc oxide (IZO) contact with a thickness of 7 nm and 40 nm, respectively.

Table C.1. Summary of reported semi-transparent perovskite solar cells with respective perovskite composition, optical bandgap and with a V_{oc} higher than 1.1V.

Perovskite composition	**Optical bandgap (eV)**	**Active area (cm^2)**	**V_{oc}**	**Year**	**Reference**
$Rb_{0.05}Cs_{0.1}MA_{0.15}FA_{0.75}PbI_2Br$	**1.72**	**1.32**	**1.271**	**2020**	**This work**
$Rb_{0.05}Cs_{0.1}MA_{0.15}FA_{0.75}PbI_xBr_{1-x}$	1.62	0.3	1.14	2020	[240]
	1.75		1.22		
$FA_{0.75}Cs_{0.25}Pb(I_{0.8}Br_{0.2})_3$	1.67	0.34	1.214	2020	[241]
$Cs_{0.05}FA_{0.81}MA_{0.14}PbI_{2.55}Br_{0.45}$	1.63	0.049	1.12	2020	[242]
		1	1.1		
$FA_{0.83}Cs_{0.17}Pb(I_{1-y}Br_y)_3$	1.65	0.105	1.16	2020	[243]
	1.69		1.21		
	1.74		1.24		
	1.79		1.23		
$Rb_{0.05}Cs_{0.1}MA_{0.15}FA_{0.75}PbI_2Br$	1.72	1	1.205	2020	[244]
$Rb_{0.05}Cs_{0.1}MA_{0.15}FA_{0.75}PbI_2Br$	1.72	0.3	1.13	2017	[245]
$Rb_{0.05}Cs_{0.1}MA_{0.15}FA_{0.75}PbI_xBr_{1-x}$	1.62	0.3	1.14	2017	[246]
	1.75		1.19		
$FA_{0.83}Cs_{0.17}Pb(I_{0.6}Br_{0.4})_3$	1.73	0.715	1.1	2016	[247]

Appendix D

Chapter 4: Silicon Photocathodes with Carrier Selective Passivated Contacts, and Earth Abundant Catalyst for High Performance, Low-Cost, Direct Solar Hydrogen Generation

Relevant manuscript: Astha Sharma, The Doung, Peng Liu, Doudou Zhang, Di Yan, Christian Samundsett, Heping Shen, Siva Karuturi, Kylie Catchpole and Fiona J. Beck. "Silicon photocathodes with carrier selective passivated contacts, and earth abundant catalyst for high performance, low-cost, direct solar hydrogen generation." *Under review in Sustainable energy and fuels*

Author contribution: A.S., S.K., K.C. and F.J.B. conceived the study. S.K., and F.J.B. directed the project. A.S. designed the experiments and performed data analysis. A.S., D.Y. and C.S. developed Si photocathode. A.S. developed NiMo catalyst. A.S. performed catalyst characterisation and performance analysis. D.Z. advised on catalyst analysis. A.S. performed Si photocathode and catalyst characterisation and performance analysis. A.S., J.S., A.R. performed gas chromatography measurements. T.D. fabricated the perovskite solar cells and performed solid state perovskite solar cell measurements. P.L. fabricated the NiFe OER anode and performed, the catalyst measurements. A.S. performed integrated system measurements and performance analysis. D.J., H.S., C.Y., S.K., K.C., and F.J.B. advised. All the authors reviewed and commented on the manuscript.

Chapter 5: Quantifying and comparing fundamental loss mechanisms to enable solar to hydrogen conversion efficiencies above 20% using perovskite-silicon tandem absorbers

Relevant manuscript: Astha Sharma, and Fiona J. Beck. "Quantifying and Comparing Fundamental Loss Mechanisms to Enable Solar-to-Hydrogen Conversion Efficiencies above 20% Using Perovskite–Silicon Tandem Absorbers." *Advanced Energy and Sustainability Research*: 2000039.

Author contribution: A.S., and F.J.B, conceived the study. F.J.B. directed the project. A.S. developed the model, performed the theoretical analysis and wrote the manuscript.

Chapter 6: Direct solar hydrogen generation at 20% efficiency using low-cost materials

Relevant manuscript: Yuan Wang*, **Astha Sharma***, The Duong, Hamidreza Arandiyan, Tingwen Zhao, Doudou Zhang, Zhen Su, Magnus Garbrecht, Fiona J. Beck, Siva Karuturi, Chuan Zhao and Kylie Catchpole. "Direct Solar Hydrogen Generation at 20% Efficiency Using Low-Cost Materials. " *Advanced Energy Materials*, 2101053

Author contribution: A.S., Y.W., S.K., C.Z., K.C. conceived the study. S.K., C.Z., and K.C. directed the project. A.S. and Y.W. designed the experiments and performed data analysis. A.S., and Y.W., wrote the manuscript. Y.W. synthesized electrocatalysts and performed electrochemical analysis. T.D. developed high-efficiency semi-transparent perovskite solar cells. A.S. and T.D. performed tandem solar cell measurements. A.S. performed photoelectrochemical measurements and analysis. A.S. developed the DSHG system model

and performed the theoretical efficiency analysis. A.S. developed the model and performed LOCH calculations. F.J.B. advised A.S. on theoretical calculations. H.A. and M.G. conducted atomic-resolution TEM, HAADF-STEM and EDS mapping of catalysts. Z.S. performed XPS analysis of catalysts. T.Z. and D.Z. contributed to electrochemical experiments. All the authors reviewed and commented on the manuscript. A.S. and Y.W. contributed equally to the manuscript.

REFERENCES

1. IPCC, *Global Warming of 1.5°C. An IPCC Special Report on the impacts of global warming of 1.5°C above pre-industrial levels and related global greenhouse gas emission pathways, in the context of strengthening the global response to the threat of climate change, sustainable development, and efforts to eradicate poverty. IPCC, Geneva, Switzerland.* 2018

2. Taibi, E., et al., *Hydrogen from renewable power: Technology outlook for the energy transition*. 2018, Tech. rep., International Renewable Energy Agency (IRENA).

3. *Accelerating the Energy Transition through Innovation*. 2017, International Renewable Energy Agency (IRENA): Abu Dhabhi, Dubai

4. *International Technology Roadmap for Photovoltaic (ITRPV) results, 10th edition.* International Technology Roadmap for Photovoltaic (ITRPV) results, 10th edition, 2019.

5. *Global energy transformation: A roadmap to 2050 (2019 edition), Abu Dhabi.* International Renewable Energy Agency, 2019.

6. IEA, *The Future of Hydrogen, IEA, Paris.* 2019.

7. US Department of Energy, A.f.d.c., *Fuel cell electric vehicles* https://afdc.energy.gov/vehicles/fuel_cell.html, accessed Feb 2021.

8. ALSTOM, *Coradia iLint – the world's 1st hydrogen powered train.* https://www.alstom.com/solutions/rolling-stock/coradia-ilint-worlds-1st-hydrogen-powered-train, accessed Feb 2021.

9. ALSTOM, *Alstom's hydrogen train successfully completes three months of testing in Austria.* https://www.alstom.com/press-releases-news/2020/12/alstoms-hydrogen-train-successfully-completes-three-months-testing#:~:text=1%20December%202020%20%E2%80%93%20Alstom's%20Coradia,Austrian%20Federal%20Railways)%20regional%20lines

December 2020.

10. Airbus, *Airbus reveals new zero emission concept aircraft* https://www.airbus.com/newsroom/press-releases/en/2020/09/airbus-reveals-new-zeroemission-concept-aircraft.html

September 2020.

11. Steilen, M. and L. Jörissen, *Hydrogen conversion into electricity and thermal energy by fuel cells: use of H2-systems and batteries*, in *Electrochemical energy storage for renewable sources and grid balancing*. 2015, Elsevier. p. 143-158.

12. consulting, A.A., *Opportunities for Australia from hydrogen export, Australian Renewable Energy Agency (ARENA).* 2018.

13. Agency, I.R.E., *Hydrogen: A renewable energy perspective.* 2019

14. Energy, U.D.o., *DOE Technical Targets for Hydrogen Production from Electrolysis.* https://www.energy.gov/eere/fuelcells/doe-technical-targets-hydrogen-production-electrolysis, access, April 2021.

15. Australian Government, D.o.I., Science, Energy and Resources *Technology Investment Roadmap: First Low Emissions Technology Statement 2020.* 2020.

16. Rajeshwar, K., R. McConnell, and S. Licht, *Solar hydrogen generation*. 2008: Springer.

17. Shaner, M.R., et al., *A comparative technoeconomic analysis of renewable hydrogen production using solar energy.* Energy and Environmental Science 2016. **9**(7): p. 2354-2371.

18. (DOE), U.S.D.o.E., *DOE technical targets for hydrogen production from photoelectrochemical hydrogen production.* https://www.energy.gov/eere/fuelcells/doe-technical-targets-hydrogen-production-photoelectrochemical-water-splitting, accessed May 18, 2020.

19. Bolton, J.R., S.J. Strickler, and J.S. Connolly, *Limiting and realizable efficiencies of solar photolysis of water.* Nature 1985. **316**(6028): p. 495-500.

20. Archer, M.D. and J.R. Bolton, *Requirements for ideal performance of photochemical and photovoltaic solar energy converters.* Journal of Physical Chemistry, 1990. **94**(21): p. 8028-8036.

21. Beck, F.J., *Rational Integration of Photovoltaics for Solar Hydrogen Generation.* ACS Applied Energy Materials, 2019. **2**(9): p. 6395-6403.

22. Astha Sharma, F.J.B., *Quantifying and Comparing Fundamental Loss Mechanisms to Enable Solar-to-Hydrogen Conversion Efficiencies above 20% Using Perovskite–Silicon Tandem Absorbers.* Advanced energy and sustainability research 2020.

23. Fountaine, K.T., H.J. Lewerenz, and H.A. Atwater, *Efficiency limits for photoelectrochemical water-splitting.* Nature communications, 2016. **7**(1): p. 1-9.

24. Weber, M.F. and M.J. Dignam, *Efficiency of splitting water with semiconducting photoelectrodes.* Journal of The Electrochemical Society, 1984. **131**(6): p. 1258-1265.

25. Wang, T., et al., *Controllable fabrication of nanostructured materials for photoelectrochemical water splitting via atomic layer deposition.* 2014. **43**(22): p. 7469-7484.

26. Kubacka, A., M. Fernandez-Garcia, and G.J.C.r. Colon, *Advanced nanoarchitectures for solar photocatalytic applications.* 2012. **112**(3): p. 1555-1614.

27. Liu, R., et al., *Water splitting by tungsten oxide prepared by atomic layer deposition and decorated with an oxygen-evolving catalyst.* 2011. **50**(2): p. 499-502.

28. Lin, Y., et al., *Nanonet-based hematite heteronanostructures for efficient solar water splitting.* Journal of the American Chemical Society, 2011. **133**(8): p. 2398-2401.

29. Luo, J., et al., *Water photolysis at 12.3% efficiency via perovskite photovoltaics and Earth-abundant catalysts.* 2014. **345**(6204): p. 1593-1596.

30. Kang, D., et al., *Printed assemblies of GaAs photoelectrodes with decoupled optical and reactive interfaces for unassisted solar water splitting.* 2017. **2**(5): p. 17043.

31. Schüttauf, J.-W., et al., *Solar-to-hydrogen production at 14.2% efficiency with silicon photovoltaics and earth-abundant electrocatalysts.* Journal of The Electrochemical Society, 2016. **163**(10): p. F1177-F1181.

32. Jacobsson, T.J., et al., *A theoretical analysis of optical absorption limits and performance of tandem devices and series interconnected architectures for solar hydrogen production.* Solar Energy Materials, 2015. **138**: p. 86-95.

33. Shockley, W. and H.J. Queisser, *Detailed balance limit of efficiency of p-n junction solar cells.* Journal of applied physics, 1961. **32**(3): p. 510-519.

34. Ingler Jr, W.B. and S.U. Khan, *A Self-Driven p/n-Fe2O3 Tandem Photoelectrochemical Cell for Water Splitting.* Electrochemical and Solid State Letters, 2006. **9**(4): p. G144.

35. Wang, H., T. Deutsch, and J.A. Turner, *Direct water splitting under visible light with nanostructured hematite and WO3 photoanodes and a GaInP2 photocathode.* Journal of the Electrochemical Society, 2008. **155**(5): p. F91.

36. Xu, P., et al., *Photoelectrochemical cell for unassisted overall solar water splitting using a BiVO 4 photoanode and Si nanoarray photocathode.* RSC advances, 2016. **6**(12): p. 9905-9910.

37. Bornoz, P., et al., *A bismuth vanadate–cuprous oxide tandem cell for overall solar water splitting.* The Journal of Physical Chemistry C, 2014. **118**(30): p. 16959-16966.

38. Kim, J.H., et al., *Wireless solar water splitting device with robust cobalt-catalyzed, dual-doped BiVO4 photoanode and perovskite solar cell in tandem: a dual absorber artificial leaf.* ACS nano, 2015. **9**(12): p. 11820-11829.

39. Shi, X., et al., *Unassisted photoelectrochemical water splitting beyond 5.7% solar-to-hydrogen conversion efficiency by a wireless monolithic photoanode/dye-sensitised solar cell tandem device.* Nano Energy, 2015. **13**: p. 182-191.

40. Shi, X., et al., *Unassisted photoelectrochemical water splitting exceeding 7% solar-to-hydrogen conversion efficiency using photon recycling.* Nature communications, 2016. **7**(1): p. 1-6.

41. Khaselev, O. and J.A. Turner, *A monolithic photovoltaic-photoelectrochemical device for hydrogen production via water splitting.* Science, 1998. **280**(5362): p. 425-427.

42. Cheng, W.-H., et al., *Monolithic photoelectrochemical device for 19% direct water splitting.* 2017.

43. Young, J.L., et al., *Direct solar-to-hydrogen conversion via inverted metamorphic multi-junction semiconductor architectures.* Nature Energy, 2017. **2**(4): p. 1-8.

44. Jia, J., et al., *Solar water splitting by photovoltaic-electrolysis with a solar-to-hydrogen efficiency over 30%.* 2016. **7**(1): p. 1-6.

45. Horowitz, K.A., et al., *A techno-economic analysis and cost reduction roadmap for III-V solar cells*. 2018, National Renewable Energy Lab.(NREL), Golden, CO (United States).

46. S.Philipps, *''Photovoltaics report'', Fraunhofer Institute for solar energy systems,ISE, Freiburg, Germany, .* ''Photovoltaics report'', Fraunhofer Institute for solar energy systems,ISE, Freiburg, Germany, , 2018.

47. Yoshikawa, K., et al., *Silicon heterojunction solar cell with interdigitated back contacts for a photoconversion efficiency over 26%.* Nature energy, 2017. **2**(5): p. 17032.

48. Yu, Z.J., M. Leilaeioun, and Z. Holman, *Selecting tandem partners for silicon solar cells.* Nature Energy, 2016. **1**(11): p. 1-4.

49. White, T.P., N.N. Lal, and K.R. Catchpole, *Tandem solar cells based on high-efficiency c-Si bottom cells: top cell requirements for> 30% efficiency.* IEEE Journal of Photovoltaics, 2013. **4**(1): p. 208-214.

50. De Wolf, S., et al., *Organometallic halide perovskites: sharp optical absorption edge and its relation to photovoltaic performance.* The journal of physical chemistry letters, 2014. **5**(6): p. 1035-1039.

51. Unger, E., et al., *Roadmap and roadblocks for the band gap tunability of metal halide perovskites.* Journal of Materials Chemistry A, 2017. **5**(23): p. 11401-11409.

52. Lal, N.N., T.P. White, and K.R.J.I.J.o.P. Catchpole, *Optics and light trapping for tandem solar cells on silicon.* 2014. **4**(6): p. 1380-1386.

53. Monteiro Lunardi, M., et al., *A life cycle assessment of perovskite/silicon tandem solar cells.* Progress in photovoltaics: research and applications, 2017. **25**(8): p. 679-695.

54. Chang, N.L., et al., *A bottom-up cost analysis of silicon–perovskite tandem photovoltaics.* 2020.

55. Werner, J., B. Niesen, and C. Ballif, *Perovskite/silicon tandem solar cells: Marriage of convenience or true love story?–An overview.* Advanced Materials Interfaces, 2018. **5**(1): p. 1700731.

56. Kojima, A., et al., *Organometal halide perovskites as visible-light sensitizers for photovoltaic cells.* Journal of the American Chemical Society, 2009. **131**(17): p. 6050-6051.

57. NREL, *https://www.nrel.gov/pv/cell-efficiency.html.* accessed 27 Januray 2021.

58. Bailie, C.D., et al., *Semi-transparent perovskite solar cells for tandems with silicon and CIGS.* Energy & Environmental Science, 2015. **8**(3): p. 956-963.

59. Mailoa, J.P., et al., *A 2-terminal perovskite/silicon multijunction solar cell enabled by a silicon tunnel junction.* Applied Physics Letters, 2015. **106**(12): p. 121105.

60. *https://www.pv-magazine.com/2020/12/21/oxford-pv-retakes-tandem-cell-efficiency-record/#:~:text=Perovskite%20developer%20Oxford%20PV%20has,U.S.%20National%20Renewable%20Energy%20Laboratory.* accessed 27 January 2021.

61. Duong, T., et al., *High Efficiency Perovskite-Silicon Tandem Solar Cells: Effect of Surface Coating versus Bulk Incorporation of 2D Perovskite.* 2020. **10**(9): p. 1903553.

62. Coletti, G., et al., *Bifacial four-terminal perovskite/silicon tandem solar cells and modules.* ACS Energy Letters, 2020. **5**(5): p. 1676-1680.

63. ITRPV, *International Technology Roadmap for Photovoltaic (ITRPV) results, 10th edition.* 2019.

64. Karuturi, S.K., et al., *Over 17% Efficiency Stand-Alone Solar Water Splitting Enabled by Perovskite-Silicon Tandem Absorbers.* Advanced Energy Materials, 2020: p. 2000772.

65. Park, H., et al., *Water Splitting Exceeding 17% Solar-to-Hydrogen Conversion Efficiency Using Solution-Processed Ni-Based Electrocatalysts and Perovskite/Si Tandem Solar Cell.* ACS applied materials interfaces, 2019. **11**(37): p. 33835-33843.

66. Gao, J., et al., *Solar Water Splitting with Perovskite/Silicon Tandem Cell and TiC-Supported Pt Nanocluster Electrocatalyst.* Joule, 2019. **3**(12): p. 2930-2941.

67. Kim, J.H., Y.K. Kim, and J.S. Lee, *Perovskite Tandems Advance Solar Hydrogen Production.* Joule, 2019. **3**(12): p. 2892-2894.

68. Roger, I., M.A. Shipman, and M.D. Symes, *Earth-abundant catalysts for electrochemical and photoelectrochemical water splitting.* Nature Reviews Chemistry, 2017. **1**(1): p. 0003.

69. IRENA, *Green Hydrogen Cost Reduction: Scaling up Electrolysers to Meet the 1.5^{o}C Climate Goal,.* International Renewable Energy Agency, Abu Dhabi, 2020.

70. Bergmann, A., et al., *Unified structural motifs of the catalytically active state of Co(oxyhydr)oxides during the electrochemical oxygen evolution reaction.* Nature Catalysis, 2018. **1**(9): p. 711-719.

71. Garcés-Pineda, F.A., et al., *Direct magnetic enhancement of electrocatalytic water oxidation in alkaline media.* Nature Energy, 2019. **4**(6): p. 519-525.

72. Lu, X.F., L. Yu, and X.W. Lou, *Highly crystalline Ni-doped FeP/carbon hollow nanorods as all-pH efficient and durable hydrogen evolving electrocatalysts.* Science Advances, 2019. **5**(2): p. eaav6009.

73. Chen, Y.-Y., et al., *Self-Templated Fabrication of MoNi4/MoO3-x Nanorod Arrays with Dual Active Components for Highly Efficient Hydrogen Evolution.* Advanced Materials, 2017. **29**(39): p. 1703311.

74. Suntivich, J., et al., *A Perovskite Oxide Optimized for Oxygen Evolution Catalysis from Molecular Orbital Principles.* Science, 2011. **334**(6061): p. 1383-1385.

75. Suryanto, B.H.R., et al., *Overall electrochemical splitting of water at the heterogeneous interface of nickel and iron oxide.* Nature Communications, 2019. **10**(1): p. 5599.

76. Duan, J., S. Chen, and C. Zhao, *Ultrathin metal-organic framework array for efficient electrocatalytic water splitting.* Nature Communications, 2017. **8**: p. 15341.

77. Wang, Y., et al., *Microwave-Induced Plasma Synthesis of Defect-Rich, Highly Ordered Porous Phosphorus-Doped Cobalt Oxides for Overall Water Electrolysis.* The Journal of Physical Chemistry C, 2020. **124**(18): p. 9971-9978.

78. Zhao, T., et al., *Vertical Growth of Porous Perovskite Nanoarrays on Nickel Foam for Efficient Oxygen Evolution Reaction.* ACS Sustainable Chemistry & Engineering, 2020. **8**(12): p. 4863-4870.

79. Rocheleau, R.E. and E.L. Miller, *Photoelectrochemical production of hydrogen: Engineering loss analysis.* International Journal of Hydrogen Energy, 1997. **22**(8): p. 771-782.

80. Zhao, Y., C. Ou, and J. Chen, *A new analytical approach to model and evaluate the performance of a class of irreversible fuel cells.* International Journal of Hydrogen Energy, 2008. **33**(15): p. 4161-4170.

81. Diéguez, P., et al., *Thermal performance of a commercial alkaline water electrolyzer: experimental study and mathematical modeling.* international journal of hydrogen energy, 2008. **33**(24): p. 7338-7354.

82. Zhang, H., G. Lin, and J. Chen, *Evaluation and calculation on the efficiency of a water electrolysis system for hydrogen production.* international journal of hydrogen energy, 2010. **35**(20): p. 10851-10858.

83. Zhang, H., et al., *Configuration design and performance optimum analysis of a solar-driven high temperature steam electrolysis system for hydrogen production.* International Journal of Hydrogen Energy, 2013. **38**(11): p. 4298-4307.

84. Nafchi, F.M., et al., *Performance assessment of a solar hydrogen and electricity production plant using high temperature PEM electrolyzer and energy storage.* International Journal of Hydrogen Energy, 2018. **43**(11): p. 5820-5831.

85. Ross, R.T. and T.L. Hsiao, *Limits on the yield of photochemical solar energy conversion.* Journal of Applied Physics, 1977. **48**(11): p. 4783-4785.

86. Hu, S., et al., *An analysis of the optimal band gaps of light absorbers in integrated tandem photoelectrochemical water-splitting systems.* Energy Environmental Science, 2013. **6**(10): p. 2984-2993.

87. Holmes-Gentle, I. and K. Hellgardt, *A versatile open-source analysis of the limiting efficiency of photo electrochemical water-splitting.* Scientific reports, 2018. **8**(1): p. 1-9.

88. Jacobsson, T.J., et al., *Sustainable solar hydrogen production: from photoelectrochemical cells to PV-electrolyzers and back again.* Energy Environmental Science, 2014. **7**(7): p. 2056-2070.

89. Winkler, M.T., et al., *Modeling integrated photovoltaic–electrochemical devices using steady-state equivalent circuits.* Proceedings of the National Academy of Sciences, 2013. **110**(12): p. E1076-E1082.

90. Haussener, S., et al., *Simulations of the irradiation and temperature dependence of the efficiency of tandem photoelectrochemical water-splitting systems.* Energy and Environmental Science, 2013. **6**(12): p. 3605-3618.

91. Urbain, F., et al., *Influence of the operating temperature on the performance of silicon based photoelectrochemical devices for water splitting.* Materials science in semiconductor processing, 2016. **42**: p. 142-146.

92. Green, M.A., et al., *Solar cell efficiency tables (version 56).* Progress in Photovoltaics: Research and Applications, 2020. **28**(7): p. 629-638.

93. Fraunhofer Institute for Solar Energy Systems, I.w.s.o.P.P.G., *Photovoltaics report.* 2020.

94. reviews, C.e., *Most efficienct solar panels 2021.* 2021.

95. *International Technology Roadmap for Photovoltaic (ITRPV).* 2020.

96. Green, M.A. and R. Godfrey, *MIS solar cell—General theory and new experimental results for silicon.* Applied Physics Letters, 1976. **29**(9): p. 610-612.

97. Blakers, A. and M. Green, *678-mV open-circuit voltage silicon solar cells.* Applied Physics Letters, 1981. **39**(6): p. 483-485.

98. Blakers, A., et al., *18-percent efficient terrestrial silicon solar cells.* IEEE electron device letters, 1984. **5**(1): p. 12-13.

99. Blakers, A.W., et al., *22.8% efficient silicon solar cell.* Applied Physics Letters, 1989. **55**(13): p. 1363-1365.

100. Green, M.A., et al., *Characterization of 23-percent efficient silicon solar cells.* IEEE Transactions on Electron Devices, 1990. **37**(2): p. 331-336.

101. Green, M.A., *The passivated emitter and rear cell (PERC): From conception to mass production.* Solar Energy Materials and Solar Cells, 2015. **143**: p. 190-197.

102. Blakers, A., *Development of the PERC solar cell.* IEEE Journal of Photovoltaics, 2019. **9**(3): p. 629-635.

103. Zhao, J., et al., *24% efficient perl silicon solar cell: recent improvements in high efficiency silicon cell research.* Solar energy materials and solar cells, 1996. **41**: p. 87-99.

104. Zhao, J., et al., *19.8% efficient "honeycomb" textured multicrystalline and 24.4% monocrystalline silicon solar cells.* Applied physics letters, 1998. **73**(14): p. 1991-1993.

105. Zhao, J., A. Wang, and M.A. Green, *24· 5% Efficiency silicon PERT cells on MCZ substrates and 24· 7% efficiency PERL cells on FZ substrates.* Progress in Photovoltaics: Research and Applications, 1999. **7**(6): p. 471-474.

106. Green, M.A., *The path to 25% silicon solar cell efficiency: History of silicon cell evolution.* Progress in Photovoltaics: Research and Applications, 2009. **17**(3): p. 183-189.

107. MacDonald, D. *The emergence of n-type silicon for solar cell manufacture*. in *50th Annual AuSES Conference (Solar 2012), Melbourne, Australia*. 2012.

108. Richter, A., et al., *n-Type Si solar cells with passivating electron contact: Identifying sources for efficiency limitations by wafer thickness and resistivity variation.* 2017. **173**: p. 96-105.

109. Fu, H.-C., et al., *Spontaneous solar water splitting with decoupling of light absorption and electrocatalysis using silicon back-buried junction.* 2020. **11**(1): p. 1-9.

110. Sun, K., et al., *Enabling silicon for solar-fuel production.* Chemical reviews, 2014. **114**(17): p. 8662-8719.

111. Fan, R., Z. Mi, and M. Shen, *Silicon based photoelectrodes for photoelectrochemical water splitting.* Optics express, 2019. **27**(4): p. A51-A80.

112. Fan, R., et al., *Highly efficient and stable Si photocathode with hierarchical MoS2/Ni3S2 catalyst for solar hydrogen production in alkaline media.* 2020. **71**: p. 104631.

113. Vijselaar, W., et al., *Spatial decoupling of light absorption and catalytic activity of Ni–Mo-loaded high-aspect-ratio silicon microwire photocathodes.* 2018. **3**(3): p. 185-192.

114. Vijselaar, W., et al., *Efficient and stable silicon microwire photocathodes with a nickel silicide interlayer for operation in strongly alkaline solutions.* ACS energy letters, 2018. **3**(5): p. 1086-1092.

115. Spitler, M.T., et al., *Practical challenges in the development of photoelectrochemical solar fuels production.* 2020. **4**(3): p. 985-995.

116. Sarkar, J., *Sputtering materials for VLSI and thin film devices*. 2010: William Andrew.

117. Huang, G., et al., *Integrated MoSe2 with n+ p-Si photocathodes for solar water splitting with high efficiency and stability.* 2018. **112**(1): p. 013902.

118. Cabán-Acevedo, M., et al., *Efficient hydrogen evolution catalysis using ternary pyrite-type cobalt phosphosulphide.* 2015. **14**(12): p. 1245-1251.

119. Fan, R., et al., *Efficient and stable silicon photocathodes coated with vertically standing nano-MoS2 films for solar hydrogen production.* 2017. **9**(7): p. 6123-6129.

120. Park, M.-J., et al., *Improved photoelectrochemical hydrogen evolution using a defect-passivated Al2O3 thin film on p-Si.* Thin Solid Films, 2016. **616**: p. 550-554.

121. Bae, D., et al., *Strategies for stable water splitting via protected photoelectrodes.* Chemical Society Reviews, 2017. **46**(7): p. 1933-1954.

122. Fan, R., et al., *n-type silicon photocathodes with Al-doped rear p+ emitter and Al2O3-coated front surface for efficient and stable H2 production.* Applied Physics Letters, 2015. **106**(21): p. 213901.

123. Abdi, F.F., et al., *Efficient solar water splitting by enhanced charge separation in a bismuth vanadate-silicon tandem photoelectrode.* Nature communications, 2013. **4**(1): p. 1-7.

124. Vanka, S., et al., *InGaN/Si Double-Junction Photocathode for Unassisted Solar Water Splitting.* ACS Energy Letters, 2020. **5**(12): p. 3741-3751.

125. Liu, B., et al., *Double-Side Si Photoelectrode Enabled by Chemical Passivation for Photoelectrochemical Hydrogen and Oxygen Evolution Reactions.* Advanced Functional Materials, 2021. **31**(3): p. 2007222.

126. Yoshikawa, K., et al., *Silicon heterojunction solar cell with interdigitated back contacts for a photoconversion efficiency over 26%.* 2017. **2**(5): p. 17032.

127. Liu, B., et al., *Double-Side Si Photoelectrode Enabled by Chemical Passivation for Photoelectrochemical Hydrogen and Oxygen Evolution Reactions.* 2020: p. 2007222.

128. Fan, R., et al., *More than 10% efficiency and one-week stability of Si photocathodes for water splitting by manipulating the loading of the Pt catalyst and TiO 2 protective layer.* Journal of Materials Chemistry A, 2017. **5**(35): p. 18744-18751.

129. Yin, Z., et al., *11.5% efficiency of TiO 2 protected and Pt catalyzed n+ np+-Si photocathodes for photoelectrochemical water splitting: manipulating the Pt distribution and Pt/Si contact.* Chemical communications, 2018. **54**(5): p. 543-546.

130. Spitler, M.T., et al., *Practical challenges in the development of photoelectrochemical solar fuels production.* Sustainable Energy & Fuels, 2020. **4**(3): p. 985-995.

131. Seger, B., et al., *Using TiO2 as a conductive protective layer for photocathodic H2 evolution.* Journal of the American Chemical Society, 2013. **135**(3): p. 1057-1064.

132. Yu, C., et al., *Recent advances in and new perspectives on crystalline silicon solar cells with carrier-selective passivation contacts.* Crystals, 2018. **8**(11): p. 430.

133. Digdaya, I.A., et al., *Interfacial engineering of metal-insulator-semiconductor junctions for efficient and stable photoelectrochemical water oxidation.* Nature communications, 2017. **8**(1): p. 1-8.

134. Fan, R., et al., *Stable and efficient multi-crystalline n+ p silicon photocathode for H2 production with pyramid-like surface nanostructure and thin Al2O3 protective layer.* Applied Physics Letters, 2015. **106**(1): p. 013902.

135. Melskens, J., et al., *Passivating contacts for crystalline silicon solar cells: From concepts and materials to prospects.* IEEE Journal of Photovoltaics, 2018. **8**(2): p. 373-388.

136. Allen, T.G., et al., *Passivating contacts for crystalline silicon solar cells.* Nature Energy, 2019. **4**(11): p. 914-928.

137. *https://www.pv-magazine.com/2020/04/02/topcon-technology-hits-23-5-in-mass-production/.* April 2020

138. Richter, A., et al., *Design rules for high-efficiency both-sides-contacted silicon solar cells with balanced charge carrier transport and recombination losses.* Nature Energy, 2021: p. 1-10.

139. Martin Green, E.D., Jochen Hohl-Ebinger, Masahiro Yoshita, Nikos Kopidakis, Xiaojing Hao, *solar cell efficiency table (version 57).* progress in photovoltaics, november 2020.

140. McKone, J.R., et al., *Ni–Mo Nanopowders for Efficient Electrochemical Hydrogen Evolution.* ACS Catalysis, 2013. **3**(2): p. 166-169.

141. Zhang, J., et al., *Efficient hydrogen production on MoNi4 electrocatalysts with fast water dissociation kinetics.* Nature Communications, 2017. **8**: p. 15437.

142. Lupi, C., A. Dell'Era, and M. Pasquali, *Nickel–cobalt electrodeposited alloys for hydrogen evolution in alkaline media.* international journal of hydrogen energy, 2009. **34**(5): p. 2101-2106.

143. Sun, T., et al., *Ordered mesoporous NiCo alloys for highly efficient electrocatalytic hydrogen evolution reaction.* international journal of hydrogen energy, 2017. **42**(10): p. 6637-6645.

144. Navarro-Flores, E., Z. Chong, and S. Omanovic, *Characterization of Ni, NiMo, NiW and NiFe electroactive coatings as electrocatalysts for hydrogen evolution in an acidic medium.* Journal of Molecular Catalysis A: Chemical, 2005. **226**(2): p. 179-197.

145. Solmaz, R. and G. Kardaş, *Electrochemical deposition and characterization of NiFe coatings as electrocatalytic materials for alkaline water electrolysis.* Electrochimica Acta, 2009. **54**(14): p. 3726-3734.

146. Ullal, Y. and A.C. Hegde, *Electrodeposition and electro-catalytic study of nanocrystalline Ni–Fe alloy.* international journal of hydrogen energy, 2014. **39**(20): p. 10485-10492.

147. Hong, S.H., et al., *High-activity electrodeposited NiW catalysts for hydrogen evolution in alkaline water electrolysis.* Applied Surface Science, 2015. **349**: p. 629-635.

148. Wang, M., et al., *The enhanced electrocatalytic activity and stability of NiW films electrodeposited under super gravity field for hydrogen evolution reaction.* international journal of hydrogen energy, 2011. **36**(5): p. 3305-3312.

149. Solmaz, R., A. Döner, and G. Kardaş, *Electrochemical deposition and characterization of NiCu coatings as cathode materials for hydrogen evolution reaction.* Electrochemistry communications, 2008. **10**(12): p. 1909-1911.

150. Solmaz, R., A. Döner, and G. Kardaş, *The stability of hydrogen evolution activity and corrosion behavior of NiCu coatings with long-term electrolysis in alkaline solution.* International journal of hydrogen energy, 2009. **34**(5): p. 2089-2094.

151. Solmaz, R. and G. Kardaş, *Hydrogen evolution and corrosion performance of NiZn coatings.* Energy Conversion and Management, 2007. **48**(2): p. 583-591.

152. Raj, I.A. and K. Vasu, *Transition metal-based hydrogen electrodes in alkaline solution—electrocatalysis on nickel based binary alloy coatings.* Journal of applied electrochemistry, 1990. **20**(1): p. 32-38.

153. Kariuki, N.N., et al., *Glad Pt–Ni alloy nanorods for oxygen reduction reaction.* Acs Catalysis, 2013. **3**(12): p. 3123-3132.

154. Jakšić, M., *Advances in electrocatalysis for hydrogen evolution in the light of the Brewer-Engel valence-bond theory.* International Journal of Hydrogen Energy, 1987. **12**(11): p. 727-752.

155. Yan, D., et al., *Phosphorus-diffused polysilicon contacts for solar cells.* Solar Energy Materials and Solar Cells, 2015. **142**: p. 75-82.

156. Liu, P., et al., *Tip-Enhanced Electric Field: A New Mechanism Promoting Mass Transfer in Oxygen Evolution Reactions.* 2021. **33**(9): p. 2007377.

157. Fan, R., et al., *Unassisted solar water splitting with 9.8% efficiency and over 100 h stability based on Si solar cells and photoelectrodes catalyzed by bifunctional Ni–Mo/Ni.* Journal of Materials Chemistry A, 2019. **7**(5): p. 2200-2209.

158. Urbain, F., et al., *Multijunction Si photocathodes with tunable photovoltages from 2.0 V to 2.8 V for light induced water splitting.* Energy & environmental science, 2016. **9**(1): p. 145-154.

159. Kirner, S., et al., *Wafer surface tuning for a-Si: H/µc-Si: H/c-Si triple junction solar cells for application in water splitting.* Energy Procedia, 2016. **102**: p. 126-135.

160. Kim, J.H., et al., *Hetero-type dual photoanodes for unbiased solar water splitting with extended light harvesting.* Nature communications, 2016. **7**(1): p. 1-9.

161. Liang, J., et al., *A low-cost and high-efficiency integrated device toward solar-driven water splitting.* ACS nano, 2020. **14**(5): p. 5426-5434.

162. Luo, J., et al., *Targeting Ideal Dual-Absorber Tandem Water Splitting Using Perovskite Photovoltaics and CuInxGa1-xSe2 Photocathodes.* Advanced Energy Materials, 2015. **5**(24): p. 1501520.

163. Kim, J.H., et al., *A precious metal-free solar water splitting cell with a bifunctional cobalt phosphide electrocatalyst and doubly promoted bismuth vanadate photoanode.* Journal of Materials Chemistry A, 2018. **6**(3): p. 1266-1274.

164. Tembhurne, S., F. Nandjou, and S. Haussener, *A thermally synergistic photo-electrochemical hydrogen generator operating under concentrated solar irradiation.* Nature Energy, 2019. **4**(5): p. 399.

165. Tembhurne, S. and S. Haussener, *Integrated photo-electrochemical solar fuel generators under concentrated irradiation II. Thermal management a crucial design consideration.* Journal of The Electrochemical Society, 2016. **163**(10): p. H999-H1007.

166. Hirst, L.C., N.J. Ekins-Daukes, and Applications, *Fundamental losses in solar cells.* Progress in Photovoltaics: Research, 2011. **19**(3): p. 286-293.

167. Würfel, P., *Thermodynamic limitations to solar energy conversion.* Physica E: Low-dimensional Systems Nanostructures 2002. **14**(1-2): p. 18-26.

168. Markvart, T., *From steam engine to solar cells: can thermodynamics guide the development of future generations of photovoltaics?* Wiley Interdisciplinary Reviews: Energy and Environment, 2016. **5**(5): p. 543-569.

169. Heidarzadeh, H., A. Rostami, and M. Dolatyari, *Management of losses (thermalization-transmission) in the Si-QDs inside 3C–SiC to design an ultra-high-efficiency solar cell.* Materials Science in Semiconductor Processing, 2020. **109**: p. 104936.

170. Todorov, T., O. Gunawan, and S. Guha, *A road towards 25% efficiency and beyond: perovskite tandem solar cells.* Molecular Systems Design Engineering, 2016. **1**(4): p. 370-376.

171. Reynolds, S. and V. Smirnov. *Modelling of two-and four-terminal thin-film silicon tandem solar cells*. in *Journal of Physics: Conference Series*. 2012. IOP Publishing.

172. Holman, J.P., *Heat transfer*. 2002: McGraw-Hill Science, Engineering & Mathematics.

173. Abdin, Z., C. Webb, and E.M. Gray, *Simulation of large photovoltaic arrays.* Solar Energy, 2018. **161**: p. 163-179.

174. Tiwari, A. and M. Sodha, *Performance evaluation of hybrid PV/thermal water/air heating system: a parametric study.* Renewable energy, 2006. **31**(15): p. 2460-2474.

175. Hammoudi, M., et al., *New multi-physics approach for modelling and design of alkaline electrolyzers.* International Journal of Hydrogen Energy, 2012. **37**(19): p. 13895-13913.

176. Schmidt, T., P. Ross Jr, and N. Markovic, *Temperature dependent surface electrochemistry on Pt single crystals in alkaline electrolytes: Part 2. The hydrogen evolution/oxidation reaction.* Journal of Electroanalytical Chemistry, 2002. **524**: p. 252-260.

177. Green, M.A. and Applications, *Lambertian light trapping in textured solar cells and light-emitting diodes: analytical solutions.* progress in Photovoltaics: Research, 2002. **10**(4): p. 235-241.

178. Fan, J.C., *Theoretical temperature dependence of solar cell parameters.* Solar cells, 1986. **17**(2-3): p. 309-315.

179. Fan, J.C. and B. Palm, *Optimal design of amorphous/crystalline tandem cells.* solar cells, 1984. **11**(3): p. 247-261.

180. Enrique, J., et al., *Theoretical assessment of the maximum power point tracking efficiency of photovoltaic facilities with different converter topologies.* Solar Energy, 2007. **81**(1): p. 31-38.

181. Reisi, A.R., et al., *Classification and comparison of maximum power point tracking techniques for photovoltaic system: A review.* 2013. **19**: p. 433-443.

182. Gibson, T.L. and N.A.J.I.j.o.h.e. Kelly, *Predicting efficiency of solar powered hydrogen generation using photovoltaic-electrolysis devices.* 2010. **35**(3): p. 900-911.

183. Enslin, J.H., et al., *Integrated photovoltaic maximum power point tracking converter.* 1997. **44**(6): p. 769-773.

184. Sullivan, C.R. and M.J. Powers. *A high-efficiency maximum power point tracker for photovoltaic arrays in a solar-powered race vehicle*. in *Proceedings of IEEE Power Electronics Specialist Conference-PESC'93*. 1993. IEEE.

185. Gong, M., et al., *An Advanced Ni–Fe Layered Double Hydroxide Electrocatalyst for Water Oxidation.* Journal of the American Chemical Society, 2013. **135**(23): p. 8452-8455.

186. Lu, X. and C. Zhao, *Electrodeposition of hierarchically structured three-dimensional nickel–iron electrodes for efficient oxygen evolution at high current densities.* Nature Communications, 2015. **6**: p. 6616.

187. Li, X., F.C. Walsh, and D. Pletcher, *Nickel based electrocatalysts for oxygen evolution in high current density, alkaline water electrolysers.* Physical Chemistry Chemical Physics, 2011. **13**(3): p. 1162-1167.

188. Gao, J., et al., *Solar Water Splitting with Perovskite/Silicon Tandem Cell and TiC-Supported Pt Nanocluster Electrocatalyst.* 2019. **3**(12): p. 2930-2941.

189. Luo, Y., et al., *Morphology and surface chemistry engineering toward pH-universal catalysts for hydrogen evolution at high current density.* Nature Communications, 2019. **10**(1): p. 269.

190. Wang, Y., et al., *Tuning the surface energy density of non-stoichiometric LaCoO3 perovskite for enhanced water oxidation.* Journal of Power Sources, 2020. **478**: p. 228748.

191. Grancini, G. and M.K. Nazeeruddin, *Dimensional tailoring of hybrid perovskites for photovoltaics.* Nature Reviews Materials, 2019. **4**(1): p. 4-22.

192. Yan, D., et al., *High efficiency n-type silicon solar cells with passivating contacts based on PECVD silicon films doped by phosphorus diffusion.* 2019. **193**: p. 80-84.

193. Green, M.A., et al., *Solar cell efficiency tables (version 56).* Progress in Photovoltaics: Research and Applications, 2020. **28**(7): p. 629-638.

194. Futscher, M.H. and B.J.A.e.l. Ehrler, *Modeling the performance limitations and prospects of perovskite/Si tandem solar cells under realistic operating conditions.* 2017. **2**(9): p. 2089-2095.

195. Almansouri, I., A. Ho-Baillie, and M.A.J.J.J.o.A.P. Green, *Ultimate efficiency limit of single-junction perovskite and dual-junction perovskite/silicon two-terminal devices.* 2015. **54**(8S1): p. 08KD04.

196. Wu, N., et al., *Identifying the cause of voltage and fill factor losses in perovskite solar cells by using luminescence measurements.* 2017. **5**(10): p. 1827-1835.

197. Yoo, J.J., et al., *Efficient perovskite solar cells via improved carrier management.* 2021. **590**(7847): p. 587-593.

198. Liu, W., et al., *Improving the Fill Factor of Perovskite Solar Cells by Employing an Amine-tethered Diketopyrrolopyrrole-Based Polymer as the Dopant-free Hole Transport Layer.* 2020. **3**(10): p. 9600-9609.

199. Kim, H.D. and H.J.S.R. Ohkita, *Potential Improvement in Fill Factor of Lead-Halide Perovskite Solar Cells.* 2017. **1**(6): p. 1700027.

200. Hu, X., et al., *Wide-Bandgap Perovskite Solar Cells With Large Open-Circuit Voltage of 1653 mV Through Interfacial Engineering.* 2018. **2**(8): p. 1800083.

201. Gharibzadeh, S., et al., *Record Open-Circuit Voltage Wide-Bandgap Perovskite Solar Cells Utilizing 2D/3D Perovskite Heterostructure.* 2019. **9**(21): p. 1803699.

202. Wu, C.-G., C.-H. Chiang, and S.H.J.N. Chang, *A perovskite cell with a record-high-V oc of 1.61 V based on solvent annealed CH 3 NH 3 PbBr 3/ICBA active layer.* 2016. **8**(7): p. 4077-4085.

203. Agarwal, S. and P.R.J.J.o.A.P. Nair, *Performance loss analysis and design space optimization of perovskite solar cells.* 2018. **124**(18): p. 183101.

204. Kayes, B.M., et al. *27.6% conversion efficiency, a new record for single-junction solar cells under 1 sun illumination*. in *2011 37th IEEE Photovoltaic Specialists Conference*. 2011. IEEE.

205. Hossain, M.I., et al., *Perovskite/silicon tandem solar cells: From detailed balance limit calculations to photon management.* 2019. **11**(1): p. 58.

206. Grimm, A., W.A. de Jong, and G.J.J.I.J.o.H.E. Kramer, *Renewable hydrogen production: A techno-economic comparison of photoelectrochemical cells and photovoltaic-electrolysis.* 2020.

207. Verlage, E., et al., *A monolithically integrated, intrinsically safe, 10% efficient, solar-driven water-splitting system based on active, stable earth-abundant electrocatalysts in conjunction with tandem III–V light absorbers protected by amorphous TiO 2 films.* Energy & Environmental Science, 2015. **8**(11): p. 3166-3172.

208. Sun, K., et al., *A stabilized, intrinsically safe, 10% efficient, solar-driven water-splitting cell incorporating earth-abundant electrocatalysts with steady-state pH gradients and product separation enabled by a bipolar membrane.* Advanced Energy Materials, 2016. **6**(13): p. 1600379.

209. Cheng, W.-H., et al., *Monolithic photoelectrochemical device for direct water splitting with 19% efficiency.* ACS Energy Letters, 2018. **3**(8): p. 1795-1800.

210. Steiner, M.A., et al., *Photoelectrochemical water splitting using strain-balanced multiple quantum well photovoltaic cells.* Sustainable Energy & Fuels, 2019. **3**(10): p. 2837-2844.

211. Ben-Naim, M., et al., *Addressing the Stability Gap in Photoelectrochemistry: Molybdenum Disulfide Protective Catalysts for Tandem III–V Unassisted Solar Water Splitting.* ACS Energy Letters, 2020. **5**: p. 2631-2640.

212. Cox, C.R., et al., *Ten-percent solar-to-fuel conversion with nonprecious materials.* Proceedings of the National Academy of Sciences, 2014. **111**(39): p. 14057-14061.

213. Nordmann, S., et al., *A monolithic all-silicon multi-junction solar device for direct water splitting.* Renewable Energy, 2016. **94**: p. 90-95.

214. Schüttauf, J.-W., et al., *Solar-to-hydrogen production at 14.2% efficiency with silicon photovoltaics and earth-abundant electrocatalysts.* Journal of The Electrochemical Society, 2016. **163**(10): p. F1177-F1181.

215. Song, H., et al., *Bifunctional NiFe inverse opal electrocatalysts with heterojunction Si solar cells for 9.54%-efficient unassisted solar water splitting.* Nano Energy, 2017. **42**: p. 1-7.

216. Fu, H.-C., et al., *Spontaneous solar water splitting with decoupling of light absorption and electrocatalysis using silicon back-buried junction.* Nature communications, 2020. **11**(1): p. 1-9.

217. Nordmann, S., et al., *Record-high solar-to-hydrogen conversion efficiency based on a monolithic all-silicon triple-junction IBC solar cell.* Solar Energy Materials and Solar Cells, 2019. **191**: p. 422-426.

218. Jacobsson, T.J., et al., *A monolithic device for solar water splitting based on series interconnected thin film absorbers reaching over 10% solar-to-hydrogen efficiency.* Energy & Environmental Science, 2013. **6**(12): p. 3676-3683.

219. Luo, J., et al., *Water photolysis at 12.3% efficiency via perovskite photovoltaics and Earth-abundant catalysts.* Science, 2014. **345**(6204): p. 1593-1596.

220. Elias, X., et al., *Neutral water splitting catalysis with a high FF triple junction polymer cell.* ACS catalysis, 2016. **6**(5): p. 3310-3316.

221. Park, H., et al., *Water Splitting Exceeding 17% Solar-to-Hydrogen Conversion Efficiency Using Solution-Processed Ni-Based Electrocatalysts and Perovskite/Si Tandem Solar Cell.* ACS applied materials & interfaces, 2019. **11**(37): p. 33835-33843.

222. Gao, J., et al., *Solar Water Splitting with Perovskite/Silicon Tandem Cell and TiC-Supported Pt Nanocluster Electrocatalyst.* Joule, 2019. **3**(12): p. 2930-2941.

223. Abdi, F.F., et al., *Mitigating voltage losses in photoelectrochemical cell scale-up.* 2020. **4**(6): p. 2734-2740.

224. Chen, Y., et al., *Large-area perovskite solar cells–a review of recent progress and issues.* 2018. **8**(19): p. 10489-10508.

225. Mohammed-Ibrahim, J., *A review on NiFe-based electrocatalysts for efficient alkaline oxygen evolution reaction.* Journal of Power Sources, 2020. **448**: p. 227375.

226. Jamesh, M.-I. and M. Harb, *Tuning the electronic structure of the earth-abundant electrocatalysts for oxygen evolution reaction (OER) to achieve efficient alkaline water splitting – A review.* Journal of Energy Chemistry, 2021. **56**: p. 299-342.

227. Li, Y., et al., *Implanting Ni-O-VOx sites into Cu-doped Ni for low-overpotential alkaline hydrogen evolution.* Nature Communications, 2020. **11**(1): p. 2720.

228. Zang, Y., et al., *Tuning orbital orientation endows molybdenum disulfide with exceptional alkaline hydrogen evolution capability.* Nature Communications, 2019. **10**(1): p. 1217.

229. Qi, K., et al., *Single-atom cobalt array bound to distorted 1T MoS2 with ensemble effect for hydrogen evolution catalysis.* Nature Communications, 2019. **10**(1): p. 5231.

230. Nairan, A., et al., *NiMo Solid Solution Nanowire Array Electrodes for Highly Efficient Hydrogen Evolution Reaction.* Advanced Functional Materials, 2019. **29**(44): p. 1903747.

231. Li, Y., et al., *Nickel-molybdenum nitride nanoplate electrocatalysts for concurrent electrolytic hydrogen and formate productions.* Nature Communications, 2019. **10**(1): p. 5335.

232. Huang, Y., et al., *Atomically engineering activation sites onto metallic 1T-MoS2 catalysts for enhanced electrochemical hydrogen evolution.* Nature Communications, 2019. **10**(1): p. 982.

233. Huang, D., et al., *Self-templated construction of 1D NiMo nanowires via a Li electrochemical tuning method for the hydrogen evolution reaction.* Nanoscale, 2019. **11**(41): p. 19429-19436.

234. Hu, K., et al., *Boosting electrochemical water splitting via ternary NiMoCo hybrid nanowire arrays.* Journal of Materials Chemistry A, 2019. **7**(5): p. 2156-2164.

235. Ganguli, S., et al., *Inception of molybdate as a "pore forming additive" to enhance the bifunctional electrocatalytic activity of nickel and cobalt based mixed hydroxides for overall water splitting.* Nanoscale, 2019. **11**(36): p. 16896-16906.

236. Zhu, C., et al., *Fe-Ni-Mo Nitride Porous Nanotubes for Full Water Splitting and Zn-Air Batteries.* Advanced Energy Materials, 2018. **8**(36): p. 1802327.

237. Yuan, W., et al., *Interfacial Engineering of Cobalt Nitrides and Mesoporous Nitrogen-Doped Carbon: Toward Efficient Overall Water-Splitting Activity with Enhanced Charge-Transfer Efficiency.* ACS Energy Letters, 2020. **5**(3): p. 692-700.

238. Zhang, L., et al., *Rational construction of macroporous CoFeP triangular plate arrays from bimetal–organic frameworks as high-performance overall water-splitting catalysts.* Journal of Materials Chemistry A, 2019. **7**(29): p. 17529-17535.

239. Du, C., et al., *Nest-like NiCoP for Highly Efficient Overall Water Splitting.* ACS Catalysis, 2017. **7**(6): p. 4131-4137.

240. Karuturi, S.K., et al., *Over 17% Efficiency Stand-Alone Solar Water Splitting Enabled by Perovskite-Silicon Tandem Absorbers.* 2020. **10**(28): p. 2000772.

241. Xu, J., et al., *Triple-halide wide–band gap perovskites with suppressed phase segregation for efficient tandems.* 2020. **367**(6482): p. 1097-1104.

242. Chen, B., et al., *Enhanced optical path and electron diffusion length enable high-efficiency perovskite tandems.* Nature Communications, 2020. **11**(1): p. 1257.

243. Gharibzadeh, S., et al., *2D/3D Heterostructure for Semitransparent Perovskite Solar Cells with Engineered Bandgap Enables Efficiencies Exceeding 25% in Four-Terminal Tandems with Silicon and CIGS.* 2020. **30**(19): p. 1909919.

244. Duong, T., et al., *High Efficiency Perovskite-Silicon Tandem Solar Cells: Effect of Surface Coating versus Bulk Incorporation of 2D Perovskite.* 2020. **10**(9): p. 1903553.

245. Duong, T., et al., *Rubidium Multication Perovskite with Optimized Bandgap for Perovskite-Silicon Tandem with over 26% Efficiency.* 2017. **7**(14): p. 1700228.

246. Shen, H., et al., *Mechanically-stacked perovskite/CIGS tandem solar cells with efficiency of 23.9% and reduced oxygen sensitivity.* Energy & Environmental Science, 2018. **11**(2): p. 394-406.

247. McMeekin, D.P., et al., *A mixed-cation lead mixed-halide perovskite absorber for tandem solar cells.* 2016. **351**(6269): p. 151-155.